MULTI SCALE MODELING OF DUAL PHASE STEELS WITH INTEGRATED COMPUTATIONAL MATERIALS ENGINEERING FRAMEWORK

A THESIS SUBMITTED TO
THE GRADUATE SCHOOL OF NATURAL AND APPLIED SCIENCES
OF
MIDDLE EAST TECHNICAL UNIVERSITY

BY

DOĞUCAN BAKKALBAŞI

IN PARTIAL FULFILLMENT OF THE REQUIREMENTS
FOR
THE DEGREE OF MASTER OF SCIENCE
IN
METALLURGICAL AND MATERIALS ENGINEERING

NOVEMBER 2022

Approval of the thesis:

MULTI SCALE MODELING OF DUAL PHASE STEELS WITH INTEGRATED COMPUTATIONAL MATERIALS ENGINEERING FRAMEWORK

submitted by **DOĞUCAN BAKKALBAŞI** in partial fulfillment of the requirements for the degree of **Master of Science** i**n Metallurgical and Materials Engineering, Middle East Technical University** by,

Prof. Dr. Halil Kalıpçılar
Dean, Graduate School of **Natural and Applied Sciences**

Prof. Dr. Ali Kalkanlı
Head of the Department, **Met. and Mat. Eng.**

Assoc. Prof. Dr. Caner Şimşir
Supervisor, Metallurgical and Materials Eng**, METU**

Assist. Prof. Dr. Omer Music
Co-Supervisor, Mechanical Eng**, TED University**

Examining Committee Members:

Prof. Dr. Cemil Hakan Gür
Metallurgical and Materials Eng, **METU**

Assoc. Prof. Dr. Caner Simsir
Metallurgical and Materials Eng, **METU**

Assist. Prof. Dr. Omer Music
Mechanical Eng**, TED University**

Assist.Prof. Dr. Eda Aydoğan
Metallurgical and Materials Eng, **METU**

Assoc.Prof. Dr. İzzet Özdemir
Civil Eng., **İzmir Institute of Technology**

Date: 21.11.2022

I hereby declare that all information in this document has been obtained and presented in accordance with academic rules and ethical conduct. I also declare that, as required by these rules and conduct, I have fully cited and referenced all material and results that are not original to this work.

Name Last name : Doğucan Bakkalbaşı

Signature :

ABSTRACT

MULTI SCALE MODELING OF DUAL PHASE STEELS WITH INTEGRATED COMPUTATIONAL MATERIALS ENGINEERING FRAMEWORK

Bakkalbaşı, Doğucan
Master of Science, Metallurgical and Materials Engineering
Supervisor: Assoc. Prof. Dr. Caner Şimşir
Co-Supervisor: Assist. Prof. Dr. Omer Music

November 2022, 174 Pages

In this thesis, process-chain simulation of of Dual-Phase (DP) steels (DP600, DP800) with different chemical compositions and manufacturing histories is performed, in line with Integrated Computational Materials Engineering (ICME) principles. To do this, the required material data is acquired by multi-scale modelling, which enables bi-directional link between the material production processes with the manufacturing processes. The thesis consists of 2 important stages, each of which includes innovations in its own field, as well as combining many modern methods in an original way.

In the first phase of the project, the focus is the inter-critical annealing (IA) process, one of the most important steps in DP steel production. First, the microstructure of the material is determined by computational thermodynamics/kinetics methods. Then, Thermodynamics Based Material Property Calculation (TBMPC) method is employed to determine mechanical properties of individual phases. TBMPC method has not yet been applied to these materials and processing methods.

In the second phase, macroscopic mechanical properties are calculated from the individual properties of phases using the composite material theory. Two approaches used here: (a) Mean Field Homogenization and (b) Finite Element Representative Volume Element Homogenization. In the literature, there exist no studies employing MFH, which can be a robust alternative. Moreover, the Bauschinger effect is also studied in material models which has significant consequences on prediction of spring-back especially for multi-phase materials.

The findings could provide a better insight for further improvement of performance of DP steels. Moreover, suggested methods have a potential to replace experimental approaches in the future.

Keywords: Integrated Computational Materials Engineering (ICME), multi-scale modeling and simulation, dual-phase (DP) steels

ÖZ

ÇİFT FAZLI ÇELİKLERİN ÜRETİMİ VE ŞEKİLLENDİRİLMESİ İÇİN BÜTÜNLEŞİK HESAPLAMALI MALZEME MÜHENDİSLİĞİ (BHMM) YAKLAŞIMIYLA YENİ BİR ÇERÇEVE GELİŞTİRİLMESİ

Bakkalbaşı, Doğucan
Yüksek Lisans, Metalurji ve Malzeme Mühendisliği
Tez Yöneticisi: Doç. Dr. Caner Şimşir
Ortak Tez Yöneticisi: Dr.Öğr.Üyesi Omer Music

Kasım 2022, 174 sayfa

Bu tez süresince, farklı kimyasal bileşimlere ve farklı üretim geçmişlerine sahip çift fazlı (DP) çeliklerin (DP600 ve DP800) süreç zinciri simülasyonu yenilikçi bir yaklaşım olan Bütünleşik Hesaplamalı Malzeme Mühendisliği (BHMM) ve ilkeleri doğrultusunda gerçekleştirilmiştir. Bunun için gerekli olan malzeme verileri, malzeme üretimi ve imalat süreçleri arasında iki yönlü bir köprü kuran çok ölçekli modelleme ile elde edilmiştir. Tez, birçok modern yöntemin özgün bir şekilde birleştirilmesinin yanı sıra her biri kendi alanında yenilikler içeren 2 önemli aşamadan oluşmaktadır:

İlk aşamada odak noktası, DP çeliklerinin üretimindeki en önemli basamaklardan biri olan ara kritik tavlama işlemi olacaktır. Malzemenin mikro yapısı hesaplamalı termodinamik ve kinetik yöntemlerle belirlendikten sonra, malzemenin içindeki her fazın birbirinden bağımsız mekanik özelliklerinin belirlenmesi için Termodinamik Esaslı Malzeme Özelliği Hesaplama (TEMÖH) yöntemi kullanılacaktır. TEMÖH yöntemi daha önce söz konusu malzemelere ve üretim işlemlerine ilk defa uygulanacaktır.

İkinci aşamada, malzemenin mikroskobik mekanik özellikleri (akma eğrisi, döngüsel pekleşme davranışı) içyapıyı oluşturan fazların bireysel özelliklerinden yola çıkarak kompozit malzeme teorisi ile hesaplanacaktır. Çözüm aşamasında a) Ortalama Alanlar Homojenizasyonu (OAH) ve b) Sonlu Elemanlar-Temsili Hacim Elemanı Homojenizasyonu (SE-THEH) olmak üzere iki yaklaşım uygulanacaktır. Literatürde, verimli bir alternatif olan OAH ile ilgili yapılmış bir çalışma bulunmamaktadır. Ayrıca, özellikle çok fazlı malzemelerde önemli etkisi bulunan Bauschinger etkisi ve geri yaylanma tahmini de oluşturulacak modelde hesaba katılacaktır.

Tezden çıkacak bulgularla, DP çeliklerinin performansının iyileştirilmesi ve süreç optimizasyonu hedeflenmiştir. Ayrıca önerilen yöntemler gelecekte zamandan ve maliyetten fayda sağlayacak şekilde deneysel yaklaşımların yerini alma potansiyeli taşımaktadır.

Anahtar Kelimeler: Bütünleşik Hesaplamalı Malzeme Mühendisliği (BHMM), Çok ölçekli modelleme ve simülasyon, çift fazlı (DP) çelikler

To my family…

ACKNOWLEDGMENTS

First of all, I would like to thank my advisor Assoc.Prof Caner Şimşir for his understanding and guidance. With the additional trainings he gave during last 2 years we worked together, he gave me the chance to develop professionally and broaden my perspective. In addition, it would have been impossible to finish this thesis without his solution-oriented ideas, approach and deep knowledge. Thanks to his informative style and willingness to share his expertise and experience, I have no doubt that he will contribute to the future training of many talented engineers.

I would like to express my thanks to Betül Gövercin, Çağlar Ünver and Şamil Dinçer for their contributions and help to this work.

I would like to express my gratitude for the friendship and support of Uzay Anıl Bilgin, Elif Coşkun, Mustafa Caner Görür, Burak Çamloğlu, Mehmet Demiroğlu, Uğur Aydoğan, Begüm Erdem, Volkan Ertaş, and Atalay Balta. Without you guys, the university would not have a taste.

I am always grateful to my family Okan Bakkalbaşı, Mukaddes Bakkalbaşı and Ekin Bakkalbaşı. Their endless love and support have always been an extra strength for me. If there's anything resembling success anywhere in my life, more than half of it is always theirs.

Lastly, my love and my companion Ezgi Keçecioğlu is the owner of my deepest gratitude. Her support and encouragement are very precious and always made me feel very lucky. I am so grateful to have you in my life.

TABLE OF CONTENTS

CHAPTERS

APPENDICES

LIST OF TABLES

TABLES

LIST OF FIGURES

FIGURES

LIST OF ABBREVIATIONS

ABBREVIATIONS

DP: Dual Phase

ICME: Integrated Computational Materials Engineering

TBPCM: Thermodynamics Based Property Calculation Method

CALPHAD: Calculation of Phase Diagrams

BE: Bauschinger Effect

MFH: Mean Field Homogenization

FEA: Finite Element Analysis

RVE: Representative Volume Element

IAT: Inter-critical Annealing Temperature

IA: Inter-critical Annealing

MS: Martensite Start

OAT: One at a Time

LIST OF SYMBOLS

SYMBOLS

α: Ferrite iron

γ: Austenite iron

σ: Stress (MPa)

σ_0: Yield stress (0.2%) MPa

ε: Strain

K: Strain hardening coefficient

n: Strain hardening exponent

CHAPTER 1

INTRODUCTION

From the new material design perspective, with the development of inexpensive, yet very fast computers and the availability of software, computational modeling and simulation became a very useful tool in last 3 decades to design and develop more sophisticated materials and models[1] . One of the most important blessings of this field is the limitation of large-scale experimental studies that can be done by using various software that integrates various physical and phenomenological approaches and can make predictions very close to experimental results, thus saving time and money. Under the influence of these developments Integrated Computational Materials Engineering (ICME), a sub-branch of computational materials science, emerged. As Olson and Gregory (2000)[2] mentioned, this approach is a multidisciplinary approach that connects material models at multiple length scales to design products, associated materials, and material production methods. In this approach, the word "Integrated" has been emphasized in multiple relations, and the word "Engineering" has been emphasized to take care of industrial benefit. The focus in the approach is to analyze material models in terms of properties like mechanical, electrical, magnetic etc. It is to be able to design materials and manufacturing processes in two directions and to optimize them together, by taking into account the effect on the properties of the product.

From the point of view of the thesis, the main problem in experimental studies arises from the loss of time and cost in the trial-and-error processes and material loss due to the inability to recycle 100% of the used material. Modeling and simulation methods, which will be realized within the framework of ICME principles, where significant developments have been shown especially in the last 10 years, promise significant hope in overcoming these problems. If the applicability of this method is demonstrated throughout the whole process by using minimum experimental data, there may be a step in terms of its usability in the process of alloy design in the future. In addition, this approach has the potential to save manufacturers and researchers from a burden that can last for years, especially in R&D studies. As can be seen in Figure-1.1a and Figure-1.1b, if the ICME approach is successfully integrated into product development systems, the use of physics-based models to optimize production processes and component performance promises to drastically reduce product development time and cost. [2]

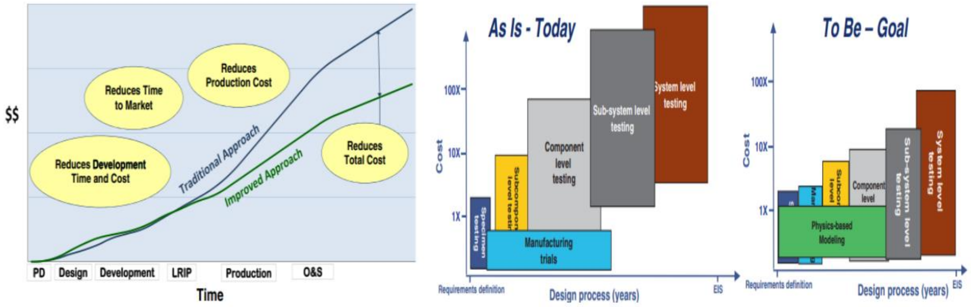

Figure 1.1. a) Less iterative production trials with physics-based modeling, the effect of system design in terms of cost and process b) The effect of ICME approach on cost and process [3]

One of the benefits of modeling simulation methods is information that cannot be reached by experimental processes (such as how variables like extreme temperature and extreme pressure values will affect material properties on any application) can be reached with consistent approaches.

If it is shown that the method works successfully it may be used to analyze and develop new alloys and can create a database and information pool that will fill the lack of first-hand information on these issues in our country. In this way, it promises hope for the coming years in terms of creating a modeling infrastructure for materials with more complicated microstructures.

The research question of the thesis is “Can we predict the properties of the material and the related manufacturing performance based on the parameters of the material production process, can we design/improve both the material production processes and the manufacturing processes using material data in an integrated manner?”.

The hypothesis of the thesis is that “This can be achieved by uniquely combining many of the modern computational materials and manufacturing engineering techniques in a ICME framework.”. When the material production and forming processes of the DP steels, which are the subject of the project, are considered as a whole, there is no similar study in the literature. In addition, there are innovations in the independent areas used, as will be detailed in the following parts of the thesis.

In this thesis, firstly, the amounts and compositions of the phases are obtained by performing computational thermodynamic and kinetic analyzes via THERMOCALC software, starting from the material production parameters (chemical composition, intermediate critical annealing temperature (IAT), time and cooling rate) provided by the supplier data. This information is used as input to the TBPC method and thus independent flow curves of ferrite and martensite phases are obtained. At the same time, independent of the models, experimental metallographic tests are started in order to be able to compare with the model later on. This type of modeling is a novelty for the literature, although material models such as yield curve modeling have been made in the literature[4,5], thermodynamic-based property calculations are not included in the material production process with models.

The thesis is then continued by creating a phase data in line with the values collected from thermodynamic-based modeling. This phase data is used to determine the mechanical properties of steel in micro-mechanical modeling. In that phase some micro-macro mechanical transition methods are employed.

2 different homogenization methods are used to make the micro-macro transition after the Representative Volume Element (RVE) of the material is created by taking into account the orientations of the phases, shape, grain sizes and volume fractions. The first of these is Mean Field Homogenization (MFH) which is a fast method that

provides the macro-scale behavior of stress strain fields by taking the micro-scale volume averages gives consistent values, not exact, but approximate values.

Considering the homogenization method to be used, the Voigt-Reuss method, which is frequently used in composite modeling, assumes that the stress strain values in Representative Volume Element (RVE) are completely uniformly distributed, creating a large band between the upper limit and the lower limit values, especially in materials with very large mechanical differences between the two phases, such as DP steels cannot give consistent results. This problem was overcome with Eshelby's solution and after more sophisticated solution models are emerged. While modeling, the Mori-Tanaka composite method, which is one of the most sophisticated and famous models emerged from this approach, is used for homogenization (Mori,Tanaka, 1973) [6].

Finite Element Analysis (FEA) is used as the second method. The main difference of this method from the first one is that it solves the RVE problem in detail by performing a much more detailed numerical analysis, calculating the average strain and stress distributions as well as the micro stress and strain distributions for each phase and grain.

The important point to be noted here is that during modeling, the phenomenon called “Bauschinger Effect” (Kinematic or Directional Hardening), which is frequently observed in multiphase materials should be taken into account when making mechanical models, is also be included in the calculations. Weiss et al. (2015)[7] showed in a study that this effect is mostly seen in cyclic compression-tensile loading situations, especially in multi-phase materials, since the two phases do not deform at the same time at the same amount and different strain forces are formed at the interfaces. It is a well-known effect in DP steels and it should be taken into account during modeling.

The innovative and prominent aspects of the Thesis are summarized below:

- A new interdisciplinary framework is developed by bringing together existing modern theories and methods holistically.

- Although TBPCM (Thermodynamics Based Property Calculation Method) has many applications, the TBPCM method has not been used in the process-chain modeling of steels before.

- There are examples of calculation of yield curves obtained in the uniaxial tensile test of DP steels using the FE-RVE (Finite Element - Representative Volume Element) method. However, the MFH (Mean Field Homogenization) method, which is much faster and requires less sources, has not been applied to DP steels.

- Although the effect of the Bauschinger effect on spring back during the shaping of DP steels has been investigated and proven experimentally, this behavior in DP steels has not been determined computationally using either FE-RVE or MFH methods.

CHAPTER 2

LITERATURE REVIEW

The subjects within the scope of this thesis and the studies on it are mentioned under this title.

2.1 DP Steels

DP steels are the most widely used member of the advanced high-strength steels family (AHSS) (Figure 2.1, Figure 2.2), with values reaching almost 60 percent. These steels, which occupy a significant place in the automotive industry, are generally used in automobile exterior ceiling, exterior door, side body and floor panel construction.

They are generally obtained by thermomechanical processing of low carbon steel and their microstructure consists of soft continuous ferrite matrix and hard martensite islands on it. This heterogenous composite like microstructure enables the material to achieve both good formability and high strength values at the same time [8–10]. They are generally characterized by their high yield strength, high maximum tensile strength, high strain hardening and elongation.[11] .

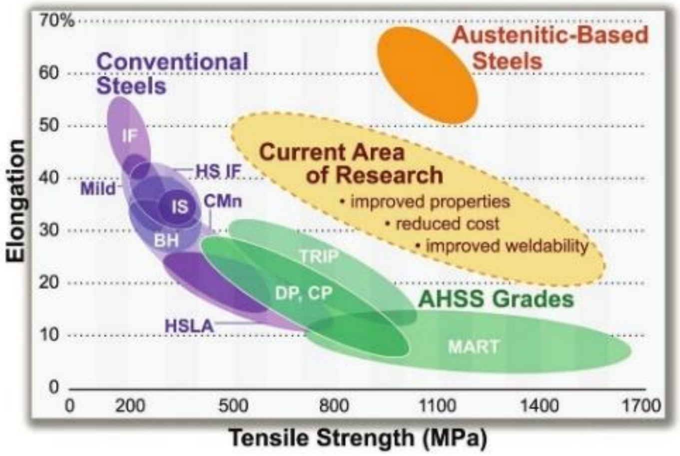

Figure 2.1. General Elongation vs Tensile Strength Curve of AHSS type steels [12]

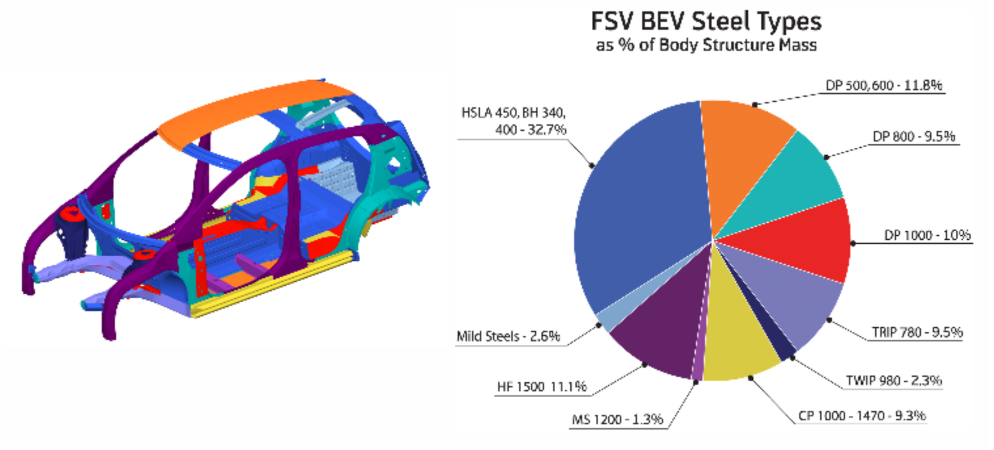

Figure 2.2. Widely used steel types and locations for automobiles, 20 Years of Automotive Steel Contributions [13]

The engineering properties of dual-phase steels vary strongly depending on the machining processes and therefore their microstructures. Generally, 2 different production routes are followed. First one is continuous annealing after hot rolling, and the second as hot rolling, batch annealing and cold rolling at the end. In some processes, short-term tempering can also be applied to increase the ductility of the steel. Annealing in the inter-critical region is of great importance in the production process and the ferritic-martensitic microstructure is obtained by quenching after annealing from A1-A3 temperatures region [14].

2.1.1 IAT Mechanism

Inter critical annealing (IA) heat treatment is a heat treatment process to develop DP microstructure in low alloy steels and involves heating to steel at a temperature between A1 and A3 temperatures.

If the material is cooled from the annealing temperature to the IA zone: First, the austenite phase begins to be enriched with carbon and the austenite-forming elements partitioning occur between austenite and ferrite. Then as the amount of cooling increases, the interfaces of austenite and ferrite phases in the microstructure accelerate the ferrite formation reaction and austenite decomposition[15]. The annealing time of the material at the IAT directly affects the chemical composition of the austenite, thus the martensite morphology that will occur after the quenching process[16,17].

Generally ferritic-pearlitic initial microstructure is used to obtain DP steels. At the IA heat treatment austenite grows very rapidly until pearlite is fully dissolved. Then slower growth of austenite at high IAT's (~800) is controlled by carbon diffusion in austenite and manganese diffusion in ferrite at low temperatures (~750 C). At the final equilibration of ferrite and austenite, manganese diffusion in austenite controls the reaction slowly [18].

Below Figure 2.3 shows the time to reach equilibrium of steels with different carbon content at different austenitization temperatures. As the amount of carbon in the steel increases, the amount of austenite formed in the material at the same temperature and at the same time increases as well[19]. Also, as the annealing temperature approaches the eutectoid temperature, time needed to reach equilibrium increases significantly. Maximum austenitization rate is always observed in the beginning of isothermal holding and then it progressively decreases.

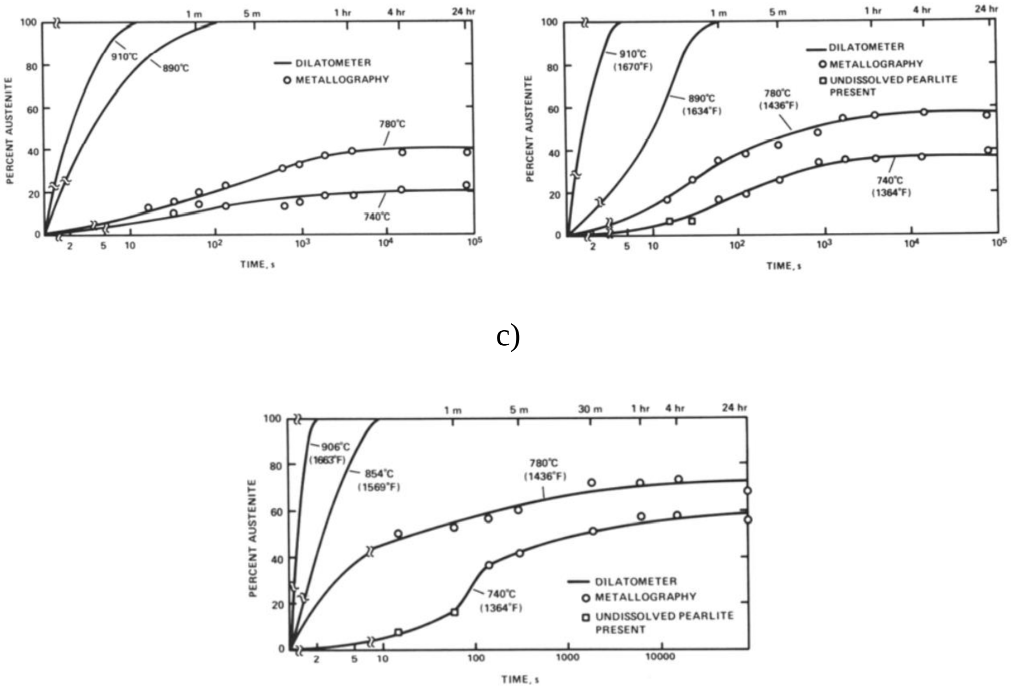

a) b)

c)

Figure 2.3. Austenite formation kinetics in steels with different chemical composition a) 0.06C-1.5M b)0.12C-1.5Mn c.)0.20C-1.5Mn steel [18]

To obtain a steel with desired mechanical properties, effect of heat treatment parameters such as heating rate, annealing temperature, annealing time and cooling rate should be taken into account. Holding time at IAT directly affect the austenite growth and chemical homogeneity. Also, chemical composition of the steel affects the heat treatment response with several thermodynamic factors such as carbon diffusivity, activity of carbon in austenite, Ac1 and Ac3 critical temperatures and α to γ transformation activation energy. The production method used in connection with these factors affects the microstructure of the steel. Instead hot rolling the material at austenitizing temperature and then cool it to produce the desired amount of ferrite, better and more stable microstructure can be obtained by thermo-mechanically rolling the material at IA zone[20].

The path followed for the formation of this microstructure is given schematically in Figure 2.4. Hayami(1977) [21] showed in the past years that this process directly affects the amount, composition and carbon content of martensite. In addition, rolling parameters and amount of plastic deformation applied on a steel sheet during production may change the stress strain distribution in the microstructure depending on the thickness of the material [22,23]

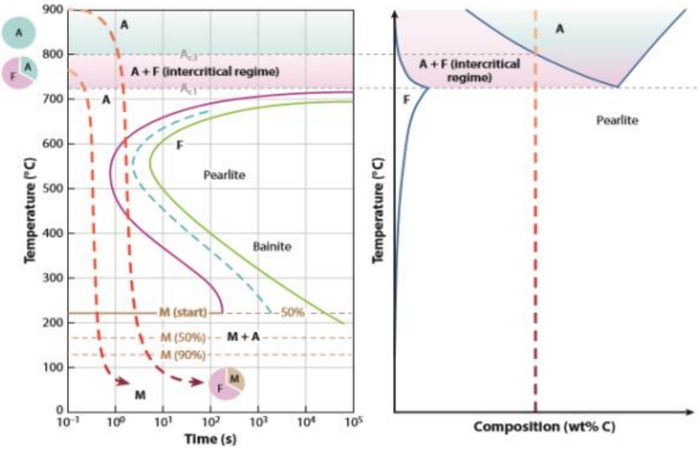

Figure 2.4. Schematic representation of the heat treatment process followed to create the ferritic-martensitic structure in DP steels [22]

Moreover, Tasan et al. (2015)[22] showed that DP steels go through metallurgical processes such as recovery, recrystallization and diffusion during their production. The interactions and competition of these mechanisms vary according to factors such as heating/cooling rate, annealing temperature and quenching rate creates a complex problem to solve.

2.1.2 Effect of Initial Microstructure

Initial microstructure of steel prior to heat treatment affects the nucleation and growth kinetics of individual phases, austenite ferrite mixture morphology and final microstructure after cooling. Original microstructure of steel dictates the transformation kinetics by shifting the critical phase transformation temperatures. In order to increase the rate of austenitization, the initial microstructures are categorized as follows: ferrite with spheroidized carbides, ferrite with lamellar pearlite, as-quenched and cold deformed microstructures[24].

Hot rolled (HR) and cold rolled (CR) ferritic-pearlitic steel sheets behave differently at the IA treatment with the same temperature. In cold rolled steels due to high stored energy, recrystallization may begin before the expected temperatures which change the dilatation response of the material. Due to heating rate and insufficient time to thermodynamic equilibrium, different initial structures can formed with partially or completely recrystallized ferrite grains and different alloying element partitions between phases.

In HR steels heat treatment response can be summarized as follows: Thermal expansion of ferrite pearlite structure follows the austenite transformation from pearlite then ferrite to austenite transformation and thermal expansion of austenite occurs. In HR steels, the heating rate and the IAT affect the austenite size formed in the steel. As the heating rate increases, austenite grains with smaller grain size are formed due to the shift of the austenite line to higher temperatures [25]. Austenite generally nucleates at austenite/ferrite interfaces. As the grain size of ferrite decreases amount of austenite/ferrite interfaces hence the austenitization rate increases proportionally. For relatively short holding times, austenitization rate of cold rolled steels are expected to be higher than the hot rolled ones due to this reason [26]. But it is shown that austenite fraction difference among different original microstructures is negligible for long holding times close to A3 temperature. Also, for CR steels, effect of initial microstructure for austenitization kinetics can completely be eliminated if the recrystallization is completed before austenite transformation [25].

2.1.3 Effect of Cooling Rate from IAT

Cooling rate is one of the most effective factors which determines the final microstructure and mechanical properties of DP Steels. Rate of the cooling and formed thermal stresses affect the final properties of the material. By using higher cooling rates DP Steels can be produced using low alloy content and lower carbon contents. However, low alloying content DP Steels are very sensitive to heating regime [27].

In relatively slower cooling rates newly formed ferrite continues to grow with increasing amounts of austenite. This newly formed ferrite has less carbon content and less hardenability. The austenite produced by this method is also more stable and has less temperature sensitivity [17]. Although there is a slight decrease in the strength after quenching due to slow cooling rates, the decrease in the carbon and nitrogen content dissolved in the ferrite significantly increases the ductility of the steel and the amount of uniform elongation [28]. Which shows the advantage of the low cooling rate in the DP steel production as long as the strength level is maintained[29].

In parallel with the production method of DP steel, the carbon saturation in austenite when it is cooled from the IAT from a fully austenitization zone and the carbon saturation in austenite when the material is heated directly from room temperature to the IAT are different from each other. Second process significantly increases the austenite stability. This is one of the important aspects of the IA process in order to obtain the desired mechanical properties from low carbon alloy steels. In this way, it is possible to accelerate the nucleation and transformation rate of ferrite and decelerate the transformation rate of pearlite[30].

One example of mechanical Properties as a function of IAT is shown in Figure 2.5.

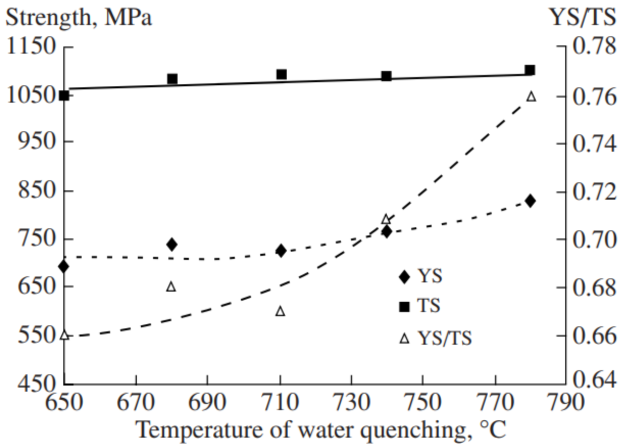

Figure 2.5. Change of yield stress, tensile stress according to quenching temperature in DP steels [31]

2.1.4 Effect of Metallurgical Parameters to Final Material

In DP steels, the manufacturing process has a great influence on the mechanical property of the steel, and this is directly affected by some factors that trigger the change in the microstructure. Some of the most important ones are martensite volume ratio, martensite morphology (shape, size and orientation), their distribution in the microstructure (homogeneous or banded) and the ferrite grain size [8,32].

To explain it with examples from the literature, it is observed in studies related to martensite volume ratio (VM) as the IAT of the manufacturing process increases, the VM ratio in the material and the material strength increase linearly after the quenching process. But this continues up to a certain limit. A decrease in strength can be observed after the VM reaches 50-60% [33]. Also, as the carbon content in the material increases, the VM increases linearly, but the intermediate temperature range where ferrite and austenite exist together narrows. From this it can be deduced that DP steels with high carbon content are more temperature sensitive. This abnormal behavior is generally explained by the dilution of carbon and the softening of the material [10]. As a result, it can be said that there may be no linear relationship between VM and strength after a point and optimization is required.

As VM increases in DP steels, the ductility of the material, amount of uniform elongation and the necessary amount of strain to reach the tensile stress decreases. It can be said that this behavior is due to void mechanisms during deformation. The number of micro voids and their coalescence rate increases as the volume fraction of martensite in DP steel increases. Increasing amount of martensite decreases the distance required for void coalescence by reducing void spacing. Along with the decohesion on grain boundaries the amount of plastic strain required for void coalescence reduces. Likewise, same mechanism can be observed with the increase in the decohesion along the grain boundaries due to higher hardness of martensite.

One of the other factors affecting the deformation mechanism is the size of martensite islands. For the same VM ratios, higher uniform elongation amounts can be achieved with finer martensite morphology due to delayed coalescence of voids. Likewise, finer ferrite grain size delays the void formation and increases the amount of uniform elongation observed in steel [34].

Mechanical property differences between ferrite and martensite and the inhomogeneous deformation behavior triggers the crack initiation. Differences in plastic non-homogeneity between phases may result in increased or decreased crack growth rate with branching of cracks. Likewise, the volume changes that occur when the retained austenite that can remain in the structure are transformed into martensite with deformation may also play a role in reducing the effective load on the material.

Similarly, when DP steels with the same VM ratio were examined, it was observed that the differentiation of martensite morphology and distribution, and therefore the differentiation of stress-strain distribution between the two phases, caused considerable changes in the mechanical properties of the material. The main reason for this is the deformation mechanism observed in DP steels. Rashid and Cprek[35] explained this mechanism as follows; ferrite, which is a softer phase, under any load begins to deform much faster than martensite and creates a shear force at the phase interface. When the ferrite phase is highly deformed, the high strain give rise to deformation of the martensite phase. In this case, the grain size of the ferrite and the stress strain values formed around it can be considered as the factors affecting the deformation mechanism. It is shown that up to 50-60% martensite there is no effect of martensite yield strength on mechanical properties of DP Steels. Because at small strains, martensite islands only deform elastically. Independence of DP steels of martensite strength is observed by several authors [31,36,37]**.** Most published data indicate that DP steel strength is linearly dependent on VM. Higher volume% martensite than 60% causes the microstructure stereology to shift and skeleton-type martensite predominates rather than martensite islands buried in a soft ferrite matrix with potential strain and stress partitioning.

Figure 2.5 Shows the strength of several DP steel specimens after quenching from different IA temperatures, there are negligible changes until 50-60% martensite even though the martensite morphologies and carbon contents are different[28]. Studies have shown that the strength of the material depends on the strength of ferrite and the volume fraction of martensite.

2.1.5 Strain Hardening in DP Steels

One of the most important advantages of DP steels is their high strain hardening rate than other low alloy steels which provide higher uniform elongation values. So, understanding and controlling the strain hardening parameters is important to produce a DP Steel with desired properties.

There are a lot of different empirical models to approximate stress-strain curves[38]. Among them most used one is the Hollomon parabolic power law model with the strain hardening exponent n [37].

$$\sigma = K\varepsilon^{n} \quad \textbf{(Eqn.1)}$$

K and n values can be found on logarithmic scale by plotting following equation,

$$\log(\sigma) = \log(k) + n\log(\varepsilon) \quad \textbf{(Eqn.2)}$$

where σ is the true stress, ε is the true strain, K and n are strain hardening coefficient and strain hardening exponent respectively.

The physical significance of the ultimate tensile strength (UTS) point refers to the condition where the geometric softening due to tensile stress is equal to strain hardening rate (dσ/dε) at the cross-sectional area of the specimen under deformation. This point represents the point where true stress equals strain hardening exponent (ε=n) due to volume conservation during deformation up to UTS as following:

$$F = \sigma * A \text{ when } dF = 0,\ \sigma dA + A d\sigma = 0. \quad \textbf{(Eq.3)}$$

$$\text{Rearranging, } d\sigma/\sigma = -dA/A.$$

$$\text{Substituting } d\varepsilon = -dA/A,$$

$$\text{the maximum load corresponds to } d\sigma/d\varepsilon = \sigma.$$

$$\text{With the power law, } \sigma = K\varepsilon^{n} \quad \textbf{(Eq.4)}$$

$$\text{and } d\sigma/d\varepsilon = nK\varepsilon^{n-1}$$

$$\text{Equating and simplifying, } K\varepsilon n = nK\varepsilon n-1,\ \varepsilon = n$$

Thus, it can be said that maximum load achieved when necking start at point where ε = n. But in multiphase materials due to inhomogeneous stress strain distribution among mechanically different phases, this method is not valid and different approximations are needed to calculate strain hardening behavior.

According to literature highest strain hardening rate is observed at the strain range of 0.01-0.05 which can be seen in Figure 2.6. After quenching high density of dislocations triggers the dislocation-dislocation and dislocation-interstitial atom interactions under deformation and lead high strain hardening rates[39]. Also, if retained austenite exist in microstructure it transforms to martensite under deformation, increases the dislocation density and hence strain hardening rate [40]. As the deformation increases, more regular dislocation cell substructure forms and decreases the rate.

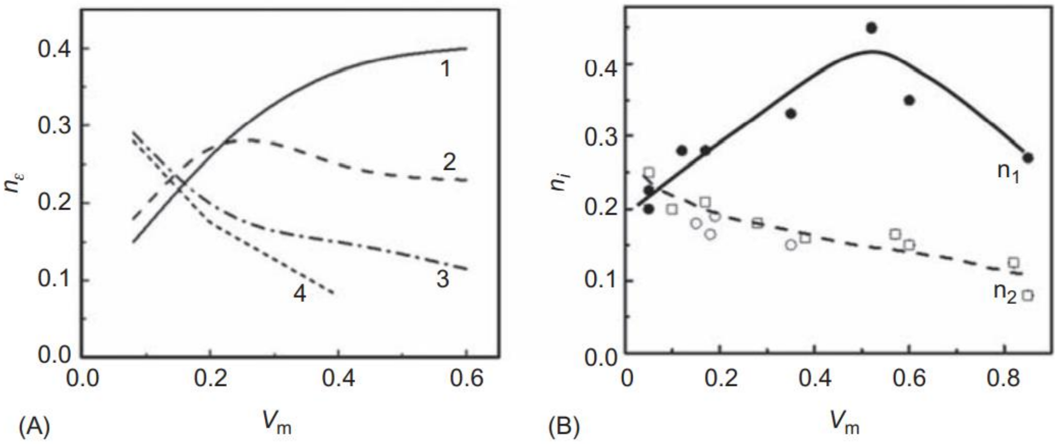

Figure 2.6. A) Effect of true strain in low alloy C-Mn-Cr steel to strain hardening exponent n 0.01, 0.02 , 0.05, 0.1 true strains respectively B) Volume fractions of martensite strain hardening relation in low alloy C-Mn-V steel. Source: N.M. [31]

Ferrite morphology and deformation mechanism affect the strain hardening behavior of DP steels. Strengthening ferrite by alloying additions like phosphorus and silicon promotes higher strain hardening rate and the uniform elongation of DP steels. Also, decrease in ferrite size generally accompanies a refinement of the martensite particles which make contribution to strain hardening [24]. Under fixed conditions of heat treatment used for obtaining DP steels, an increase in the volume fraction of martensite is accompanied by an increase in both the tensile strength and the yield strength of the steel, which at the level of the tensile strength above 850–900 MPa can be accompanied by a significant increase in the yield strength tensile strength ratio. This is explained by a more uniform strengthening of the bulk of ferrite due to the transformation-induced hardening upon the martensite transformation of austenite [24,31].

Their high ductility at any given stress level and low yield stress to tensile stress ratio, which can be as low as 0.4-0.5, because of the high density of mobile dislocations is one of the most important intrinsic properties of DP steels. These uniform elongation values are generally dictated by the strain hardening exponent n value. With the increase in the amount of martensite in the steel, the voids formed earlier than expected due to the incompatibility of deformation at the ferrite-martensite interface cause the ductility of the material and the strain hardening exponent to decrease. Effect of martensite content to strain hardening coefficient can be seen at Figure 2.7.

For this reason, it can be said that one of the best ways to increase the strain hardening of DP steel is to form martensite with lower carbon content with the same martensite fraction or increasing the necking strain (corresponding strain of ultimate tensile stress of ferrite) by silicon or phosphorus addition[26]**.**

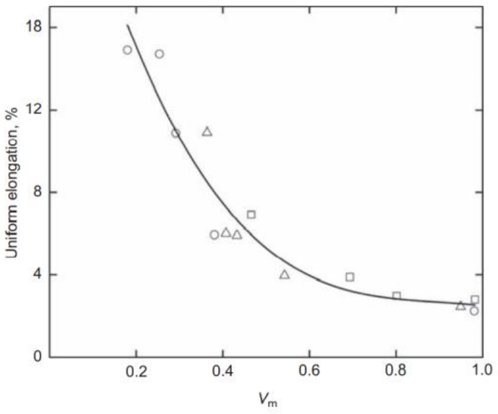

Figure 2.7. Effect of martensite volume percentage on Cr-Mn-Si-B steel's uniform elongation [24]

2.1.6 Grain Size Effect

Refinement of ferrite grain size increases the strength of DP Steels but the physical meaning of Hall-Petch coefficient is not the same for tempered steels and quenched steels due to stress relaxation by dislocation interactions at tempering stage. It is shown that the coefficient is strongly related with the true stress on quenched DP steels. According to literature it is shown that even the effect is low at low strain levels (0.2%) its contribution to strength increases at higher strains due to dislocation pinning mechanism of grain boundaries [24].

When it is compared with the ferritic steel strength contribution of ferrite grain size is lower in DP steels because of lower stress requirements to move dislocations due to existence of unlocked dislocations sources after quenching [24].

2.1.7 Effect of Chemical Composition on Dual Phase Steels

By altering the phase transformation lines, alloying elements have an impact on the reaction kinetics and thermodynamics[41].

The primary alloying components of DP steels are Mn, Si, C and Al. Depending on the steel's manufacturing process, some minor alloying components, such as Cr, Nb, Ti, and V might change the phase diagrams and alter the final product's properties. This section reveals the effects of alloying elements.

2.1.7.1 Effect of Carbon

Carbon is the most essential and one of the most effective alloying elements in general steels. The amount of carbon in DP steels directly influences the austenite and ferrite transformation rates, martensite start temperature, martensite strength, ferrite dislocation density, and residual stress built up on the material.

The effective carbon content in the γ phase, $C\gamma$ should be taken into account from two different angles: (1) carbon content in the initial austenite phase, which is determined by the heating parameters and the presence of carbide forming elements[26] and (2) carbon content in the final part of the γ phase, which is before the martensitic transformation and can be influenced by the quantity of recently transformed ferrite.

Formed austenite at the same IAT increases as the volume % of carbon in DP Steels increases which also increases the steel's strength after quenching.

But, as the applied IAT increases for the same composition of the steel, although amount of obtained austenite increases amount of carbon in austenite solution decreases since composition range narrows where austenite and ferrite coexist. This makes the higher carbon content DP Steels more sensitive to temperature variations. Since high-carbon steels are difficult to control in high-temperature reactions, it is generally preferred to start with low-carbon steels during the alloy design phase. This anomaly is explained with carbon dilution, which softens the martensite phase, lessening the overall strength of aggregate[32].

It demonstrates a trade-off between the strength-enhancing effects of the martensite volume percentage and the carbon content of austenite. Therefore, IAT and chemical composition of DP Steels must be arranged carefully during design phase and optimization of parameters.

Also, the carbon concentration in austenite fraction at the time of its change in cooling from the α - γ region is the primary factor affecting the Ms temperature and, consequently, the strength of martensite as shown in Figure 2.8.

a) b)

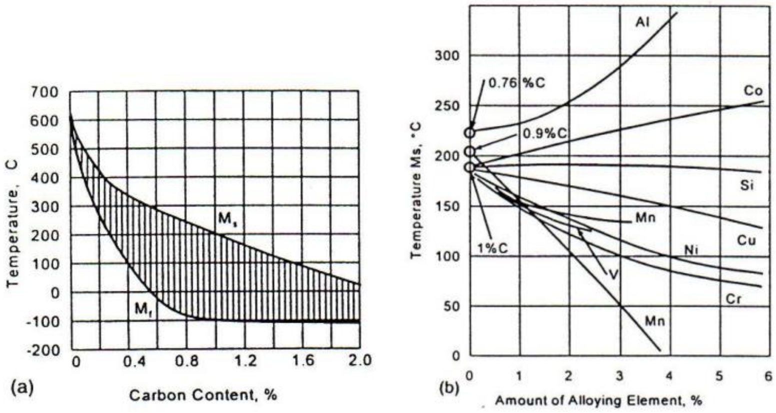

Figure 2.8. Effect of (a) %Carbon and (b) Alloying elements on the martensite transformation [42]

Moreover, carbon has an dramatic impact on the inter critical annealing A1–A3 range. In fact, within the temperature range of 760-850 °C, a reduction in the carbon content of Cr-Mn-Si steel from 0.18 percent to 0.10 percent and then to 0.07 percent decreases the rate of variation in the amount of C in γ-phase with temperature from 6 percent to 3.3 percent and then to 2.3 percent, respectively [43].

In order to understand the behavior of the DP steel in terms of the chemical composition, the interactions of different elements with each other should also be taken into account. Figure 2.9a shows the inversely proportional relationship of two essential alloying elements Mn and C in DP steels.

As shown, increase in Mn content decreases the %Carbon in austenite for the same IAT. Also, as shown in Figure 2.9b an almost double decrease in C can change the quantitative impact of a certain alloying element on the hardenability of austenite when modern DP steels with 0.08-0.12 percent C are heated to generate the 30-50 percent austenite or higher.

Moreover, effect of %C on tensile strength and YS/TS ratio DP steel can be seen from the Figure 2.10. Changing manganese and carbon content change the YS/TS ratio hence the strain hardening behavior of steel.

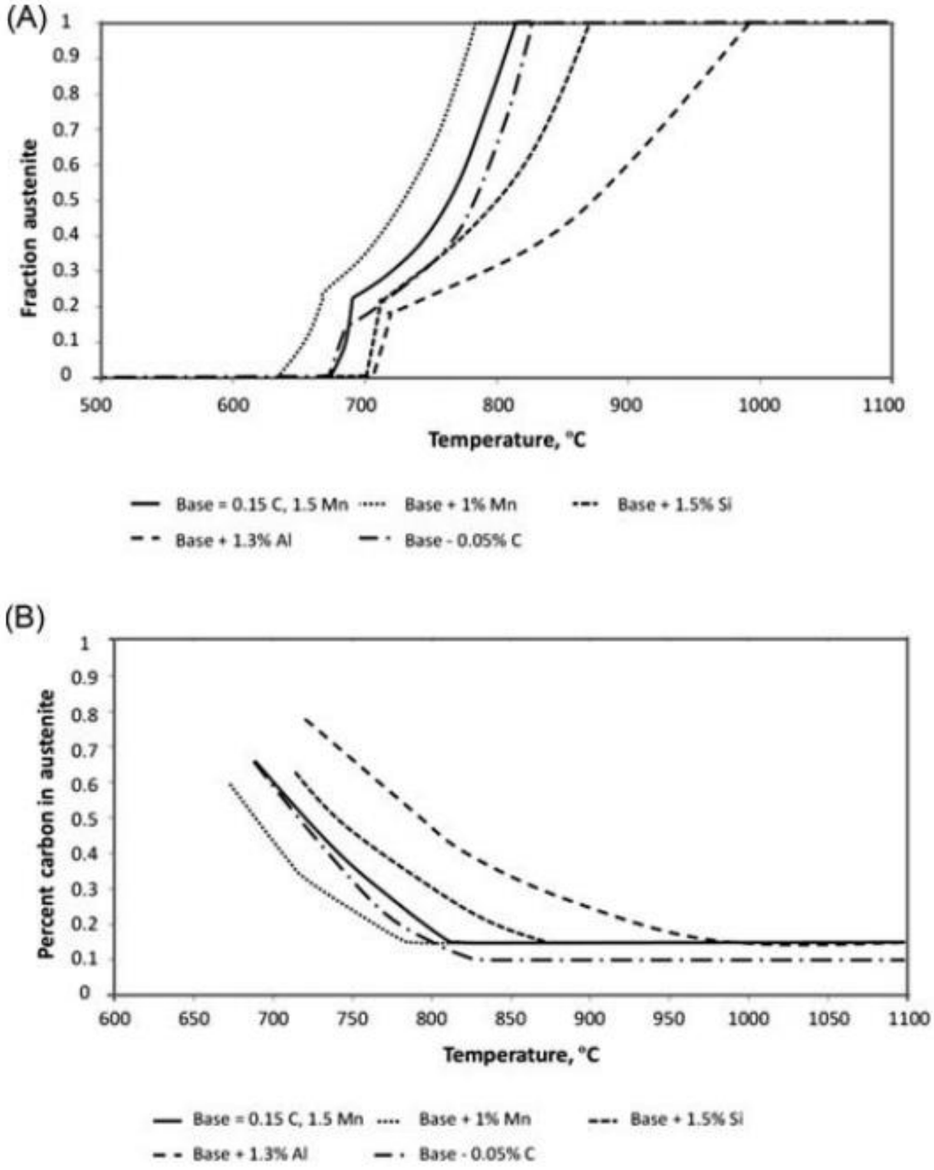

Figure 2.9. Effect of changes in steel composition depending on (A) The amount of volume fraction of austenite formed during heating in the intercritical range; (B) Carbon content in austenite [24]

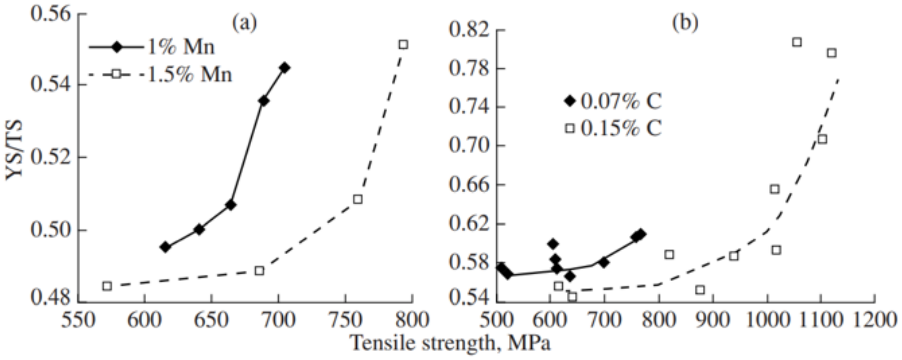

Figure 2.10. Effect of chemical composition on DP steels, the YS/TS ratio is affected by (a) in terms of manganese content and (b) in terms of carbon content (after water quenching from different IAT's) [31]

2.1.7.2 Effect of Silicon and Aluminum

Silicon and aluminum are the other 2 main alloying elements of DP steels.

Aluminum and Silicon restrict the formation of γ-iron, causing the γ-domain to shrink to a small area in the iron carbon diagram. This is because the respective elements promote BCC crystallographic structure, hence the BCC-iron ferrite and suppress FCC-iron austenite. Therefore, since these alloys change the reaction kinetics in cooling involving γ -phase transformation, the amount to be added as an alloying element should be carefully decided[42]**.**

Silicon and notably aluminum broadens the IAT range substantially among the alloying elements used in DP steels by significantly raising the A3 temperature and increases the slope of the $\gamma / (\alpha + \gamma)$ solvus which lowers the rate of austenite volume fraction variation with temperature.

Therefore, the volume fraction of the generated austenite and, consequently, of martensite after cooling, gradually decreases during the annealing of steels with higher Al and Si concentration at a fixed inter-critical temperature as shown in below. Increasing silicon and aluminum content give rise to the decrease in volume fraction of martensite.

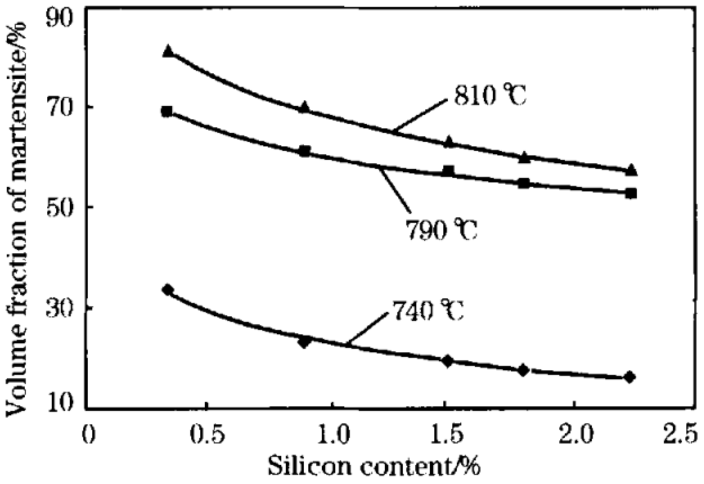

Figure 2.11. Volume fraction of martensite silicon addition relationship after quenching from different IAT's [44]

Moreover, silicon and aluminum are effective in work hardening behavior of DP steels as following. It has been shown in previous studies that the total elongation increases with the addition of aluminum. The reason for providing a better balance of tensile strength and total elongation with the addition of aluminum is due to the lowering of the martensite start temperature, the promotion of new ferrite formation, and the contribution of the refined ferrite grains to the deformation mechanism with finer martensite islands. [45]

With the silicon additive, the yield and tensile strength of the steel increases with the solid solution strengthening mechanism as shown in Figure 2.12. At the same time, silicon additive increases the amount of uniform/total elongation like aluminum [45,46].

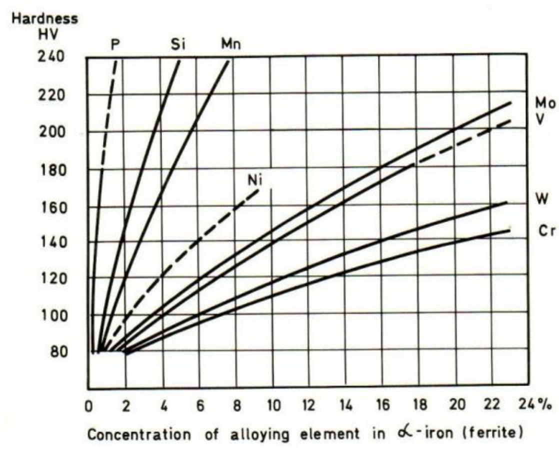

Figure 2.12. Effect of substitutional alloying element additions on ferrite hardness [42]

It has frequently been suggested that the improved work hardening rate of silicon-alloyed ferrite throughout the entire strain range is responsible for the retention of excellent ductility in silicon bearing DP steel.

Greater uniform elongation and a better tensile strength-ductility balance of DP steels at higher Si content are the results of higher strain hardening.

2.1.7.3 Effect of Manganese

Almost all alloying elements, in general, reduce the amount of eutectoid carbon as shown in Figure-2.13. In particular, the effect of this feature causes the addition of Mn to increase the austenite volume fraction attained at the same temperature by decreasing the A1 temperature. The element Mn is known as a potent austenite stabilizer and encourages greater austenite hardenability values. The ferrite formation phase lines change to lower temperatures and slower cooling rates as the manganese content in the steel increase [47].

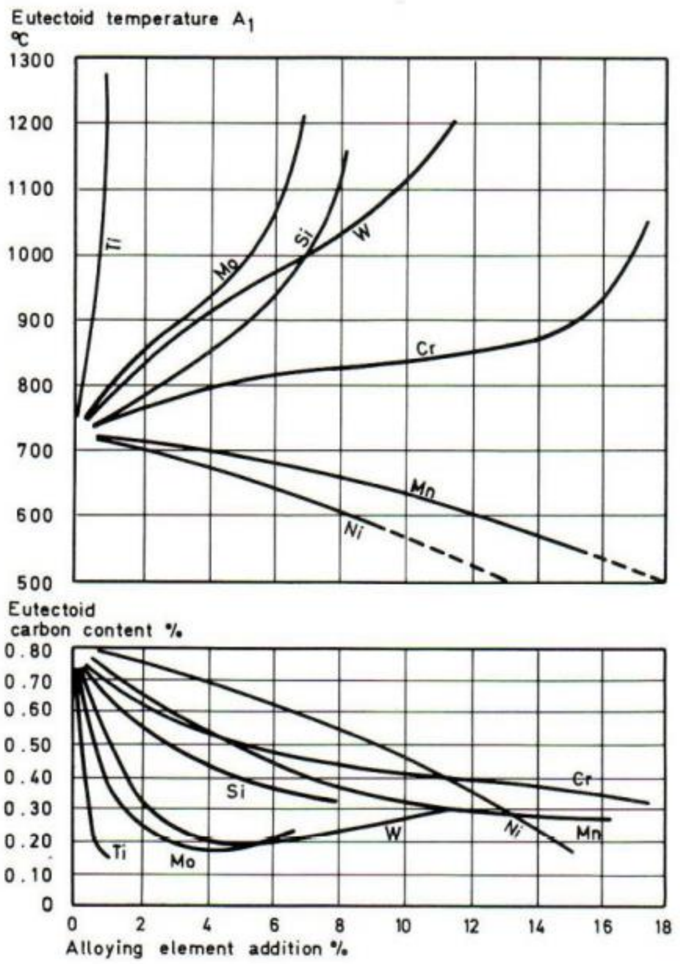

Figure 2.13. Influence of alloying element additions on the eutectoid temperature and the eutectoid carbon content [42]

Manganese partitioning coefficient increases with the increase in temperature. As the IAT increases, the solubility of manganese in ferrite and austenite decreases. Similar behavior can be seen with the addition of silicon content.

The reason for the increase in the concentration difference of manganese dissolved in ferrite and austenite with silicon addition is due to simultaneous promotion of ferrite formation with silicon addition and austenite formation with manganese addition. In such a case partitioning of manganese to the austenite and silicon to the ferrite is expected [44].

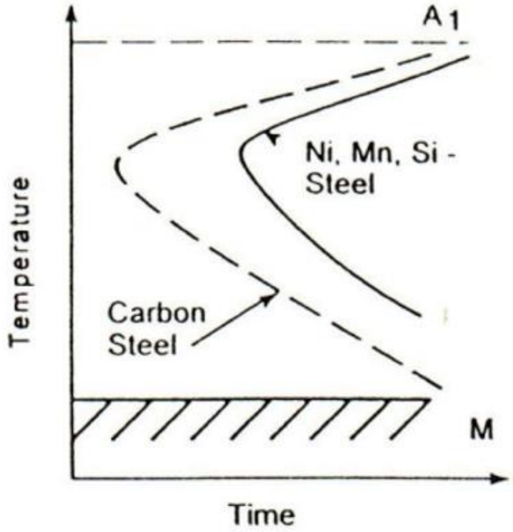

Figure 2.14. Diagrams of isothermal transformation. (a) Effect of non-carbide-forming alloying elements on carbon steel [42]

For example, significant increase in volume fraction of austenite at the same temperature of annealing caused by increasing manganese content is induced by gradual lowering of the Ac1 temperature. This is opposite to the effects of Si and Al additions that raise Ac1.

Manganese also has an important role in refining the grain size of austenite. This effect can be triggered by several mechanisms. Factors such as increasing the stability of austenite with manganese addition and decreasing Ac1 temperature, the growth of the $\alpha + \gamma +$ cementite phase region where grain growth is difficult, the pinning effect of the refined cementite and the reduction of grain boundary mobility with the solute drag effect together allow the grain size of the austenite to be refined [48,49].

Likewise, Mn addition also contributes positively to the attainable uniform elongation value of the steel, as it increases the mobile dislocations at the martensite-ferrite interface, which can be obtained at lower temperatures [31].

Moreover, due to substitutional solid solution effect Manganese slowdowns the reaction kinetics as expected. Quantitative effect of manganese on transformation kinetics can be seen in Figure 2.14.

2.1.7.4 Other Elements

Molybdenum shows the strongest effect in stabilizing austenite. Therefore, austenite can be obtained with the lowest cooling rate by adding Molybdenum. It can be said that the effect of molybdenum on austenite stability is 2.6 times of Mn and 1.3 times of Cr[24,34]. The strong effect of molybdenum is due to the higher hardenability values of austenite [48,49].

In terms of tendency, the chromium effect is comparable to that of Mo, although less potent. Cr additions improve austenite's hardenability capacity and slow down the rate at which ferrite transforms.

If we look at the effect of alloying elements on the martensite start temperature, we can start from the created empirical equations. The following equation demonstrate that carbon, manganese, chromium, and silicon, in that order, have the largest effects on Ms.

$$Ms(°C) = 571-474.4C-33Mn-17Ni-17Cr-21Mo \quad \textbf{\textit{(Eq.5)}}$$

$$Ms(°C) = 538-317C-33Mn-11Si+30Al \quad \textbf{\textit{(Eq.6)}}$$

During heating or holding in the inter-critical temperature range, as well as during subsequent cooling, fine particles of special carbides and carbonitrides can precipitate in steels containing carbide or nitride forming elements, such as niobium, titanium, zirconium, aluminum, molybdenum, and vanadium.

The heat treatment parameters used to produce cold rolled DP steels reduce potential reinforcement by dispersed particles since pre-existing precipitates containing Nb become coarser. However, Nb, which is used to control the grain size in hot rolled steels, can be used to keep ductility at good levels, as well as increasing strength. The effect of microalloying of DP steels with Nb or Ti can be attributed to the combined effect of structure improvement and precipitation hardening. Niobium's strength is combined by raising the austenite content at the same inter-critical annealing temperature, partially preventing ferrite recrystallization, and refining the grain structure [32]. After recrystallization of ferrite is complete and the austenite fraction is approximately reached, the equilibrium strengthening effect of Nb becomes less pronounced as the temperature rises to A3.

Considering the boron addition, which can be used in steel in low amounts, it suppresses the ferrite formation and promotes the higher fraction of austenite at given parameters of annealing.

2.1.8 Bauschinger Effect

In 1881, Bauschinger discovered that, after deforming a metal with a uniaxial tensile test, the yield stress of the metal decreased with the following compression test. Since that day, this phenomenon is known as Bauschinger effect. Bauschinger Effect represents the change in a stress strain characteristic of a plastically deformed metal due to microscopic distribution of dislocations depending on the direction of plastic flow. Generally, two types of mechanism are used to explain Bauschinger effect depending on the microstructure of the material [50,51]. First is the local back stresses which affects the movement of dislocations in the reverse direction. Back stresses develop due to mechanical properties differences between the embedded particles and the surrounding matrix material with 2 main sources Orowan loops and mechanical incompatibilities of different phases. With the aid of local back stresses yield stress drop is triggered in the metal due to easy dislocation movement [51]. Second if the strain direction is reversed, dislocations with the opposite sign may be produced from the same source. Opposite sign dislocations attract and annihilate each other which decreases the strength of the material. As a result, yield stress of the material at the opposite direction is measured lower than it would be if the strain had continued in the forward direction [52].

It has been shown in previous studies that the Bauschinger effect is much more effective in multi-phase materials than pure metals and the effect is linearly proportional to volume fraction of harder phase and the amount of forward pre-strain[53,54]. This is due to the very high long range internal stresses between two mechanically very different constituents formed by misfit strain as compared with the internal stresses in single phase materials. (Bausch-b). DP steels show remarkable BE depending on the deformation history and amount of pre-strain. Main origin is generally developed back stresses due to lang range internal stresses which has a dramatic influence on work hardening behavior[55]. In that case material model excluding BE in DP steels lead misleading results.

Although permanent softening is determined by some of the previous workers on DP steels, it is not detected by others. This is because of the different mechanical behavior of materials due to differences in volume fraction, strength and morphology of the phase colonies.

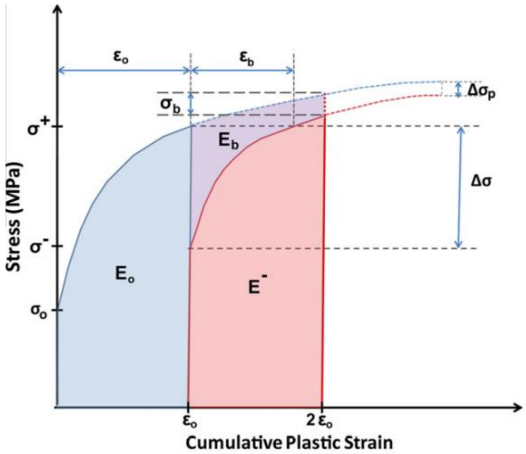

Figure 2.15. Absolute reconstructed stress vs. cumulative plastic strain diagram and schematic representation of Bauschinger quantification parameters[55]

Previously, Weiss et al.[7] reported the results by applying compression-tension, uniaxial tensile and shear tests on samples with different VM ratios in one of his studies to show the Bauschinger effect. When looking at Figure 2.15 and Figure 2.16 taken from that article, it can be seen that there are differences between the stress-strain flow curves obtained from uniaxial tensile and continuous compression-tensile tests applied on two different samples shown as M3 and M2c. Especially when looking at the compression-tension cyclic test data, it can be seen that there is a decrease in yield strength due to the Bauschinger effect in both samples.

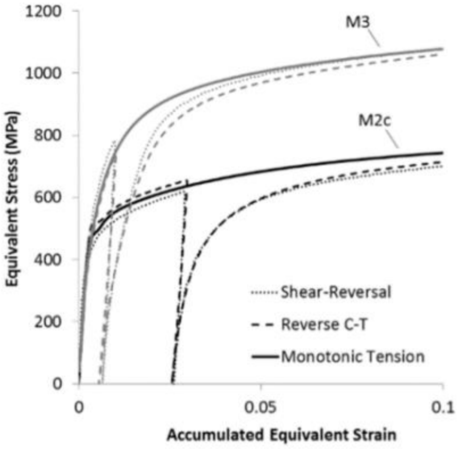

Figure 2.16. Comparative uniaxial tensile, compression-tensile and shear test data for M3 and M2c samples (Proje, Ref = Weiss et al)

The main factor in the development of DP steels is the improvement of its mechanical performance without compromising formability and weldability. Therefore, most of the publications in the literature are related to research and development studies related to mechanical performance. As stated in the previous sections, these improvements are closely related to the microstructure and the following machining process.

In such a case, a modeling that does not consider the microstructure will not be very meaningful, multi-scale microstructure included modeling approximation is used in the scope of this thesis which is motivated by calculating the macro-scale mechanical behavior of DP steels.

2.1.8.1 Quantification of Bauschinger Effect

It is shown that Bauschinger effect is the function of several parameters like temperature, material texture, amount of pre-strain and loading path of the material.

Physical behavior of Bauschinger parameters are sourced by generalized short-range and long-range microstructural interactions. Long range interactions include Orowan loops, dislocation pile-ups near the grain boundaries and strong precipitates. The short-range interactions are originated by dislocation resistance to motion and dislocation annihilation. Many experimental and theoretical efforts have been devoted to studying the Bauschinger effect in bulk metals since the phenomenon was first reported.

Figure 2.17 and Figure 2.18 represents the two characterization stages of Bauschinger Effect. First stage represents the transient Bauschinger deformation composed of work-hardening stagnation which is seen up to a certain range of pre-strain and re-yielding. At the second stage, permanent softening can be defined by stress offset after transient period.

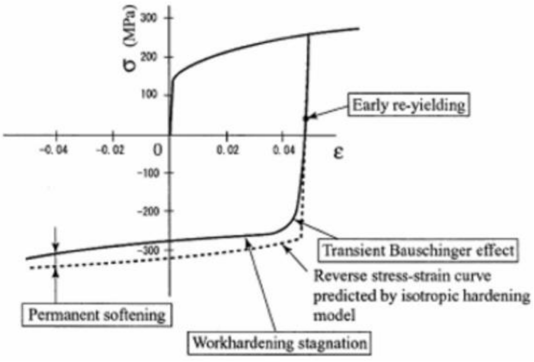

Figure 2.17. Stress-strain curve for Bauschinger tension-compression test and representation of Bauschinger effect related phenomenons[56]

Many different definitions have been used in previous studies to quantify the Bauschinger effect [57,58]. Caceres and Abel defined the Bauschinger energy parameter (BEP) to describe the relationship between isotropic and kinematic hardening, and the Bauschinger stress parameter (BSP) to express the amount of back stress caused by dislocations on the matrix.

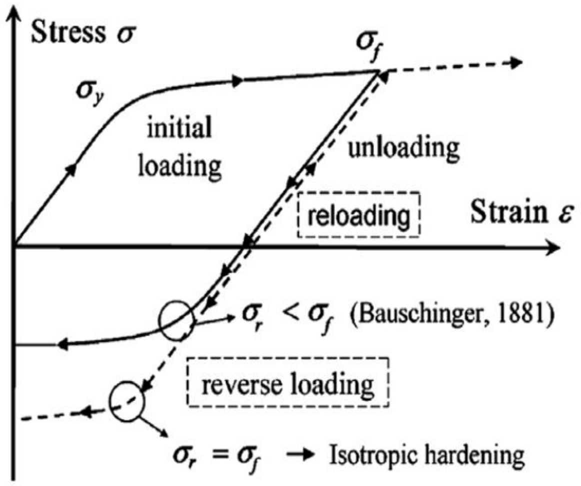

Figure 2.18. A stress–strain curve that exhibits the Bauschinger effect for typical metallic alloys[59]

$$BSP = \frac{|\sigma f|-|\sigma r|}{|\sigma f|} \quad \text{(Eq.7)}$$

$$BEP = \frac{|\sigma f|-|\sigma r|}{2|\sigma f|-|\sigma y|} \quad \text{(Eq.8)}$$

Where σf is the forward pre-strain stress, σr is the reversal stress, σy is the forward yield stress.

In another article examining the Bauschinger behavior of an Aluminum 2024 alloy, the Bauschinger concavity parameter was defined, and it was examined under different age temperatures to see where it was maximized. Also, the internal state variable model (ISV) has been used to measure plastic deformation in many different metals which taking into account the nucleation, growth, and coalescence[10,60]. With the implementation of the method to FEA it has been used in many material models for quantification[54,60].

The major problem with the parameters proposed to date is that the parameters often do not represent the entire Bauschinger effect. The parameters used are generally used to characterize only one or a few aspects of the effect. This is one of the factors that makes it difficult to compare the spring back behavior of different samples show the Bauschinger effect[55].

In addition, due to the complex interactions among the mechanisms, a specific quantitative comparison method could not be established. In this thesis, Bauschinger stress, Bauschinger strain, Bauschinger Energy parameters and B* parameter representing the isotropic hardening relationship of kinematic hardening is used to quantify the Bauschinger behavior of materials.

2.1.9 Motivation of Modeling of Process Chain Simulation of DP Steels

Considering all these information above, it is seen that thermodynamic, metallurgical, kinetic and physical processes change the properties of materials by acting together. Therefore, it can be said that it creates a multifaceted and complex problem.

In such a case, modeling and simulation, as an alternative to the experimental methods used to collect the material data needed in industrial processes, promises the infrastructure and equipment that can provide the data with lower costs and less time. Modeling techniques in micro scale, meso-scale, continuous media scale and finally macro scale may enable us to reach consistent results by taking into account the necessary factors with the help of several modeling software. In other words, it can be said that the contribution and effect of the thesis is hidden in its method.

Thermodynamic Modeling Methods

Calculation of Phase Diagrams (CALPHAD)

A phenomenological method known as CALPHAD is used to compute and predict the thermodynamic and kinetic properties of multicomponent material systems.

It is based on the characteristics of the phases, which are the essential components of materials. By beginning with pure elements and binary and ternary systems CALPHAD makes predictions about the properties of higher order alloys using extrapolation. The CALPHAD approach has been successfully applied throughout the years to the development of many "real" engineered materials and became an important modeling tool in many industrial areas.

Working principle of THERMOCALC software with underlying CALPHAD method can be found at Figure 2.19.

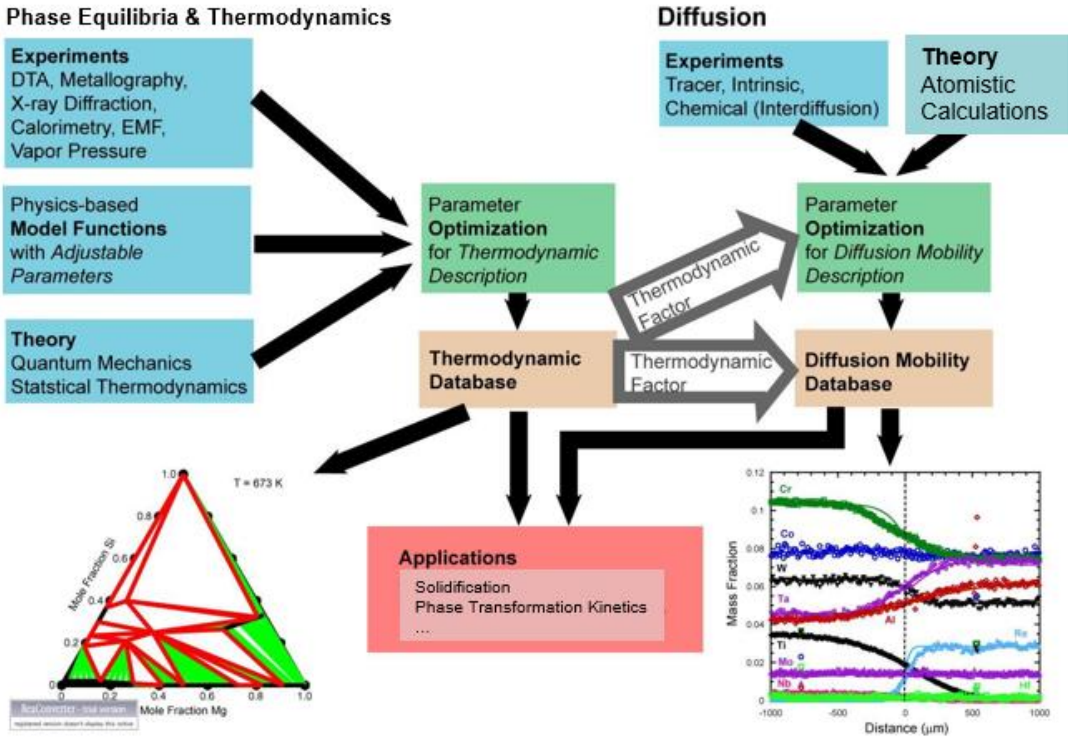

Figure 2.19. Working principle of THERMOCALC software [61]

In order to be able to model thermodynamics, it is of great importance to understand the thermodynamics underlying the potential transformations and phase equilibria of materials. Phase diagrams have always been among the main guides in the direction of material design and development and most materials have more than two or three components, which makes it difficult to describe these systems graphically and hence limits their usability. Furthermore, phase diagrams are frequently only partially understood at best for many multicomponent systems.

Computational methods of thermodynamics have filled a big gap in this regard, especially since it is very difficult to analytically represent and solve systems containing 4 phases or more. Also, development of conventional materials and manufacturing processes takes time and money. The CALPHAD approach was early recognized as a significant tool for alloy production because modeling the behavior and qualities of a material requires an understanding of the phases that are present and their compositions.

The CALPHAD is the only one available method for effective calculations in multicomponent, multiphase systems with the level of precision required for real-world applications. In addition, metastable equilibria and the forces that promote the creation of stable phases can both be calculated through CALPHAD computations. Consequently, the CALPHAD approach has become a crucial tool for numerous sectors and a component of what is now known as ICME (Integrated Computational Materials Engineering)[62].

However, thermodynamic modeling methods do not give information about reaction times, even though they calculate phase diagrams and what will happen in equilibrium states well. Since the benefit from time and cost in the industry is of great importance, it is very important to know how long a reaction will take place, especially in industry-related issues. For this reason, mobility databases that can produce solutions with multi-component diffusion equations have been added to software that makes thermodynamic modeling[63]. The diffusion mobilities were derived from a different database that was identical to the one for the thermodynamics, whereas the thermodynamic factor was obtained via simulations of thermodynamic equilibrium. Recent years have seen attempts to describe molar volume, bulk modulus, and other parameters using the same methods [63].

When considering the kinetic calculations in the CALPHAD method, two different databases are used in the calculations. The reliability of the data in the database is of great importance in terms of properly solving the models. By making solutions according to Gibbs energy component relations with the data coming from the thermodynamic database, the interface equilibrium states are calculated. At the same time multi-component diffusion problems are solved with Fick's equations, taking into account the mobility coefficients with the data coming from the mobility database. Then, the data processed from these two databases are used together to create a flux balance solution. In this way, solutions can be produced for models such as the moving phase boundary model, coarsening model, dispersed system model and cooperative growth model.

Micro Mechanical Modeling

Most of the micromechanical modeling involves numerical simulation of small material volumes. While modeling the effect of the microstructure on the mechanical properties, first the purpose of establishing the model and the scale or scales to be used should be decided. The work performed here is generally divided into 3 categories, as shown in Figure 2.20 [21,64].

a) First, critical production stages and performance prediction is determined and modeled according to average material properties.
b) Second is named as micro-macro transition, typical flow curves which gives the general material behavior can be found by considering and modelling the strain hardening behavior, microstructure properties and the texture.
c) In the third, the simulations focus on the local mechanical behavior of the material. At this microscale, the physical and microscopic origin of DP steels is simulated by considering particle orientation and shape, interface properties, interphase/intergranular gradients.

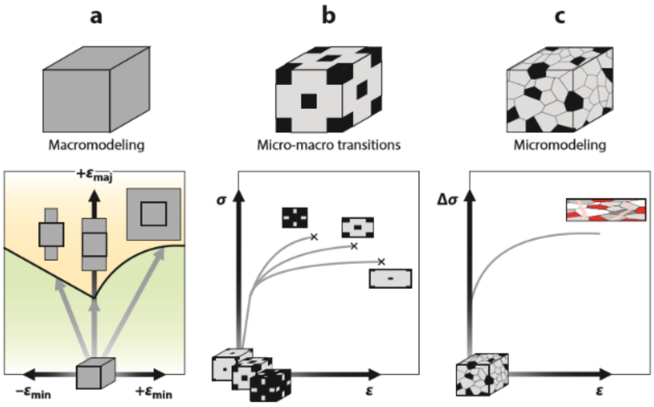

Figure 2.20. a) Component-based macro modeling, general yield-based damage modeling b) Micro-macro transitional modeling is generally used for yield curves and strain-hardening modeling c) Texture and microstructure-based full-area micro modeling is generally used to determine the micro-mechanical properties of the material. [22]

Multi-scale modeling, which is applied when going from micro-scale to macro-scale, aims to get results at large scales by evaluating the microstructure data. There are some procedures that must be followed to do this. To make this transition, a structure called the Representative Volume Element (RVE) must be created. According to the definition, RVE can be briefly called as the smallest part of a heterogeneous material that can represent the whole property.

One of the important issues to be mentioned here is the creation of the Representative Volume Element (RVE) shown in Figure 2.21. This structure can be called as the main element used in the transition from micro scale to macro scale. This transition can generally be reduced to 3 stages as seen in Figure 2.20:

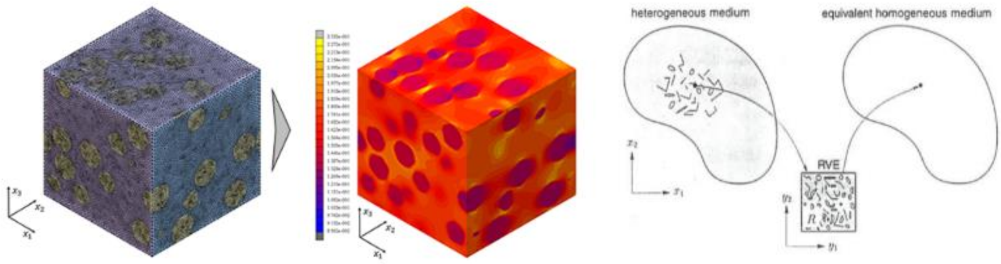

Figure 2.21. a) Schematic representation of RVE b) Schematic representation of micro-macro transition[22,65]

1- First, the RVE definition is made, the volume element should be large enough to represent the entire microstructure and small enough not to prolong the calculation time.

2- Consecutive mechanical modeling definitions are made separately for each phase.

3- Certain "homogenization" strategies are followed to see macro behavior.

It has been mentioned in the previous sections that DP steels exhibit a composite-like behavior due to their microstructure. Many different methods have been used for composite modeling and homogenization since the past. One of the most basic approaches used in composite modeling is Rule of Mixtures based on the Voigt-Reuss approximations. And it assumes:

$$\sigma c = \sigma 1V1 + \sigma 2V2 \text{ (longitudinal loading) } \textbf{(Eq.9)}$$

$$1/\sigma c = \sigma 1/V1 + \sigma 2/V2 \text{ (transverse loading) } \textbf{(Eq.10)}$$

$$\text{where } V1+V2 = 1 \textbf{ (Eq.11)}$$

which can be used to find to upper and lower bounds of the composites assumes isotropic uniform strain inside the RVE under longitudinal loading with parallel fibers and isotropic uniform stress inside the RVE under transverse loading with perpendicular fibers. In this case, if each phase is isotropic, both models predict an isotropic composite, regardless of the shape and orientation of the inclusions, which is physically false. But in fact, in DP steels due to random distribution of martensite on soft ferrite matrix, an alternative mechanical deformation behavior takes place and stress-strain distribution between two mechanically different phases neither stresses nor strains are identical. Softer ferrite phase deforms while deformation on martensite is low and stress increases at the interface of these two phases as the applied load increases. For such a complex deformation mechanism which has proven experimentally rule of mixture is not sufficient to give accurate results. Since there is no physical approach to formulate the effects of microstructural parameters on fracture behavior in heterogeneous materials, experimental validation is generally needed.

Later, with time, more sophisticated methods emerged and the Hashin-Strikhman boundaries were defined as the narrowest limits where the moduli of any double-phase composite could be defined as in Figure 2.22[66].

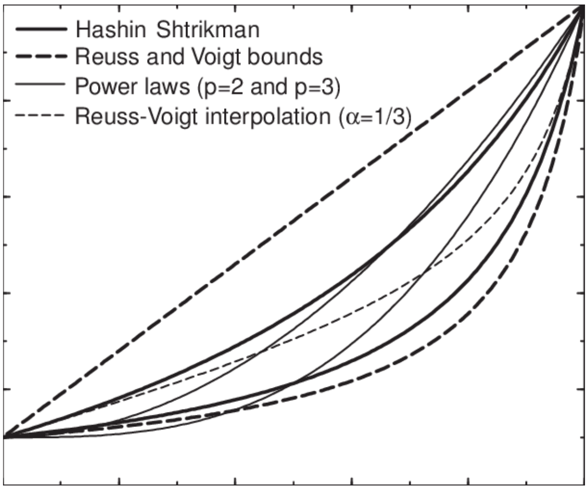

Figure 2.22. A comparison of the Voigt upper and the Reuss lower bound, the Hashin-Strikhman upper and lower bound[67]

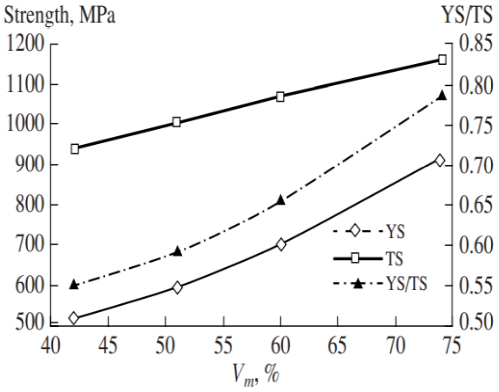

Figure 2.23. The effect of the volume fraction of martensite on the values of the yield strength, tensile strength and their ratio in DP steels[31]

Due to the geometrical constraints encountered in composite models made in finite element solutions, the difficulties encountered in the solution of high-volume composite particles and fibers with high aspect ratios, micro-mechanical models have begun to increase their importance as an effective solution tool. Instead of relying on trial-and-error experiments, they use the derivation of the macroscopic behavior of new materials while taking into consideration the microstructural parameters of each phase, which requires less computation time than direct bridging techniques[10].

The earliest approaches on the subject are based on methods calculating macroscopic stress from direct macroscopic strain by analytical methods. A second approach is based on explaining the effective potential of the composite with the use of derivatives in stress-strain relations. However, these approaches based on linear analyzes according to the load carrying capacity of the material cause serious design errors due to their limitations. To create better models without compromising such errors and structural integrity, non-linear analysis solutions have emerged.

Later, many methods have been developed to account for intergranular heterogeneity in elastoplastic material modeling. Self-consistent (SC) formulation developed by Hill [68] based on Kroner[69] is used in polycrystal elastoplastic materials by Iwakuma[70] and Lipinski by taking the deformation into account. However, among all these procedures, the method based on Eshelby tensor estimation yielded the most consistent results in two or multi-phase elastoplastic composites with different shapes and sizes of reinforcements.

According to Eshelby’s solution at Figure 2.24 an ellipsoidal volume within an infinite solid body is cut out and it undergoes an stress free eigenstrain (ε^*) and is welded back into the body. Eshelby found that the strain inside the ellipsoidal volume “I” is uniform and related to the eigenstrain as follows:

$$\varepsilon(x) = \zeta(I,C_0):\varepsilon^*, \quad \forall x \in (I) \quad \textbf{(Eqn.12)}$$

If C_0 is isotropic and (I) is a spheroid, then Stiffness dependence is through Poisson’s ratio only. Shape dependence through the aspect ratio only. Eshelby’s solution plays a fundamental role in MFH, as it enables to solve the MFH problem.

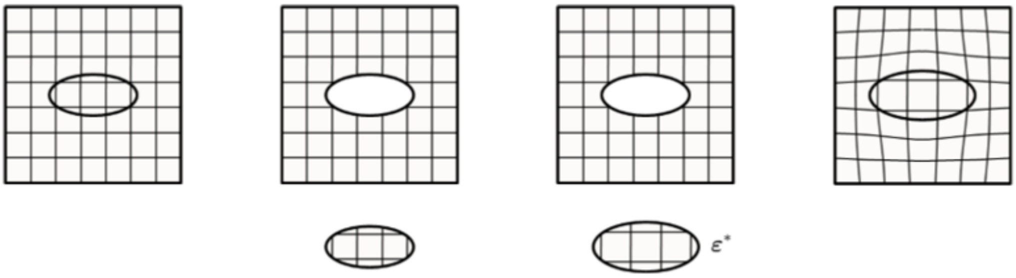

Figure 2.24. Eshelby’s problem: An ellipsoidal volume within an infinite solid body of uniform stiffnes is cut out, undergoes an eigenstrain and is welded back into body

Within the scope of the thesis, two different methods are used in the homogenization stage of the micro-macro transition. The first of these is the MFH method.

MFH is the semi-analytical homogenization approach used to compute thermal and mechanical properties of a composite material. It predicts volume averaged micro-level solutions in each constituent of the composite; with formulations based on

Eshelby's solution. Method has advantages like ease of use, high efficiency in terms of computational point of view and reduced memory usage. Also, the MFH method has not been used to calculate the mechanical properties of metals before. But MFH does not solve the RVE problem in detail therefore does not compute the detailed micro stress and strain fields in each phase. Also, it cannot take into account clustering, percolation and size effects.

Second method is the Finite Element Analysis-Representative Volume Element (FEA-RVE) method. Although this method has been frequently used to calculate the mechanical properties of materials before, it has not been made by relying on thermodynamic modeling data, which takes into account the microstructure of the material. The method, which provides a much more detailed analysis compared to MFH and gives the results of local stress-strain analysis, is used as the second homogenization method in the thesis. In the previous FEA-RVE literature studies, Abbasi[10] used this method in a study to model the effect of different distribution and size of martensite particles in DP steels by creating axis-symmetrical models. Likewise, studies on this subject have been carried out in universities such as Middle East Technical University (METU) and Gazi University in our country. Yalcinkaya et al. performed a micromechanical based numerical analysis of DP steels in a study and examined the effect of microstructural properties on plasticity and local deformation. In a study conducted at Gazi University, RVE modeling of DP600, DP800 and DP1000 steels was performed to examine the stress strain relationship in DP steels by Çavuşoğlu et al [71].

CHAPTER 3

EXPERIMENTAL AND MODELING METHODS

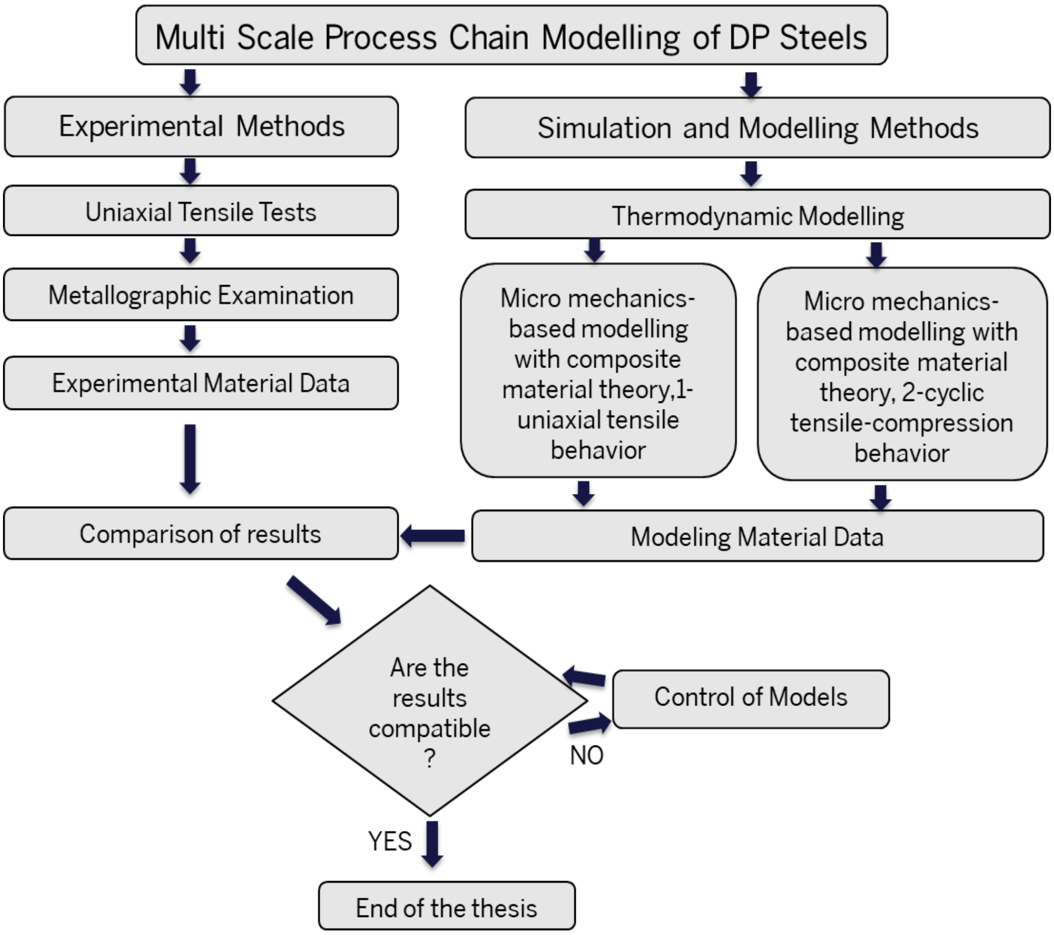

Figure 3.1. Flowchart of the thesis

3.1 Mechanical and Metallographic Test Methods

3.1.1 Chemical Composition

Mechanical tests and microstructure characterization are the two primary categories of experiments that were performed for the project. Within the scope of the thesis, DP600 and DP800 steels with different chemical compositions, produced by 2 different methods (hot rolled, cold rolled) and supplied from 2 different manufacturers (SSAB, BORÇELIK) are used.

The sheets produced by hot rolling are supplied by the SSAB company, while the sheets produced by cold rolling are provided by our domestic manufacturer BORÇELIK. In this way, the effect of different material manufacturing processes on material performance are determined and a detailed verification with the models are made. Chemical compositions of 4 specimen provided by manufacturers can be found in Table 3.1.

Table 3.1 Chemical Composition of DP Steel Specimens

		%C	**%Si**	**%Mn**	**%Al**	**%Ni**	**%Cr**	**%Mo**	**%V**	**%Nb**
1	**SSAB-DP600**	0.10	0.28	1.5	0.04	0.04	0.02	0.01	0.01	0.0002
2	**BOR-DP800**	0.14	0.21	2.0	0.03	0.02	0.23	0.02	0.004	0.0007
3	**BOR-DP600**	0.09	0.24	1.9	0.03	0.02	0.20	0.01	0.003	0.0005
4	**SSAB-DP800**	0.13	0.19	1.5	0.04	0.03	0.04	0.01	0.015	0.013

3.1.2 Uniaxial Tensile Test

Steel sheets are tested at room temperature in the ZWICK-ROELL compression-tension test machine (Figure 3.2), which can operate at 1-250 mm/min tension speeds.

In accordance with the rolling direction, DP600 and DP800 alloy sheets supplied from the manufacturers are cross sectioned in 0° and 90° directions and tensile test specimens are prepared. ISO 6892-1 tensile test guide for metals followed in the preparation of the test protocol and test specimens. The two directional extensometers are used on the tensile devices to see the deformation in the material in 2 different axes. As a result of these experiments, stress-strain curve of the materials under uniaxial tension at 0° and 90° obtained.

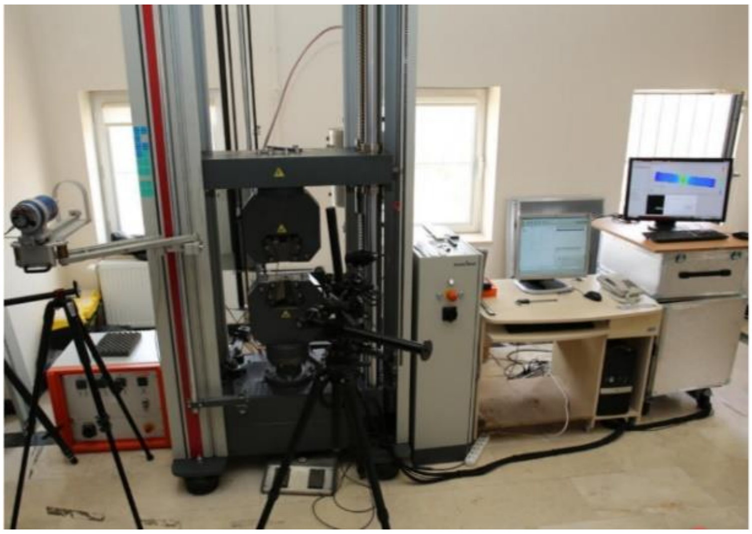

Figure 3.2. Zwick Roell Tension-Compression Test Equipment

3.2 Microstructural Characterization

Optical Microscope (OM) used for microstructural characterization of DP steel specimens. After steel specimens are prepared for the process specific method, they are tested accordingly. Average grain size, grain geometry, grain (geometric) orientation and distribution of martensite grains are determined by taking sufficient number of photos from different parts of the samples by using OM.

ASTM E112 standard, which is used for calculating grain sizes by image analysis methods, is used as a guide. In order to microstructure analysis to be representative, at least 7 microstructure photographs from each sample are examined. For the results to be representative, the number of samples or the analyzed interior photos are increased to the point where the relative (standard) deviation is less than 12% as specified in the ASTM E562 standard.

Metallographic analyzes are performed on samples taken from 2 different sections (parallel to the rolling direction and perpendicular to the rolling direction) in order to determine the 3-dimensional grain structure in DP steels. After taking a sufficient number of photographs that reduce the standard deviation below a certain ratio from the microstructures, the phase ratios in the steels were found by image processing method with the help of ImageJ software.

3.3 Modelling and Simulation Methods

In the first phase of the project, the main focus is the IA process. First, the microstructure of the material is determined by computational thermodynamics/kinetics methods. Then, Thermodynamics Based Material Property Calculation (TBMPC) method as mentioned in Liu et al.'s[72] is employed to determine mechanical properties of individual phases.

For thermodynamic-based modeling, a method that provides thermodynamic modeling of multi-component materials, also called the CALPHAD method, is used[72].

Calculations are performed with the help of THERMOCALC, JMatPro, MATLAB and diffusion simulation software (THERMOCALC-DICTRA). Modeling is done using a few manufacturing information (chemical composition, intermediate annealing temperature, time, heating and cooling rates, grain size). After then, ferrite/martensite grain sizes, martensite ratio by volume, chemical composition of ferrite and martensite are calculated.

Then, by using the compositions of the phases with the help of Thermodynamic Based Property Calculation Method (TBPCM) elastic properties and true stress-true strain curves are calculated at constant strain rate (0.001 s-1) for ferrite and martensite separately. A calculated example of both separate phases on some DP800 steel is shown in Figure 3.3a and Figure 3.3b.

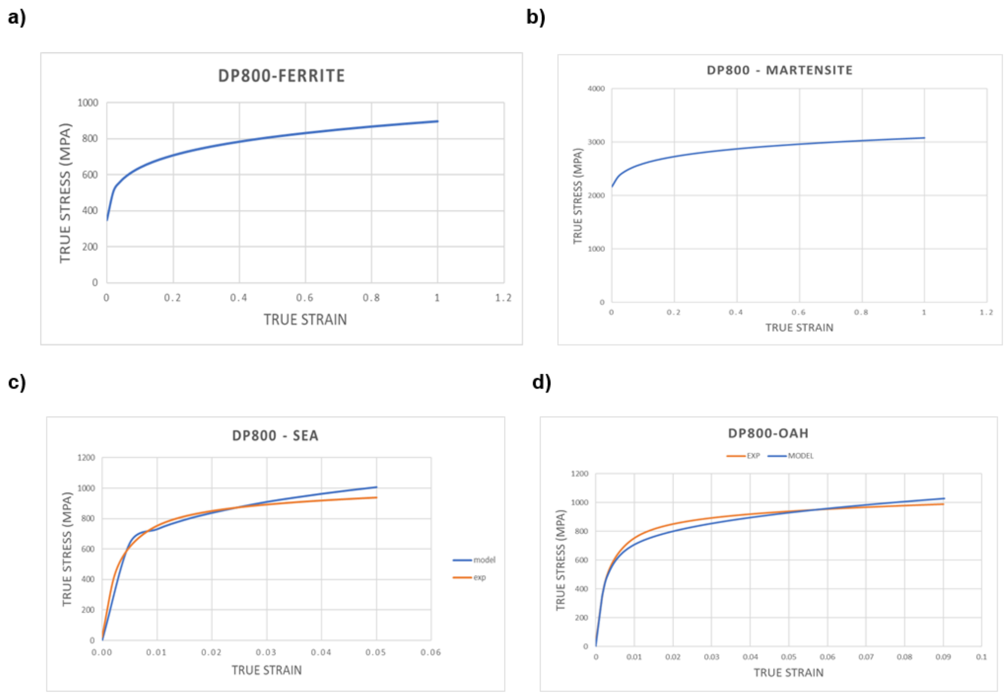

Figure 3.3. DP800 steel at constant strain rate (0.01 s-1) room temperature a) ferrite and b) martensite yield curves and according to these data c) yield curve calculated by FEA method d) yield curve calculated by MFH method and their comparison with experimental data

Then, the extracted data are transferred to MATLAB and processed, and the strain hardening coefficients are found by "Power Law" fitting. As a result, using only a few experimental input data, phase amounts and compositions, elastic properties of phases and yield curves of ferrite and martensite are determined.

In the second phase, macroscopic mechanical properties (flow curve and cyclic hardening behavior) are calculated from the individual properties of phases using the composite material theory. Extracted and processed data is used for micro-mechanical modelling. As mentioned earlier, two approaches are used here: (a) Mean

Field Homogenization (MFH) and (b) Finite Element Representative Volume Element (FE-RVE) Homogenization.

During the modeling, software such as DIGIMAT, MATLAB, Msc.Marc are used and the input values of the phases yield strength, elasticity modules, isotropic/kinematic hardening parameters, length ratio of martensite, volume fraction, distribution, orientations are taken.

Mori-Tanaka scheme, which was found after Eshelby solution, is used as the homogenization scheme for MFH method. As a result, yield curve of DP steel's are obtained. The yield curve of a sample calculated by this method and its comparison with the experimental data can be seen in Figure 3.3c.

The difference of the FEA-RVE method, which is the second method to be used for homogenization, from the first one (MFH) can be shown as solving the problem in detail by performing a much more detailed numerical analysis, calculating the average strain and stress distributions as well as micro stress and strain distributions for each phase. The material data to be used in the solution of this method can be shown as yield strengths, modulus of elasticity, isotropic hardening coefficients, aspect ratio of martensite, volume fraction and distribution and orientations of the phases. An example of the yield curve of one DP800 sample calculated with this method can be seen in Figure 3.3d.

In the creation of RVE, 2D and 3D models are used separately. At the end, mechanical data of DP steel specimens such as yield curve, cyclic loading behavior, stress-strain tensors, total strain, plastic strain Von-Mises stress analysis data are obtained. Some examples of 2D and 3D modeling trial RVE results can be found at Figure 3.4.

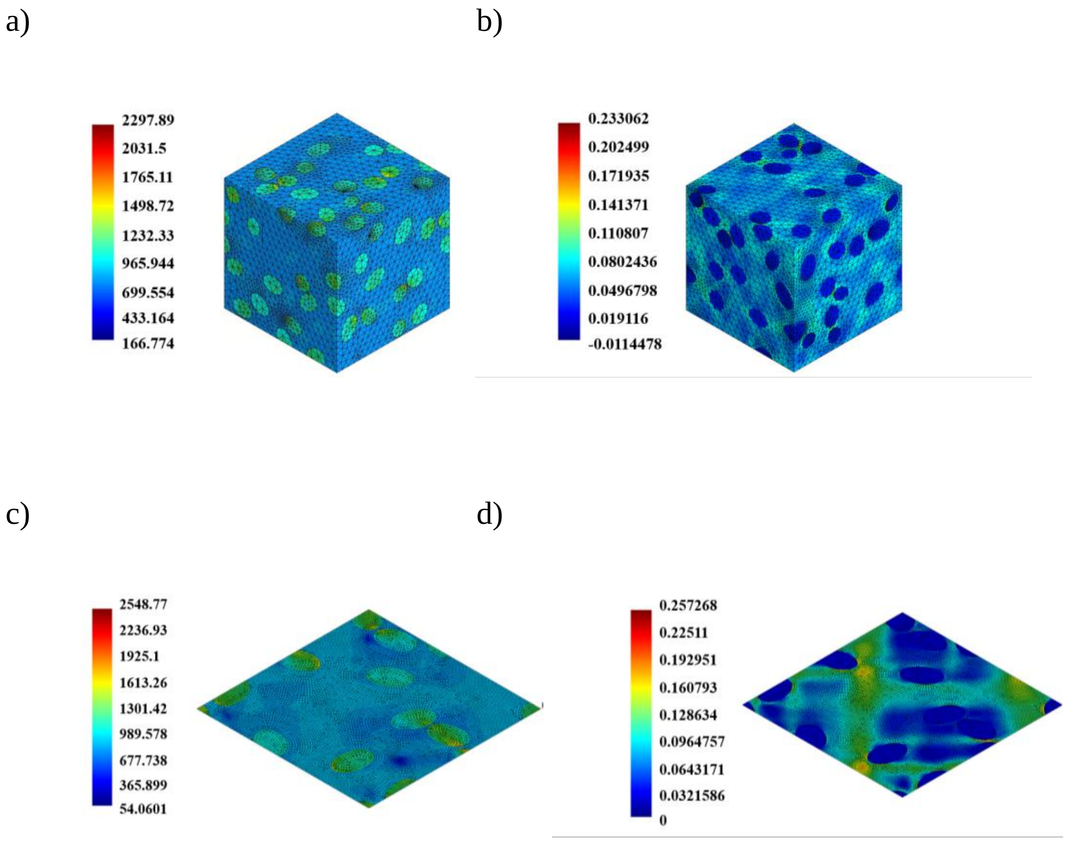

Figure 3.4. Dual phase steel model trials (3D and 2D), specific to phases a) 3D Equivalent Von-Mises stress distribution b) 3D Equivalent plastic strain distribution c) 2D Equivalent Von-Mises stress distribution d) 2D Equivalent Von-Mises stress distribution

In the final phase of the thesis, after the uniaxial tensile test model is applied to BOR-DP600, BOR-DP800, SSAB-DP600 and SSAB-DP800 samples, Bauschinger parameters in all samples Bauschinger stress, Bauschinger strain, Bauschinger Energy and P_{isot} which represents the fraction of isotropic hardening are calculated by cyclic tension-compression loading model.

CHAPTER 4

RESULTS AND DISCUSSION

Results from thermodynamic and mechanical models for DP steel samples are given in this chapter in comparison with experimental data.

4.1 Thermodynamic Modelling

To ascertain the mechanical characteristics of the various stages of ferrite and martensite, TBMPC method is utilized. A few experimental inputs are used to start the modeling process, including chemical composition (Table-3.1), ferrite and austenite grain sizes, and phase fractions.

Thermodynamic parametric analysis and sensitivity analysis are conducted prior to the simulation using the data from real steel samples to understand the relationship between the input and output variables, measure the accuracy of the model, reduce model uncertainty, simplify the model by removing the data that does not cause turbulence in the output results, and for optimization.

At this part of the model a fictitious DP Steel Composition is used as base.

Modeling procedure flowchart can be seen in Figure 4.1. Green boxes represents the thermodynamical modeling steps.

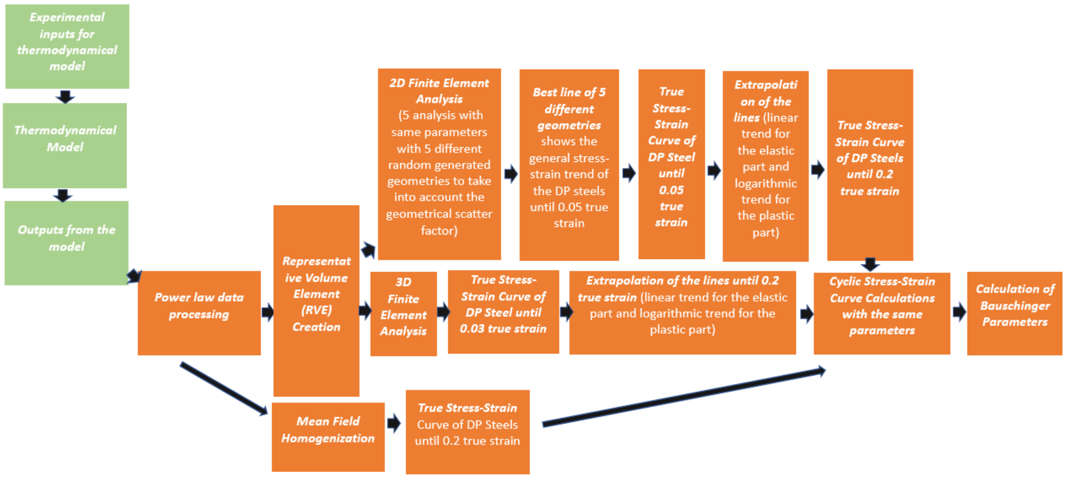

Figure 4.1. Modeling Procedure Flowchart

4.1.1 Thermodynamic Parametric and Sensitivity Analysis

One of the most common approaches in sensitivity analysis is One at a Time (OAT) method. In this method, one variable changes at a time while keeping the other parameters as constants with following equation:

$$F(x) = y \quad \textbf{\textit{(Eqn.13)}}$$

Where F(x) function represents the created model, “x” is the input and “y” is the output value. After sufficient number of inputs are used to see a linear trend in implemented model, dimensionless sensitivity parameters are calculated according to derivative of the trendlines.

Base input values are determined according to average DP steel parameters as follows to represent the DP steel behavior.

Used input parameters are as follows: IAT, %C, %Mn, %Si, grain size, %Cr, %Al, %Mo, %Ni, %Nb, %Ti

To see the change on material behavior of low addition alloys like %Cr, %Al, %Mo, %Ni, %Nb, %Ti, models were run with higher volume fractions than those normally used in DP steels.

These inputs are used for calculations to determine the effects on phase transformation lines, the mechanical characteristics of phases, the distribution of elements among the phases, and the change in phase fractions.

Output parameters are as follows: Ferrite σ_0, Ferrite K, Ferrite n, Martensite σ_0 Martensite K, Martensite n, % Martensite, % Ferrite, %C in ferrite, %C in austenite, %Mn (in fer), %Mn (in aus), %Si (fer), %Si (aus), %Cr (in aus), %Cr (in fer), A1 Temp, A3 Temp, A3-A1 Temp, Ms Temp, Mf, Mf-Ms Temp.

4.1.1.1 Parametric Analysis Results

After thermodynamic model is created, by using each input, turbulence on output properties are calculated. Effect of %Mn on austenite and ferrite formation can be seen in Figure 4.2.

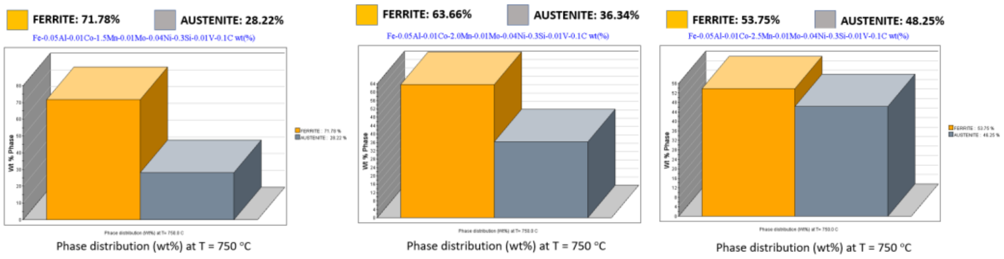

Figure 4.2. Effect of %Mn on austenite and ferrite formation at same IAT, 1.5%Mn (71.78%ferrite), 2%Mn(63.66% ferrite), 2.5%Mn (53.75% ferrite)

Phase fractions and elemental partition in different phases are determined by keeping the IAT fixed. A1, A3, Ms and Mf temperatures and change of pearlite, ferrite and bainite transformation temperatures and time are determined from the TTT curves. One example is shown in Figure 4.3, Figure 4.4 and Figure 4.5 with varying Mn content.

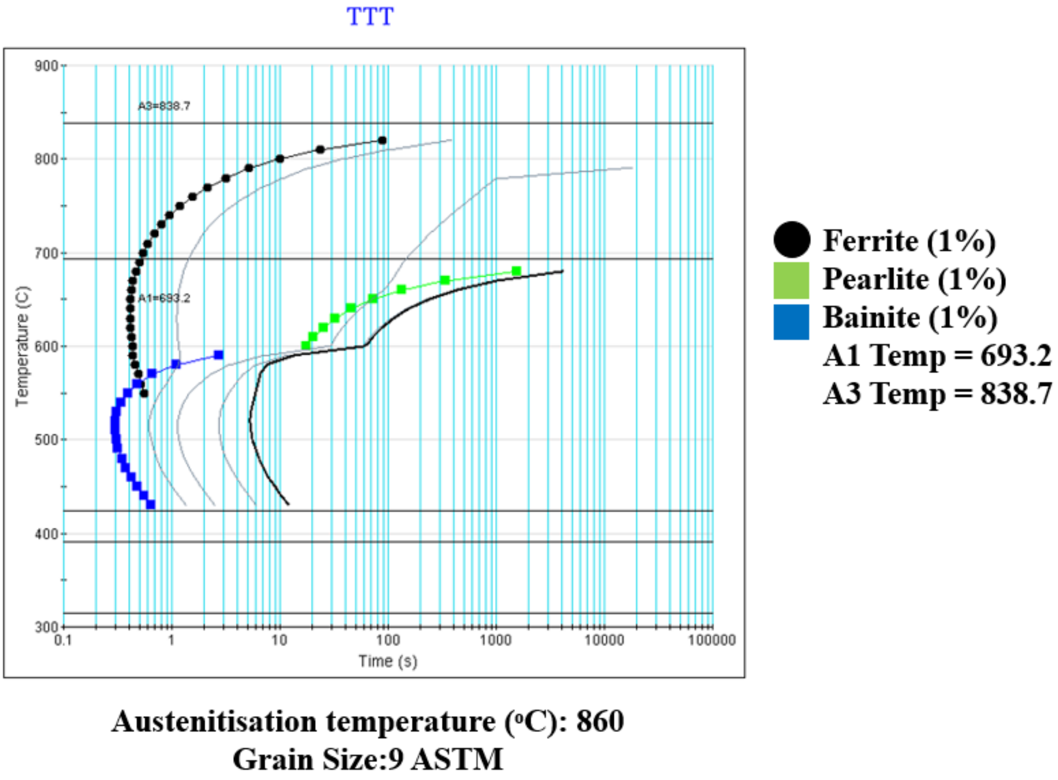

Figure 4.3. TTT curve of fictitious DP steel with varying Mn content, 1.5% Mn

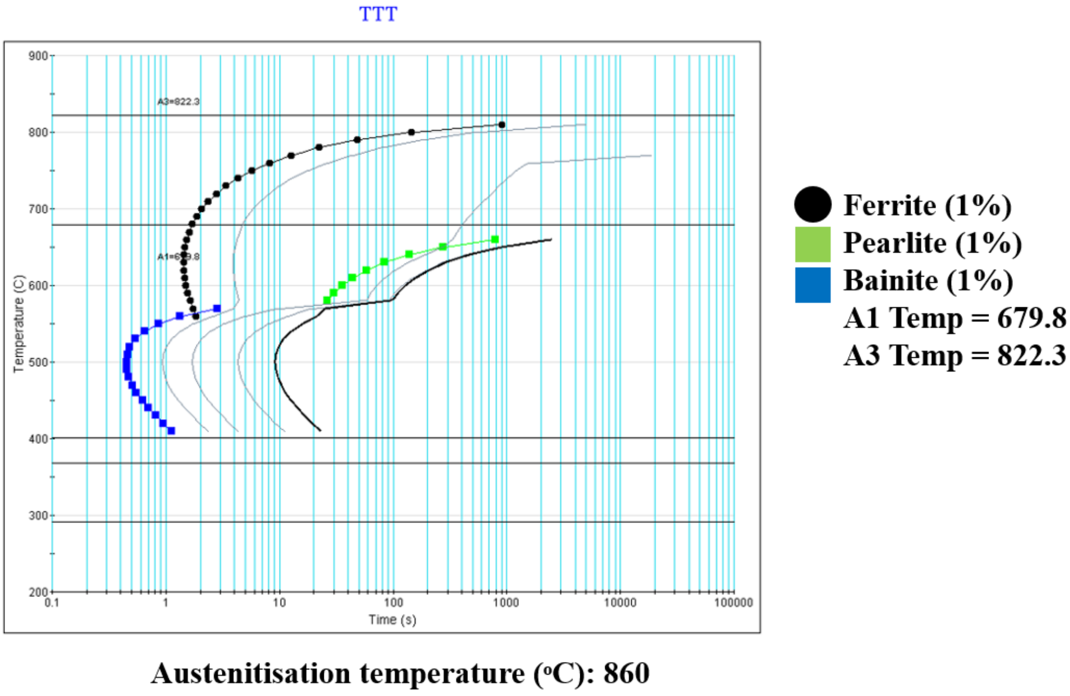

Figure 4.4. TTT curve of fictitious DP steel with varying Mn content, 2% Mn

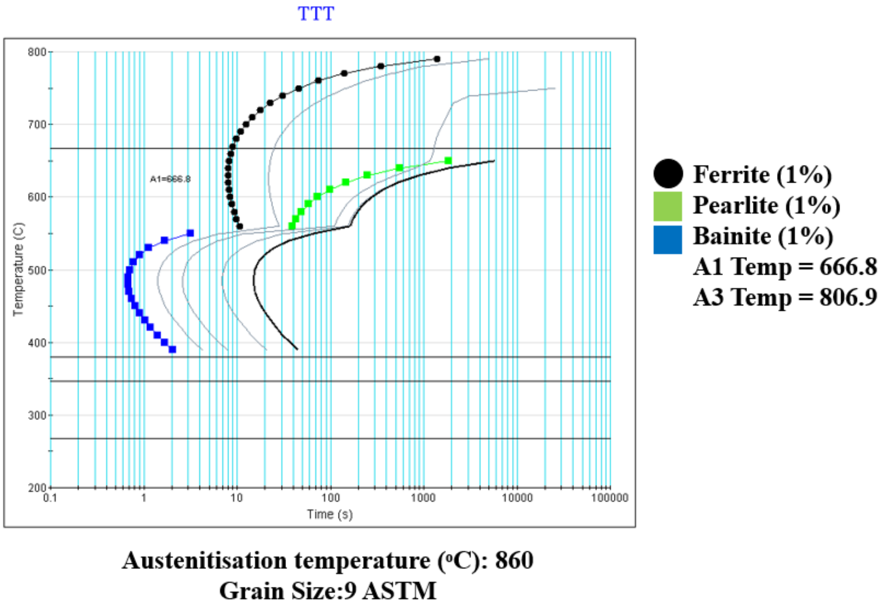

Figure 4.5. TTT curve of fictitious DP steel with varying Mn content, 2.5%Mn

4.1.1.1.1 Effect of IAT

Table 4.1 Effect of IAT on Output Parameters 1

IAT (°C)	Fer σ0	Fer K	Fer n	Mar σ0	Mar K	Mar n	%C_α	%C_γ
715	329	521	0.25	2349	873	0.27	0.0089	0.48
750	306	500	0.25	1765	908	0.27	0.0081	0.39
775	294	490	0.25	1403	900	0.27	0.0075	0.23
790	288	483	0.25	1231	883	0.27	0.007	0.19
800	284	480	0.25	1100	867	0.27	0.00066	0.16
DS	-1.32	-0.79	0.00	-8.29	NV	0.00	-7.23	-13.48

**Fer represents ferrite, Mar represents martensite, NV represents not valid sensitivity analysis output, DS represents the dimensionless sensitivity*

Table 4.2 Effect of IAT on Output Parameters 2

IAT (°C)	%Cr_α	%Cr_γ	%Mn_α	%Mn_γ	%Si_α	%Si_γ	% Mar	% Fer
715	0.22	0.39	1.03	3.42	0.26	0.2	20	80
750	0.21	0.33	1	2.67	0.27	0.2	30	70
775	0.21	0.3	0.95	2.26	0.28	0.21	40	60
790	0.21	0.29	0.91	2.05	0.29	0.22	50	50
800	0.2	0.28	0.88	1.91	0.3	0.23	60	40
DS	-0.74	-3.36	-1.47	-6.17	1.11	-1.11	8.72	-5.81

**DS represents Dimensionless Sensitivity*

According to Tables 4.1 and 4.2, as the IAT rises, the %C, %Mn, and %Ni in ferrite and austenite decreases, reduces the strength of both the ferrite and martensite. Only %Si in austenite and ferrite increases with the increasing IAT since it is a ferrite stabilizer unlike other evaluated elements.

However, while the IAT increases, volume fraction of martensite after quenching increases as well. It is well known that the presence of martensite and the amount of carbon contribute to a material's strength, yet there is an inverse relationship between these two. Due to an increase in the related IAT, dissolved carbon inside martensite decreases as the amount of the material does (Figure 4.6). As a result, there is a trade-off between the IAT and the material's strength. The explanation for this anomaly is carbon dilution, which weakens the aggregate's overall strength by softening the martensite phase.

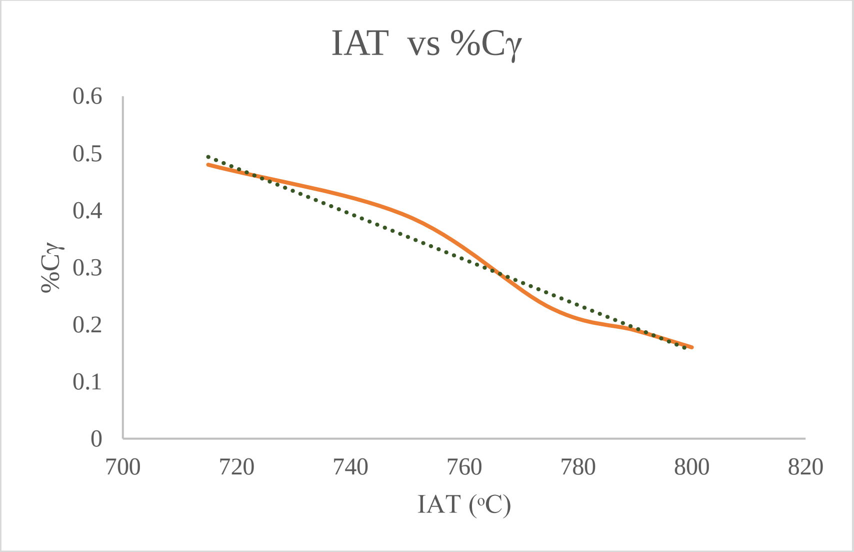

Figure 4.6. IAT (°C) vs %Cγ graph

4.1.1.1.2 Effect of %Carbon

Table 4.3 Effect of %C on Mechanical Output Parameters

%C	Fer σ0	Fer K	Fer n	Mar σ0	Mar K	Mar n
0.05	326	520	0.25	617	715	0.26
0.075	319	512	0.25	724	762	0.25
0.1	314	507	0.25	831	800	0.26
0.125	308	503	0.25	937	831	0.26
0.15	304	498	0.25	1042	855	0.26
DS	-0.070	-0.042	0.000	0.512	0.175	0.000

**DS represents Dimensionless Sensitivity*

Table 4.4 Effect of %C on Chemical Composition

Carbon%	%Mar	%Fer	%C_α	%C_γ	%Mn_α	%Mn_γ	%Si_α	%Si_γ
0.05	14	86	0.007	0.32	1.19	3.31	0.29	0.23
0.075	20	80	0.007	0.35	1.09	3.08	0.3	0.23
0.1	25	75	0.008	0.37	1.01	2.9	0.3	0.23
0.125	30	70	0.008	0.39	0.95	2.74	0.31	0.23
0.15	35	65	0.009	0.41	0.89	2.6	0.31	0.23
DS	0.83	-0.28	0.30	0.24	-0.29	-0.24	0.07	0.07

Table 4.5 Effect of %C on Phase Transformation Lines

%C	A1(°C)	A3(°C)	A3-A1(°C)	Ms(°C)	Mf(°C)	Mf-Ms(°C)
0.25	706	798	92	364	250	114
0.5	717	751	34	270	147	123
0.75	723	743	20	180	44	136
1	724	836	112	90	-60	150
1.25	725	860	135	70	-85	155
DS	0.019	NV	NV	-1.28	-5.98	0.24

**Ms represents Martensite start temperature, Mf represents Martensite finish temperature*

Table 4.6 Effect of %C on Transformation Kinetics

%Carbon	Bain. (°C)	Bain. (sec)	Fer. (°C)	Fer. (sec)
0.5	460	2.5	625	0.3
0.75	425	10	625	0.35
1	400	35	625	0.5
1.25	390	50	625	0.75
DS	-0.049	0.98	0	12.5

**Bain represents bainite phase, fer represents ferrite phase. Transformation temperatures and times at the phase formation noses are given separately*

As illustrated in Table 4.3 transformation rates of formed ferrite and martensite changes prominently with varying carbon content. As the %Carbon increases, more austenite is obtained at the same IAT. As a result, extra martensite is produced after quenching, increases the steel's strength. Because more carbon atoms are locked into the structure during quenching, causes strain in the lattice, the strength of the material increases as the amount of carbon in the solution increases. After the strain has been released, carbon atoms pin the dislocations, preventing further mobility.

Most prominent effect of carbon on austenite is in the hardenability values of the steel. From the Table 4.4 increasing amounts of carbon lowers the Ms and Mf temperatures dramatically, and at the same cooling rates, it provides a steel with higher hardenability. Also, effect of %Carbon on bainite and ferrite transformation rates can be seen in Table 4.5. Increasing %C shifts the bainite formation temperature to lower temperatures.

Likewise, carbon retards the formation of ferrite to some extent. Carbon composition change the rate of new ferrite formation and enrichment of austenite with carbon, shifts bainite transformation to lower temperatures (Table 4.6) and slower cooling rates and results in slightly decreasing MS temperature.

4.1.1.1.3 Effect of %Chromium

Table 4.7 Effect of %Cr on Mechanical Output Parameters

Cr%	**Fer σ0**	**Fer K**	**Fer n**	**Mar σ0**	**Mar K**	**Mar n**
0.15	310	505	0.25	840	803	0.26
0.2	311	506	0.25	843	804	0.26
0.25	312	506	0.25	845	805	0.26
0.3	316	509	0.25	840	803	0.26
0.35	319	512	0.25	834	801	0.26
DS	0.037	0.017	0.000	NV	NV	0.000

**DS represents Dimensionless Sensitivity*

Table 4.8 Effect of %Cr on Chemical Composition

%Cr	**%Mar**	**%Fer**	**%C_α**	**%C_γ**	**%Mn_α**	**%Mn_γ**	**%Si_α**	**%Si_γ**
0.15	25	75	0.008	0.37	1.01	2.88	0.3	0.23
0.2	25	75	0.008	0.37	1.01	2.87	0.3	0.23
0.25	26	74	0.007	0.36	1.01	2.86	0.3	0.23
0.3	26	74	0.007	0.36	1	2.85	0.3	0.23
0.35	26	74	0.007	0.36	1	2.84	0.3	0.23
DS	0.06	-0.02	-0.07	-0.04	-0.04	-0.02	0.00	0.00

Table 4.9 Effect of %Cr on Phase Transformation Lines

%Cr	**A1(°C)**	**A3(°C)**	**A3-A1(°C)**	**Ms(°C)**	**Mf(°C)**	**Mf-Ms(°C)**
1	718	825	107	405	290	115
2	734	814	80	380	265	115
3	744	804	60	370	255	115
DS	**0.035**	**-0.026**	**-0.59**	**-0.092**	**-0.132**	**0**

Table 4.10 Effect of %Cr on Transformation Kinetics

%Cr	**Per. (°C)**	**Per (sec)**	**Bain. (°C)**	**Bain. (sec)**	**Fer. (°C)**	**Fer. (sec)**
1	590	40	500	1	650	0.3
2	610	60	475	2	650	25
3	630	80	460	5	650	60
DS	0.066	0.67	-0.084	2	0	2.39

**Bain, fer and per represents the formation of bainite, ferrite phases and pearlite phase mixture respectively. Transformation temperatures and times at the phase formation noses are given separately.*

Due to same crystal structure with austenite (FCC), Cr decreases the A3 temperature (Table 4.9) and increases the A4 temperature broadens and stabilizes the austenite phase area. The promotion of bainite (Table 4.10) at the expense of high-temperature transformation products like ferrite and granular bainite is another effect of raising

the Cr concentration, as increase in hardenability, which resulted in a decrease in transformation temperatures.
As the %Cr increases %C and %Mn in both austenite and ferrite decreases slightly and shifts the phase transformation lines (Table 4.8) due to solid solution strengthening effect.

If ferrite strengthening is not desirable due to possible decrease in ferrite ductility, addition of Cr for enhanced hardenability is especially advantageous as Cr has little effect on ferrite strengthening (Table 4.7). For this reason, Cr is one of the most convenient alloying elements in steel especially that is to be processed by cold working in which good hardenability is required. Cr addition for this reason can be seen in BOR-DP600 and BOR-DP800 steel specimens in Table 3.1.

4.1.1.1.4 Effect of %Manganese

Table 4.11 Effect of %Mn on Mechanical Output Parameters

%Mn	Fer σ0	Fer K	Fer n	Mar σ0	Mar K	Mar n
1.25	301	496	0.25	828	799	0.26
1.5	312	506	0.25	831	800	0.26
1.75	322	515	0.25	833	801	0.26
2	330	523	0.25	836	802	0.26
2.25	338	529	0.25	839	802	0.26
DS	0.201	0.112	0.000	0.023	0.007	0.000

**DS represents dimensionless sensitivity*

Table 4.12 Effect of %Mn on Chemical Composition

%Mn	%Mar	%Fer	%C_α	%C_γ	%Mn_α	%Mn_γ	%Si_α	%Si_γ
1.25	22	78	0.009	0.42	0.87	2.55	0.3	0.22
1.5	25	75	0.0078	0.38	1.01	2.91	0.3	0.23
1.75	29	71	0.0068	0.33	1.15	3.22	0.3	0.24
2	32	68	0.006	0.3	1.27	3.5	0.3	0.24
2.25	37	63	0.0053	0.26	1.38	3.74	0.3	0.25
DS	0.9	-0.4	-1.0	-0.8	0.8	0.6	0.0	0.2

Table 4.13 Effect of %Mn on Phase Transformation Lines

%Mn	A1(°C)	A3(°C)	A3-A1(°C)	Ms(°C)	Mf(°C)	Mf-Ms(°C)
1.5	693	839	146	425	315	110
2	680	822	142	401	291	110
2.5	667	807	140	380	270	110
DS	-0.077	-0.078	0	-0.22	-0.31	0

Table 4.14 Effect of %Mn on Transformation Kinetics

%Mn	Per. (°C)	Per (sec)	Bain. (°C)	Bain. (sec)	Fer. (°C)	Fer. (sec)
1.5	600	20	525	0.3	650	0.4
2	575	30	500	0.45	650	2
2.5	550	40	475	0.6	650	7
DS	0	0.67	-0.1	0.67	-0.077	3.3

**Bain, fer and per represents the formation of bainite, ferrite phases and pearlite phase mixture respectively. Transformation temperatures and times at the phase formation noses are given separately.*

A powerful austenite stabilizer Mn promotes higher austenite hardenability values. Since Mn increases the obtained austenite hence the martensite after quenching (Table 4.12) increases the strength of the steel. Furthermore, as shown in Table 4.11, Mn has a solid solution strengthening effect that further increases the strength of both ferrite and martensite.

Significant increase in volume fraction of austenite at the same temperature of annealing caused by increasing manganese content is induced by gradual lowering of the A1 temperature as shown in (Table 4.13). This is opposite to the effects of Si and Al additions that raise A1 (Table 4.17 and Table 4.19).

Manganese partitioning coefficient increases with the increase in temperature. As the IAT increases, the solubility of manganese in ferrite and austenite decreases Table 4.2. Similar behavior can be seen with the addition of silicon content.

4.1.1.1.5 Effect of %Si and %Al

Table 4.15 Effect of %Si on Mechanical Output Parameters

%Si	Fer σ0	Fer K	Fer n	Mar σ0	Mar K	Mar n
0.15	302	498	0.25	845	805	0.26
0.2	315	501	0.25	839	803	0.26
0.25	324	503	0.25	834	801	0.26
0.3	331	508	0.25	828	800	0.26
0.35	340	510	0.25	823	798	0.26
DS	0.142	0.031	0.000	-0.033	-0.011	0.000

**DS represents dimensionless sensitivity*

Table 4.16 Effect of %Si on Chemical Composition

%Si	**%Mar**	**%Fer**	**%C$_\alpha$**	**%C$_\gamma$**	**%Mn$_\alpha$**	**%Mn$_\gamma$**	**%Si$_\alpha$**	**%Si$_\gamma$**
0.15	26	74	0.0077	0.36	1	2.89	0.16	0.12
0.2	26	74	0.0077	0.37	1.01	2.9	0.21	0.16
0.25	25	75	0.0078	0.37	1.01	2.9	0.27	0.2
0.3	25	75	0.0079	0.37	1.02	2.91	0.32	0.24
0.35	25	75	0.008	0.38	1.02	2.92	0.37	0.28
DS	-0.06	0.02	0.05	0.054	0.024	0.012	0.98	1

Table 4.17 Effect of %Si on Phase Transformation Lines

%Si	**A1(°C)**	**A3(°C)**	**A3-A1(°C)**	**Ms(°C)**	**Mf(°C)**	**Mf-Ms(°C)**
0.5	695	845	150	419	309	110
1.5	715	892	177	404	294	110
2.5	737	962	225	390	280	110
DS	0.044	0.098	0.318	-0.054	0.107	0

Aluminum and Silicon prevent the formation of γ-iron, which causes the γ-domain in the iron carbon diagram to shrink into a smaller region. This is due to the corresponding elements support BCC crystallographic structure, hence suppressing FCC-iron austenite and promoting BCC-iron ferrite. Because of this silicon and especially aluminum broadens the IA zone by significantly increasing the A3 temperature as shown in Table 4.17 and Table 4.19 and increases the slope of the γ / (α+γ) solvus which lowers the rate of austenite volume fraction variation with temperature.

Since Al significantly raises the A3 temperature, the annealing of steels with increased Al content at given IAT is accompanied by progressively decreasing volume fraction of the formed austenite and hence of martensite after quenching (Table 4.18).

Therefore, the volume fraction of the generated austenite gradually decreases during the annealing of steels with higher Al and Si concentration at a fixed IAT as shown in Table 4.16 and Table 4.18.

Also, increase in silicon content increase the strength of the ferrite and the DP steel due to solid solution strengthening effect as can be seen in Table 4.15. Reason for providing a better balance of tensile strength and total elongation with the addition of silicon is due to the lowering of the martensite start temperature (Table 4.17), the promotion of new ferrite formation, and the contribution of the refined ferrite grains to the deformation mechanism with finer martensite islands. [31]

Improved work hardening rate of silicon-alloyed ferrite throughout the entire strain range is responsible for the retention of excellent ductility in silicon bearing DP steel. Positive effect of strain hardening coefficient K can be seen in Table 4.17.

Table 4.18 Effect of %Al on Mechanical Parameters and Chemical Composition

%Al	**Fer σ0**	**Fer K**	**Fer n**	**%Mar**	**%Fer**	**%C$_\gamma$**	**%Mn$_\alpha$**	**%Mn$_\gamma$**
1	255	464	0.276	37	63	0.25	1.12	2.27
1.5	280	491	0.279	27	73	0.34	1.21	2.49
2	303	515	0.281	20	80	0.43	1.27	2.64
DS	0.129	0.078	0.011	-0.94	0.35	0.79	0.19	0.22

Table 4.19 Effect of %Al on Phase Transformation Lines and %Si

%Al	%Si$_\alpha$	%Si$_\gamma$	A1(°C)	A3(°C)	A3-A1(°C)	Ms(°C)	Mf(°C)	Mf-Ms(°C)
1	0.31	0.29	701	906	205	442	334	108
1.5	0.3	0.29	711	986.5	275.5	469	361	108
2	0.29	0.29	720	1097	377	487	378	109
DS	-0.1	0	0.04	0.29	0.94	0.14	0.18	0.014

Table 4.20 Effect of %Al on Transformation Kinetics

%Al	Per. (°C)	Per (sec)	Bain. (°C)	Bain. (sec)	Fer. (°C)	Fer. (sec)
0.5	600	11	520	0.3	690	0.17
1	600	10	520	0.3	720	0.06
1.5	600	8	520	0.3	800	0.02
DS	0	-0.15	0	0	0.076	-1.25

**Bain, fer and per represents the formation of bainite, ferrite phases and pearlite phase mixture respectively. Transformation temperatures and times at the phase formation noses are given separately.*

4.1.1.1.6 Effect of %Molybdenum

Table 4.21 Effect of %Mo on Mechanical Parameters and Chemical Composition

%Mo	Fer σ0	Fer K	Fer n	%Mar	%Fer	$\%C_\gamma$	$\%Mn_\alpha$	$\%Mn_\gamma$
1	266	478	0.277	90	10	0.11	0.84	1.63
2	288	501	0.28	71	27	0.12	0.93	1.81
3	297	510	0.28	54	44	0.09	1.05	2.01
DS	0.1076	0.064	0.014	-0.51	1.26	NV	0.23	0.21

Table 4.22 Effect of %Mo on Phase Transformation Lines and %Si

%Mo	$\%Si_\alpha$	$\%Si_\gamma$	A1(°C)	A3(°C)	A3-A1(°C)	Ms(°C)	Mf(°C)	Mf-Ms(°C)
1	0.36	0.29	699	859	160	405	295	110
2	0.34	0.28	705	884	179	395	280	115
3	0.33	0.27	711	914	203	390	260	130
DS	-0.09	-0.07	0.02	0.06	0.24	-0.04	-0.13	0.17

Table 4.23 Effect of %Mo on Transformation Kinetics

%Mo	Per. (°C)	Per (sec)	Bain. (°C)	Bain. (sec)	Fer. (°C)	Fer. (sec)
1	590	300	510	2.1	700	400
2	585	900	500	5	725	300
3	580	1700	490	10	750	280
DS	-0.017	1.56	-0.04	1.58	0.069	-0.4

**Bain, fer and per represents the formation of bainite, ferrite phases and pearlite phase mixture respectively. Transformation temperatures and times at the phase formation noses are given separately.*

Molybdenum shows similar effects with chromium when it is added to steel. By decreasing the MS temperature Mo promotes the higher hardenability of austenite and martensitic transformation on steel. By delaying the pearlite and bainite formation and decreases the Bainite start temperature as can be seen from Table 4.23 it avoids the formation of bainite at the final microstructure of DP steels.

4.1.1.1.7 Effect of %Nb and %Ti

Table 4.24 Effect of %Nb on Mechanical Parameters and Chemical Composition

%Nb	Fer σ0	Fer K	Fer n	%Mar	%Fer	%C_γ	%Mn_α	%Mn_γ
0.5	246	454	0.275	47	52	0.07	1.05	2.12
0.75	253	463	0.276	25	74	0.03	1.25	2.47
1	267	479	0.277	7	91	<0.01	1.47	2.85
DS	0.031	0.02	0.0027	-2.4	0.79	-3.5	0.504	0.443

Table 4.25 Effect of %Nb on Phase Transformation Lines and %Si

%Nb	%Si_α	%Si_γ	A1(°C)	A3(°C)	A3-A1(°C)	Ms(°C)	Mf(°C)
0.5	0.33	0.27	680	856	176	445	340
0.75	0.31	0.27	670	865	195	455	350
1	0.3	0.27	526	875	349	525	425
DS	-0.15	0	-0.345	0.032	1.331	0.26	0.36

Table 4.26 Effect of %Nb on Transformation Kinetics

%Nb	Per. (°C)	Per (sec)	Bain. (°C)	Bain. (sec)	Fer. (°C)	Fer. (sec)
0.25	600	20	520	0.21	640	0.3
0.5	610	30	520	0.2	640	0.2
0.75	No per	No per	520	0.18	640	0.15
1	No per	No per	520	0.15	640	0.1
1.25	No per	No per	520	0.12	640	0.08
DS	NV	NV	0	-0.096	0	-1.08

**Bain, fer and per represents the formation of bainite, ferrite phases and pearlite phase mixture respectively. Transformation temperatures and times at the phase formation noses are given separately. ** NV represents non valid sensitivity analysis result, No per means no pearlite formed at that particular temperature and time*

When carbide formers elements Titanium and Niobium added to the steel, similar kind of effects can be observed with the addition of ferrite stabilizing effect of Titanium. Which are used to regulate the grain size in hot rolled steels, can be utilized to both boost strength and maintain high levels of ductility. Ferrite strength can be altered by the grain size, precipitation hardening, and solid solution hardening. As it can be seen from the Table 4.24 and Table 4.27 Ti addition increases the ferrite strength due to solid solution strengthening effect since some amount of Nb will remain inside the solution after heat treatment.

Also, dramatic increase in obtained %Ferrite can be observed with the addition of both %Ti (Table 4.24) and %Nb (Table 4.27) due to strong effect on contracting or closing the γ-field. Promoting the ferrite formation by Titanium can be seen at Table 4.29.

Table 4.27 Effect of %Ti on Mechanical Parameters and Chemical Composition

%Ti	**Fer $\sigma0$**	**Fer K**	**Fer n**	**%Mar**	**%Fer**	**%C_{γ}**	**%Mn_{α}**	**%Mn_{γ}**
0.3	246	456	0.275	39.8	60	0.060	1.110	2.220
0.45	261	473	0.276	15.5	84	>0.01	1.370	2.670
0.6	273	483.	0.278	5.5	94	>0.01	1.480	2.880
DS	0.023	0.013	0.002	-3.31	0.61	NV	0.404	0.371

**DS represents dimensionless sensitivity*

Table 4.28 Effect of %Ti on Phase Transformation Lines and %Si

%Ti	**%Si_{α}**	**%Si_{γ}**	**A1(^{o}C)**	**A3(^{o}C)**	**A3-A1(^{o}C)**	**Ms(^{o}C)**	**Mf(^{o}C)**
0.3	0.320	0.27	678	861	183	450	340
0.45	0.310	0.27	670	876	206	460	350
0.6	0.300	0.27	603	895	292	465	355
DS	-0.097	0.000	-0.17	0.058	0.794	0.049	0.064

Table 4.29 Effect of %Ti on Transformation Kinetics

%Ti	**Per. (^{o}C)**	**Per (sec)**	**Bain. (^{o}C)**	**Bain. (sec)**	**Fer. (^{o}C)**	**Fer. (sec)**
0.15	600	20	520	0.21	650	0.28
0.3	610	35	520	0.19	650	0.2
0.45	No Per	No Per	520	0.16	650	0.1
DS	NV	NV	0	-0.268	0	-0.9

**Bain, fer and per represents the formation of bainite, ferrite phases and pearlite phase mixture respectively. Transformation temperatures and times at the phase formation noses are given separately. ** NV represents non valid sensitivity analysis result, No per means no pearlite formed at that particular temperature and time*

4.1.1.1.8 Effect of Grain Size

Table 4.30 Effect of Grain Size on Ferrite Mechanical Parameters

INPUT	**OUTPUTS**		
Grain size (um)	**Fer σ0**	**Fer K**	**Fer n**
5	406	585	0.25
10	326	519	0.25
15	291	486	0.24
20	271	465	0.24
25	256	451	0.24
30	246	443	0.24
DS	-0.29	-0.16	0

5 um to 30 um grain sizes are used at IAT = 740 ^{o}C and 30% martensite fraction.

As the grain size decreases it is seen that the material strength increases since grains are barriers to dislocations and restricts the dislocation movements. From Table 4.30, dramatic increase at strength of ferrite can be seen when the grain size decreases to 5 um from 30 um.

4.1.1.2 Thermodynamic Sensitivity Analysis Results

Sensitivity analysis Table-4.31 is created to include all inputs and outputs based on the DS (dimensionless sensitivity) values calculated at the previous section.

Table 4.31 Thermodynamic Sensitivity Analysis Results

	IAT (°C)	**%C**	**%Cr**	**%Mn**	**%Si**	**%Mo**	**%Nb**	**%Ti**	**%Ni**	**%Al**	**Max_abs**
Fer σ0	-1.32	-0.07	0.04	0.20	0.14	0.11	0.03	0.02	NM	0.09	1.32
Fer K	-0.79	-0.04	0.02	0.11	0.03	0.06	0.02	0.01	NM	0.05	0.79
Fer n	0.00	0.00	0.00	0.00	0.00	0.01	0.00	0.00	NM	0.01	0.01
Mar σ0	-8.29	0.51	NV	0.00	-0.03	NM	NM	NM	NM	NM	8.29
Mar K	NV	0.18	NV	0.01	-0.01	NM	NM	NM	NM	NM	0.18
%C$_{\alpha}$	-7.23	0.30	-0.07	-0.95	0.05	NM	NM	NM	NM	NM	7.23
%Cγ	-13.5	0.24	-0.04	-0.85	0.054	**NV**	-3.50	NM	-0.91	0.53	13.5
%Cr$_{\alpha}$	-0.74	NM	NM	NM	NM	NM	NM	NM	NM	NM	0.74
%Crγ	-3.36	NM	NM	NM	NM	NM	NM	NM	NM	NM	3.36
%Mn$_{\alpha}$	-1.47	-0.29	-0.04	0.78	0.03	0.23	0.50	0.40	-0.53	0.12	1.47
%Mnγ	-6.17	-0.24	-0.02	0.65	0.01	0.21	0.44	0.37	-0.47	0.15	6.17
%Si$_{\alpha}$	1.11	0.07	0.00	0.00	0.98	-0.09	-0.14	-0.10	0.00	-0.07	1.11
%Siγ	-1.11	0.07	0.00	0.20	1.00	-0.07	0.00	0.00	0.09	0.00	1.11
%Ni$_{\alpha}$	-2.39	NM	NM	NM	NM	NM	NM	NM	0.62	NM	2.39
%Niγ	-3.94	NM	NM	NM	NM	NM	NM	NM	0.63	NM	3.94
% Mar	8.72	0.83	0.06	0.89	-0.06	-0.50	-2.40	-3.31	0.81	-0.95	8.72
% Fer	-5.81	-0.28	-0.02	-0.37	0.02	1.26	0.79	0.60	-0.75	0.35	5.81
A1 (°C)	NM	0.02	0.04	-0.08	0.04	0.02	-0.35	-0.16	-0.08	0.02	0.35
A3 (°C)	NM	NV	-0.03	-0.08	0.10	0.06	0.03	0.06	-0.08	0.19	0.19

Table 4.31(Cont'd)

A3-A1 (°C)	NM	NV	-0.59	0.00	0.32	0.24	1.33	0.79	-0.10	0.62	1.33
Ms (°C)	NM	-1.28	-0.09	-0.22	-0.05	-0.04	0.26	0.05	-0.16	0.10	1.28
Mf (°C)	NM	-5.98	-0.01	-0.31	0.11	-0.13	0.36	0.06	-0.25	0.12	5.98
Mf-Ms (°C)	NM	0.24	0.00	0.00	0.00	0.17	0.00	0.00	NV	0.01	0.24
Fer. (°C)	NM	0	0	-0.08	0.08	0.07	0	0	-0.05	0.08	0.08
Fer. (sec)	NM	12.5	2.38	3.3	0	-0.4	-1.8	-0.9	1.55	-1.25	12.5
Per. (°C)	NM	0	0.065	0	0	-0.02	NV	NV	-0.08	0	0.08
Per. (sec)	NM	-0.1	0.67	0.67	0.45	1.56	NV	NV	1.32	-0.15	1.56
Bain. (°C)	NM	-0.05	-0.08	-0.1	-0.06	-0.04	0	0	-0.07	0	0.1
Bain. (sec)	NM	0.98	2	0.67	0.6	1.58	-0.1	-0.27	1.39	0	2

**NM represents the not measured values and NV represents the not valid values on the table.*

***Bain, Fer and Per represents the formation of bainite, ferrite phases and pearlite phase mixture respectively. Transformation temperatures and times at the phase formation noses are given separately.*

4.1.1.2.1 IAT - %Carbon Relationship

Table 4.31 shows that as the IAT increases obtained austenite increases correspondingly until equilibrium and as the %C in alloy increases obtained austenite increases at the same IAT.

However, as shown in Figure 2.9B, the quantitative impact of a certain alloying element on the hardenability of austenite changes from 700 °C to 800 °C, dropping from 0.6 to 0.1 Cγ for 0.05%C DP Steel.

Figure 4.7 shows a modeled DP steel with a similar trend but a slightly different chemical composition and below Table 4.32 shows that IAT strongly affect the %C in both austenite and ferrite and final phase fractions of the DP steel.

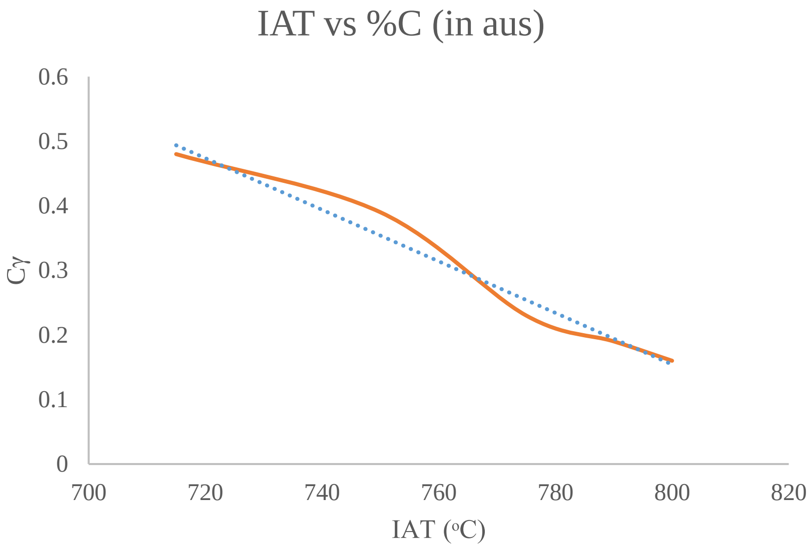

Figure 4.7. IAT vs %C relationship in DP Steels

Table 4.32 IAT vs dissolved %C in phases and Formed %Mar and %Fer

	IAT (ºC)
%C$_\alpha$	-7.23
%Cγ	-13.48
% Mar	8.72
% Fer	-5.83

4.1.1.2.2 %Manganese %Carbon Relationship

Increase in %Mn decreases the %C both in ferrite and austenite for the same IAT with a strong coefficient (Table 4.33).

Similar behavior can be seen from the Figure 2.9B.

Table 4.33 %Mn vs Mechanical Properties of Ferrite and dissolved %C in phases

	%Mn
Fer σ0	0.20
Fer K	0.11
Fer n	0
%C_α	-0.95
%Cγ	-0.85

4.1.1.2.3 Relationship of %Silicon and %Aluminum with %Carbon

As can be seen from Table 4.34, the thermodynamic model of DP steel predicts that as %Al and %Si increases, so does the percentage of carbon in ferrite and austenite for the same IAT. Also, more pronounced effect of %Al can be seen.

Similar trend is observed at the previous working in area which is shown at Figure 2.9B.

Positive effect of %Si and %Al on %ferrite is known since they are strong ferrite stabilizers as shown in Figure 2.12.

Likewise, the stronger effect of %Al on the austenite ratio in the same IAT compared to %Si was calculated in the model as seen in the table below, and it is consistent with Figure 2.9B.

Table 4.34 %Si and %Al, dissolved %C in phases and Formed %Mar and %Fer

	%Si	**%Al**
$\%C_\alpha$	0.05	NV
$\%C\gamma$	0.05	0.53
% Mar	-0.06	-0.95
% Fer	0.02	0.35

**NV represents the not valid property*

4.1.1.2.4 Chemical Composition Effect on A1 Temperature

Table 4.35 Chemical Composition Effect on A1 Temperature

	IAT (^oC)	**%Cr**	**%Mn**	**%Si**	**%Mo**	**%Ti**	**%Ni**
A1(^oC)	NM	0.04	-0.08	0.04	0.02	-0.16	-0.08
$\%C_\gamma$	-13.48	-0.04	-0.85	0.05	NV	NM	-0.91

**NM represents the not measured values and NV represents the not valid values on the table.*

Austenite stabilizers lower the eutectoid A1 temperature, thereby widening the temperature range over which austenite is stable. Similarly, the ferrite formers raise the eutectoid temperature, thereby restricting the γ –phase field.

From the Figure 2.13, A1 temperature increasing elements are in the order of %Ti>%Mo>%Si>%Cr and A1 temperature decreasing elements are in the order of Ni>Mn.

Almost same order is obtained except %Mo from the thermodynamical model as following in Table 4.35:

A1 temperature increasing elements in the order of %Ti>%Si>%Cr>%Mo (+).

A1 temperature decreasing elements in the order of %Ni>%Mn.

4.1.1.2.5 Chemical Composition Effect on TTT Diagrams

It is known that alloying elements that dissolve only in ferrite and cementite without the formation of special carbides like Ni, Si, Mn and Al exert just a quantitative effect on the transformation processes and delay the transformation as shown in Figure 2.14. Similar outcome is obtained from the model except %Al as shown in below Table 4.36.

Table 4.36 Chemical Composition Effect on Transformation Time

	%Mn	**%Si**	**%Ni**	**%Al**
Fer (sec)	3.3	0	1.55	-1.25
Per (sec)	0.67	0.45	1.32	-0.15
Bain (sec)	0.67	0.6	1.39	0

***Bain, Fer and Per represents the formation of bainite, ferrite phases and pearlite phase mixture respectively. Transformation times at the phase formation noses are given separately.*

4.1.1.2.6 Effect on Ferrite Hardness

Effect of hardness of elements which is proportional with the strength can be seen in Figure 2.12. According to figure Cr is the least effective element among others in ferrite hardness. For this reason, Cr is a most convenient alloying element in steel that is to be processed by cold working in which good hardenability is required. Since it gives the smallest hardness increase. According to Figure 2.12, effect of ferrite hardness in the order of: %Si>%Mn>%Mo>%Cr

A similar result was obtained from the model at Table 4.37, except that the places of Si and Mn were changed with close coefficients. According to model effect of ferrite hardness in the order of %Mn>%Si>%Mo>%Cr.

It is shown that Si and Mn, the most frequently occurring alloying elements, have a relatively potent effect on the hardness of ferrite.

Table 4.37 Effect of Chemical Composition on Fer. Mechanical Properties

	IAT (°C)	%C	%Cr	%Mn	%Si	%Mo	%Nb	%Ti	%Ni	%Al
Fer σ0	-1.32	-0.07	0.04	0.20	0.14	0.11	0.03	0.023	NM	0.09
Fer K	-0.79	-0.04	0.02	0.11	0.03	0.06	0.02	0.01	NM	0.05
Fer n	0.00	0.00	0.00	0.00	0.00	0.01	0.00	0.00	NM	0.01

4.1.1.2.7 Chemical Composition Effect on Martensite Start Temperature

Most alloying elements which enter solid solution, lower the martensite start temperature (MS), with the exception of Co and Al according to Figure 2.8b. Same results are obtained from the model at Table 4.38.

However, the interstitial solutes carbon and nitrogen have a much prominent effect than the metallic solutes. Empirical equation (Eqn.5) shows the dramatic effect of %Carbon to determine MS temperature. Similar observation can be made from the model results at Table 4.38 with approximate coefficients and slightly changing order.

Model solution:

Effect on martensite start %C >> %Mn > %Ni > %Al > %Cr > %Si

Empirical model Eqn. 5,

Effect on martensite start %C >> %Mn > %Al > %Ni, %Cr > %Si

Table 4.38 Chemical Composition Effect on Martensite Start Temperature

	%C	**%Cr**	**%Mn**	**%Si**	**%Mo**	**%Ni**	**%Al**	**Max(abs)**
Ms (°C)	-1.28	-0.09	-0.22	-0.05	-0.04	-0.16	0.1	1.28
Mf (°C)	-5.98	-0.01	-0.31	0.11	-0.13	-0.25	0.12	5.98
Mf-Ms (°C)	0.24	0	0	0	0.17	NV	0.01	0.17

**NV represents non valid analysis value*

Some of the critical mechanical properties of DP steels are governed by MS since it affects the number of mobile dislocations and the level of residual stresses generated in local γ-α transformation. Because of this, the martensite structure, cooling behavior and the amount of retained austenite in the final microstructure are all within the control of MS Temperature and according to analysis results %C is the important part of it.

By looking at the outcomes of modifying several parameters at once, sensitivity analysis can produce more outputs and be improved. But since alloy design is outside the scope of the thesis, the examples are restricted to those presented above.

<u>According to thermodynamic sensitivity analysis below outcomes are obtained:</u>

- IAT is the most critical parameter by far, IAT should be chosen carefully and fixed.
- ▪ In terms of the alloy's contribution to material strength, %C and %Mn should be precisely measured experimentally for a more reliable model.
- ▪ %C dramatically affect the martensite strength and MS temperature.
- ▪ %Mn and %Si dramatically affect the ferrite strength.
- ▪ %Mn and %C strongly affect the obtained %Austenite at fixed IAT.
- ▪ The final strength of DP steel is greatly influenced by the strong effect of grain size on ferrite strength.

- %Al and %Si has a significant effect on obtained %Martensite after quenching.

4.1.2 Thermodynamic Modeling of BORCELIK and SSAB DP Steels

After sensitivity analysis, thermodynamic analysis models are created for DP600 and DP800 samples. In order to perform thermodynamic analysis, chemical analysis data from the manufacturer, experimentally measured ferrite grain size and ferrite martensite phase ratios are used as input data. In that case ferrite grain sizes for all specimens (Table 4.40) and ferrite, martensite fractions (Table 4.39) are calculated with the methods mentioned in the previous chapter (experimental methods). For the austenite grain sizes, the austenite grain sizes suggested by the software at that IAT is used.

Table 4.39 %Ferrite in DP Steel Specimens

EXPERIMENT	**%Ferrite**
SSAB-DP600	82
SSAB-DP800	65
BOR-DP600	79
BOR-DP800	63

Table 4.40 Grain Sizes of Ferrite in DP Steel Specimens

	0°	**90°**	**Avr.**
DP600-SSAB	11.1	8.4	10
DP800-SSAB	5.14	4.87	5.01
DP600-BOR	3.98	4.16	4.07
DP800-BOR	3.76	3	3.38

In thermodynamic modeling, main focus is finding the most critical parameter IAT and fix the parameter for the following models. Equilibrium IAT's are calculated from the THERMOCALC Software to obtain necessary amount of phases shown in Table 4.39. Calculated equilibrium IAT's can be found at Table 4.41.

Tablo 4.41 Temperatures Required to Obtain the Experimental Amount of Ferrite at Thermodynamical Equilibrium

	% Ferrite Fraction (EXP)	**Equilibrium IAT (^{o}C)**
SSAB-DP600	82	710
SSAB-DP800	65	750
BOR-DP600	79	710
BOR-DP800	62	705

Kinetic mobility database of the software is used to determine the most suitable IAT's for each specimen since it is unknown how long it will take for the phase quantities to reach thermodynamic equilibrium.

4.1.2.1 Modelling Strategy for Finding IAT’s

A thermodynamical-kinetic model is developed using two different specimen, SSAB-DP600 and SSAB-DP800. Since austenite grain sizes (25 um, 50 um) at that temperature and time are unknown, the model is evaluated for several times (900s, 1800s, 3600s, and 7200s) and varied grain sizes.

According to model, specimens are austenitized at 890 °C for 900 s. Then cooled to IAT with 1 °C/s, holding at given IAT for 900 seconds. Finally, it is quenched with 225 °C/s to obtain ferrite martensite DP steel microstructure. Different grain sizes of austenite (25 um, 50 um) are used in the model since the exact grain size of austenite at that specific IAT is not known.

According to thermodynamic model, carbon profiles and fraction of obtained BCC-iron ferrite are calculated as follows in Figure 4.8, Figure 4.9, Figure 4.10, Figure 4.11 for all selected IAT’s.

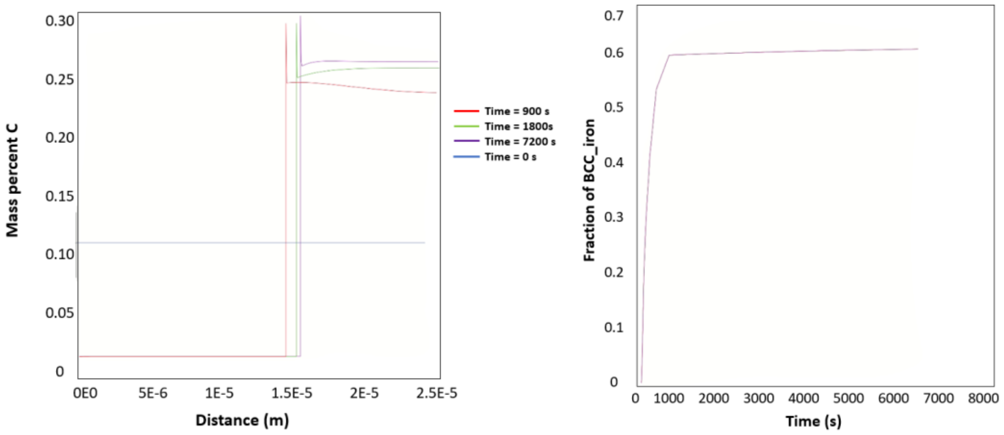

a) b)

Figure 4.8. SSAB-DP600 steel specimen, at IAT 720 °C, 25 um grain size a) carbon profile during inter-critical annealing at 900 s, 1800 s and 7200 s b) Formation fraction of BCC ferrite iron

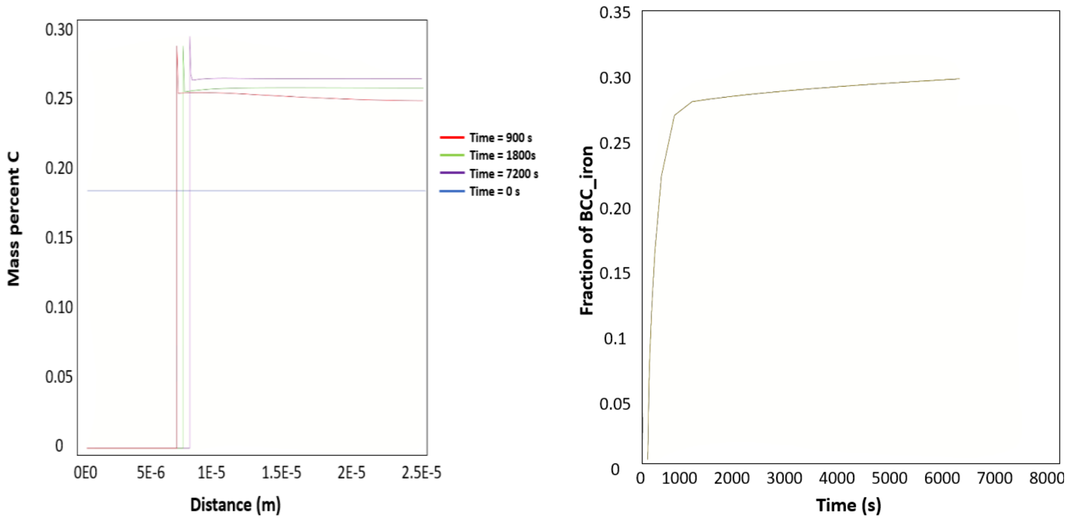

Figure 4.9. SSAB-DP600 steel specimen, at IAT 755 °C, 25 um grain size a) carbon profile during inter-critical annealing 900 s, 1800 s and 7200 s b) Formation fraction of BCC ferrite iron

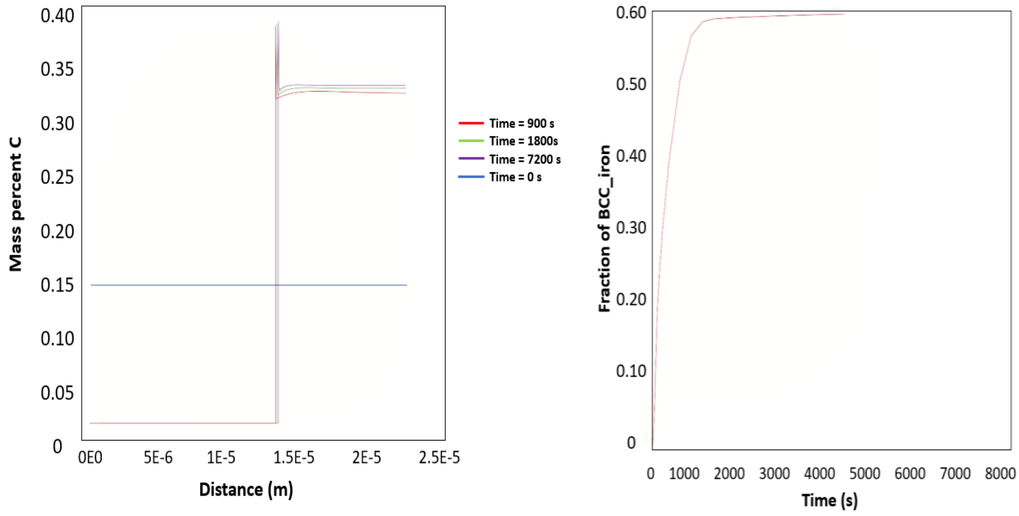

Figure 4.10. SSAB-DP800 steel specimen, at IAT 700 °C, 25 um grain size a) carbon profile during inter-critical annealing b) Formation fraction of BCC ferrite iron

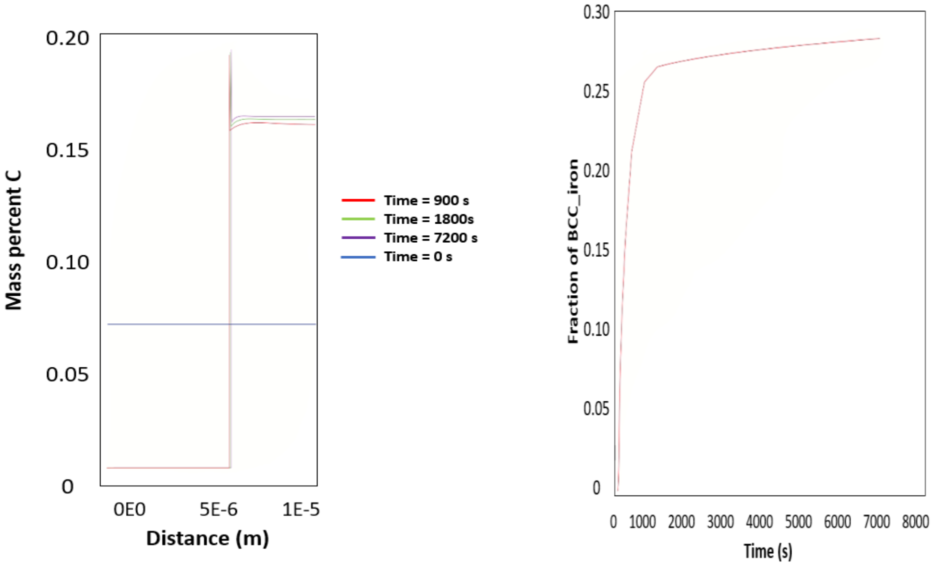

Figure 4.11. SSAB-DP800 steel specimen, at IAT 740 °C, 25 um grain size a) carbon profile during inter-critical annealing b) Formation fraction of BCC ferrite iron

Table 4.42 SSAB-DP600 steel, model results, the amount of ferrite to be obtained after 900 s of IA at different temperatures

	SSAB-DP600			
IAT (°C)	**720**		**755**	
%Fer	60	46	28	12
Aust. Grain Size (um)	25	50	25	50

Table 4.43 SSAB-DP800 steel, model results, the amount of ferrite to be obtained after 900 s of IA at different temperatures

	SSAB-DP800			
IAT (°C)	**700**		**740**	
%Fer	58	38	27	17
Aust. Grain Size (um)	25	50	25	50

It is seen from the Table 4.42, Table 4.43 and above Figure 4.8, Figure 4.9, Figure 4.10, Figure 4.11 that 900 seconds at IA region is not enough for both specimens to reach thermodynamic equilibrium. The reason for using 25 um and 50 um as grain sizes is that the austenite grain size of the steel is thought to be in this range at the temperatures used. By using these grain sizes, a range for the phase fractions that will occur after 900 seconds is calculated.

After modeling is done, experimental validation is set up at the same time to see if the modeled results and experimental validation results are compatible. Same parameters used for both model and experiment, experimental set up can be seen below.

4.1.2.1.1 Step1 - Experimental Set-Up

Two different specimens SSAB-DP600 and SSAB-DP800 is used for the experiment. 2 different IAT is selected for each specimen as shown in Table 4.42 and Table 4.43. Specimens are austenitized at 890 °C for 900 s. Then cooled to IAT with 1 ^{o}C/s, holding at given IAT for 900 seconds. Finally, it is quenched with 225 ^{o}C/s to obtain ferrite martensite DP steel microstructure.

Experimental parameters for obtaining desired microstructure is determined from the TTT, CCT curves created with the JMatPro software shown in Figure 4.12, Figure 4.13, Figure 4.14, Figure 4.15.

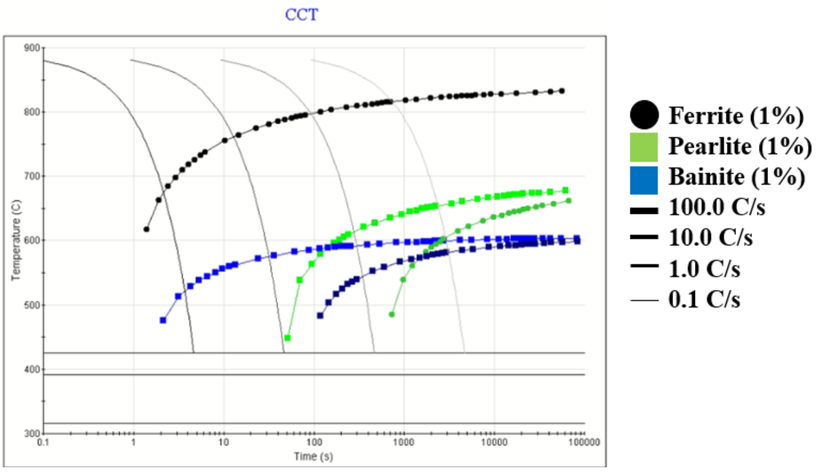

Austenitisation temperature (°C): 890

Figure 4.12. Continuous Cooling Transformation Diagram of SSAB-DP600 steel

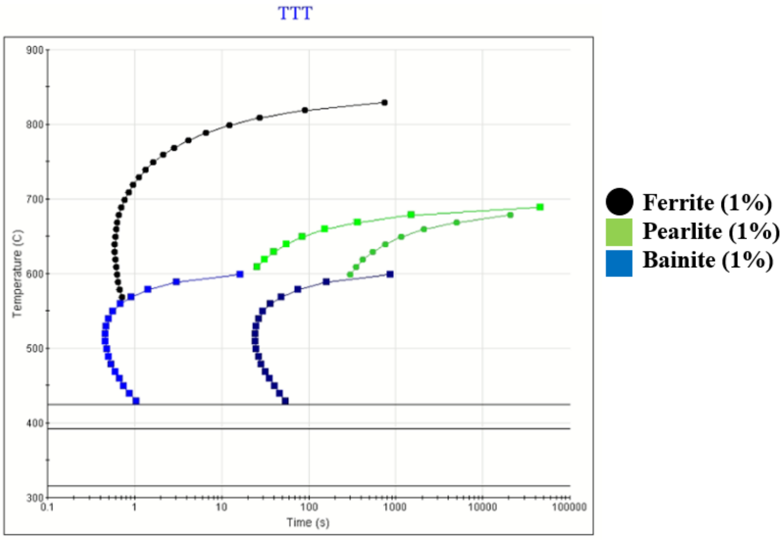

Austenitisation temperature (°C): 890

Figure 4.13. Time Temperature Transformation Diagram of SSAB-DP600 steel

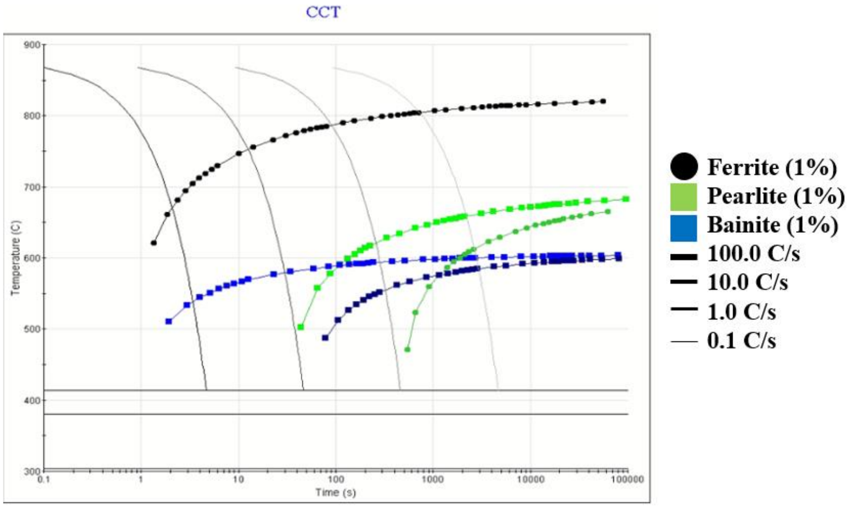

Austenitisation temperature (°C): 890

Figure 4.14. Continuous Cooling Transformation Diagram of SSAB-DP800 steel

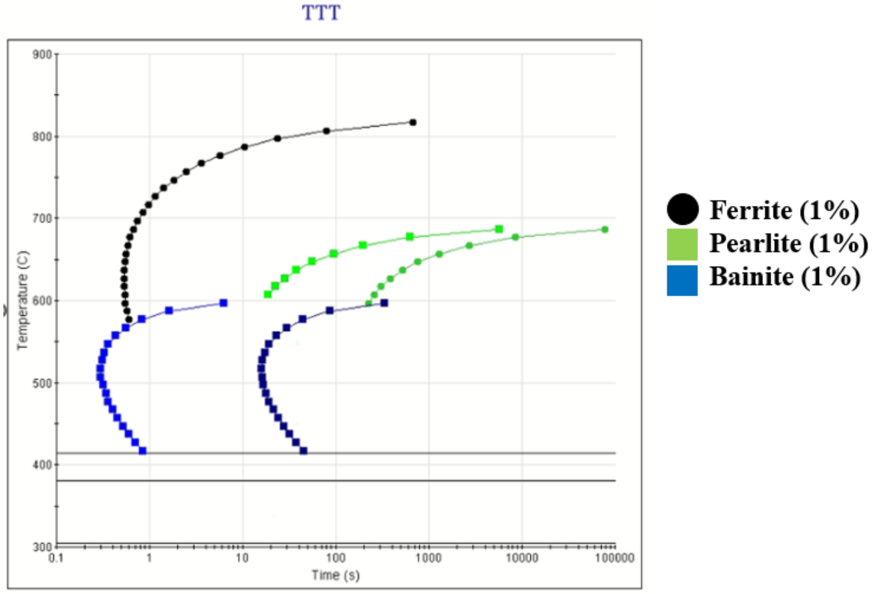

Austenitisation temperature (°C): 890

Figure 4.15. Time Temperature Transformation Diagram of SSAB-DP800 steel

Optical microscope photographs of all specimens after the experiment can be seen in the Figure 4.16, Figure 4.17, Figure 4.18 and Figure 4.19 below.

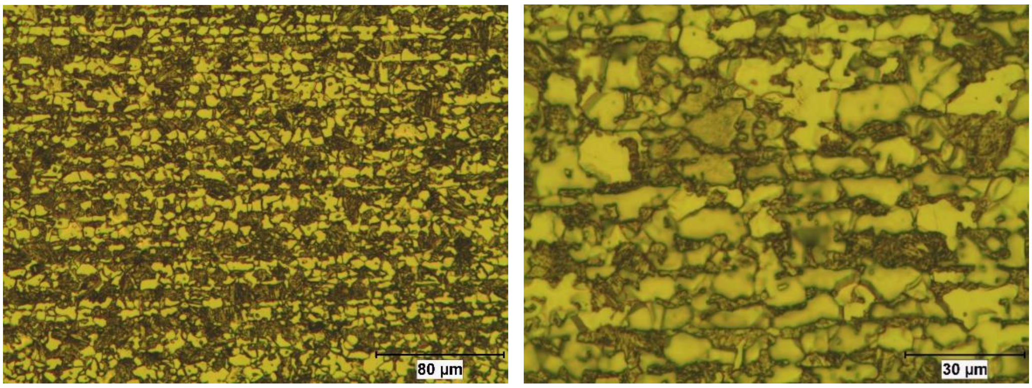

Figure 4.16. Microstructure of inter critically annealed at 700 °C SSAB-DP800 steel sample after experiment a) 200x magnification b) 500x magnification

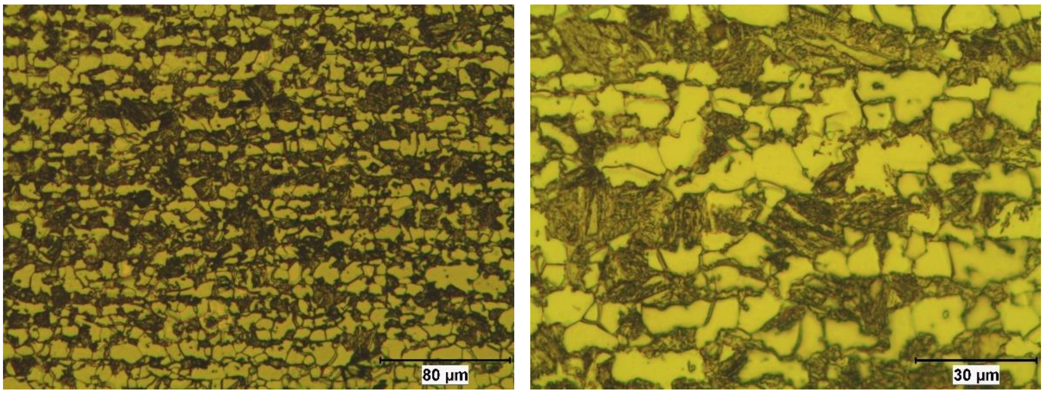

Figure 4.17. Microstructure of inter critically annealed at 740 °C SSAB-DP800 steel sample after experiment a) 200x magnification b) 500x magnification

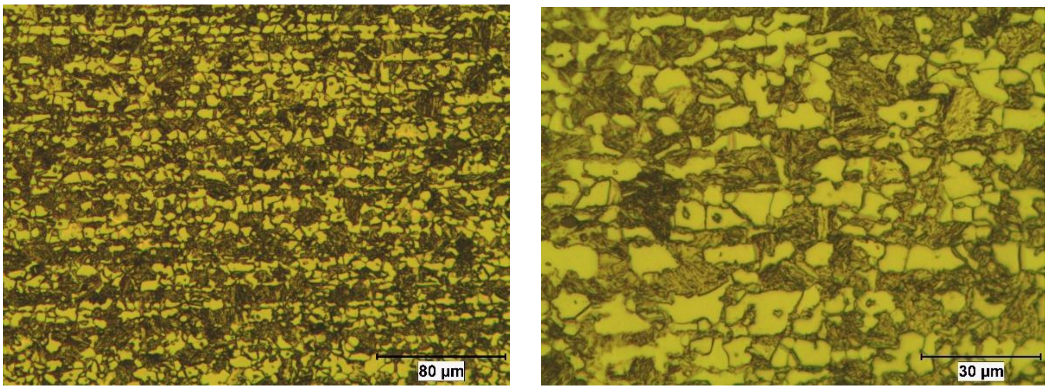

Figure 4.18. Microstructure of inter critically annealed at 720 ^{o}C SSAB-DP600 steel sample after experiment a) 200x magnification b) 500x magnification

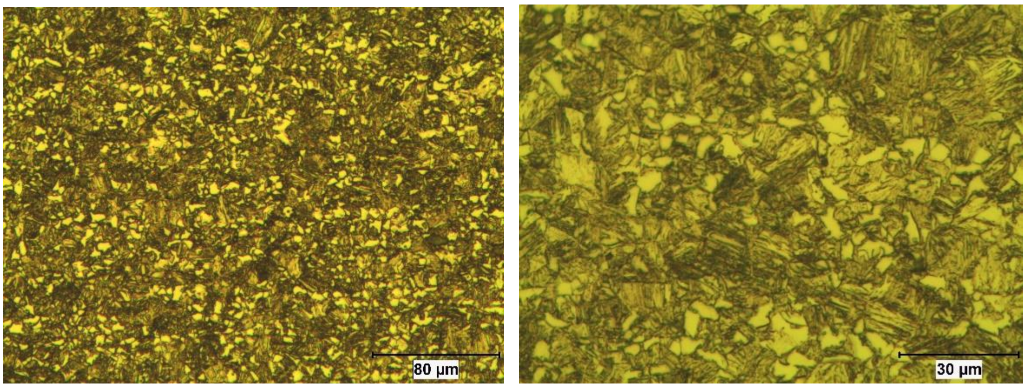

Figure 4.19. Microstructure of inter critically annealed at 755 ^{o}C SSAB-DP600 steel sample after experiment a) 200x magnification b) 500x magnification

After OM photographs are taken, phase fractions are calculated by ImageJ image processing program. Results are available at Table 4.39. At least 7 photographs from same magnification (200x and 500x) are used and results are averaged.

After the experiment, it is evident that the equilibrium ferrite and martensite fractions that are listed in Table 4.41 and the model solution in Table 4.44 are not attained.

Table 4.44 %Ferrite after experiment

	IAT (°C)	**%Fer**
SSAB-DP800	700	43%
	740	27%
SSAB-DP600	720	41%
	755	29%

Results show that 900 s is not enough to reach to equilibrium for DP steel specimens. Also, necessary cooling rates (225 C/s) couldn’t be obtained in experiment and bainite is formed instead of martensite.

But when the experimental and thermodynamical model results are compared it is seen that calculated results are compatible, and the model set up in the THERMOCALC is working properly as shown in Table 4.45.

Table 4.45 Experimentally Measured vs Thermodynamically Modeled %Ferrite

	IAT (°C)	**%Ferrite (Exp)**	**%Ferrite (Modeled)**
SSAB-DP800	700	43% ± 4%	38-58%
	740	27% ± 3%	12-28%
SSAB-DP600	720	41% ± 4%	45-61%
	755	29% ± 3%	17-27%

4.1.2.1.2 Step2 – Model Validation of IAT

New analyses were conducted to determine the IAT that should be used to arrive at the phase fractions in samples from steel suppliers at Table 4.39 after it is determined that the results from the thermodynamic model and experimental data are compatible.

Models are conducted using 2 distinct austenite grain sizes, 25 um and 50 um, following the determination of 3 different IAT for SSAB-DP600 and SSAB-DP800 specimens.

Results are shown in below Table 4.46 and Table-4.47:

Table 4.46 Effect of Time on Ferrite transformation at different IAT's for SSAB-DP600 steel

SSAB-DP600						
IAT (°C)	700		720		755	
%Fer (900s)	75	52	58	40	28	12
%Fer 1800s	76	65	60	50	28	22
%Fer 3600s	76	77	61	60	29	28
%Fer 7200s	79	79	61	60	30	30
Grain Size (um)	25	50	25	50	25	50

Table 4.47 Effect of Time on Ferrite transformation at different IAT's for SSAB-DP800 steel

SSAB-DP800						
IAT (°C)	**700**		**710**		**740**	
%Fer 900s	57	40	52	30	24	16
%Fer 1800s	58	54	52	41	26	22
%Fer 3600s	58	58	53	51	26	26
%Fer 7200s	59	59	54	53	27	27
Grain Size (um)	25	50	25	50	25	50

The following comments can be made based on the results:

1- It can be seen that keeping ferrite at the IAT for more than an hour does not provide much benefit as the holding period at the IA area increases and ferrite approaches the equilibrium state (Table 4.48)

2- Equilibrium composition cannot be reached even for long periods because the reaction rate slows down after a certain period of time.

3- In order to obtain the required phase fractions in all samples, samples should be kept for at least 1-2 hours at low temperatures in the IAT region, slightly above the eutectoid temperature.

4- In order to produce the necessary amount of ferrite and martensite phases, the time and temperature are chosen to be 3600 s at 700 °C for both SSAB-DP600 and SSAB-DP800 samples.

5- After the same procedures were done for BOR-DP600 and BOR-DP800 (Table 4.48). IAT is chosen as 700 °C for all samples.

Table 4.48 Effect of Time on Ferrite transformation at IAT=700 °C for BOR-DP600 and BOR-DP800 steels

IAT	**700 °C**	
Specimens	**BOR-DP800**	**BOR-DP600**
% Fer (900s)	54	59
% Fer (1800s)	56	59
% Fer (3600s)	56	60
% Fer (7200s)	57	61

- Ferrite fractions calculated by the THERMOCALC program are close to the experimental data but relatively less ferrite fractions are calculated in the model for BORCELIK samples. In addition, it is calculated from the model that the required ferrite fractions for the BOR-DP600 sample could not be achieved even at the lowest temperature that could be selected, which should be noted. Therefore, 700 °C, the lowest temperature just above the eutectoid line is selected.
- This may be due to the use of a model solution scheme in THERMOCALC that cannot provide such detailed solutions in nucleation mechanisms, although the growth mechanisms are handled with sophisticated models while calculating in the program.
- Based on the results, it is decided that the IAT temperature for all samples should be 700 °C, which is slightly above the eutectoid line (Table-4.49).

Table 4.49 Final Selected IAT's for Thermodynamical Model

	IAT (°C)
SSAB-DP600	700
SSAB-DP800	700
BOR-DP600	700
BOR-DP800	700

To see the effect of alloying elements on ferrite transformation rate, same model for SSAB-DP600 specimen is used at IAT=720 °C with only C, Si, Mn addition and with C, Si, Mn, Ni and Cr addition.

Table 4.50 Effect of Additional Alloying on Ferrite Transformation

	SSAB-DP600	
IAT(C°)	**720 (C-Si-Mn)**	**720 (C-Si-Mn-Ni-Cr)**
900 s	53%	49%
3600 s	63%	61%
7200 s	64%	61%

If we look at Table 4.50 ferrite transformation slows down a little more when the Ni and Cr is added to the model due to the substitutional solid solution diffusion delaying effect.

4.1.2.2 Calculation of Ferrite and Martensite Flow Curves

After IAT's for all 4 specimens are calculated, all input data needed to initialize the model are obtained to find the ferrite and martensite flow curves of specimens. After all input values are implemented to model in JMatPro software flow curves of both martensite and ferrite phases are calculated.

All model results and least square error minimization best fits are listed in below.

Since the damage parameter is not defined, the strain values for the individual phases ferrite and martensite are reached to higher amounts than the strain values that can be reached experimentally. Here, the information included in the curves is processed and used as a tool to aid in understanding the general flow pattern across the phases. The resulting data trends are implemented in power law, which is one of the most used methods in defining strain hardening behavior, using the least square error minimization method. Consequently, strain hardening coefficient (K) and exponent (n) of both phases are found.

As a result, yield stress values and strain hardening exponent and coefficient values for the individual phases are found which are shown in Figure 4.20, Figure 4.21, Figure 4.22 and Figure 4.23.

Then the whole data obtained from the thermodynamical modeling shown in Table 4.53 are used as input parameters for mechanical modeling stage.

4.1.2.2.1 Ferrite and Martensite Flow Curves of BOR-DP600 specimen

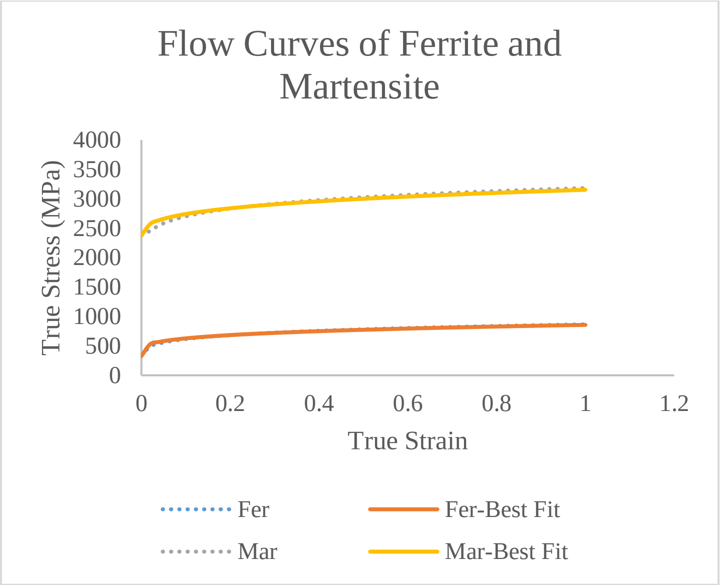

Figure 4.20. Ferrite and Martensite Flow Curves of BOR-DP600 specimen

4.1.2.2.2 Ferrite and Martensite Flow Curves of SSAB-DP600 specimen

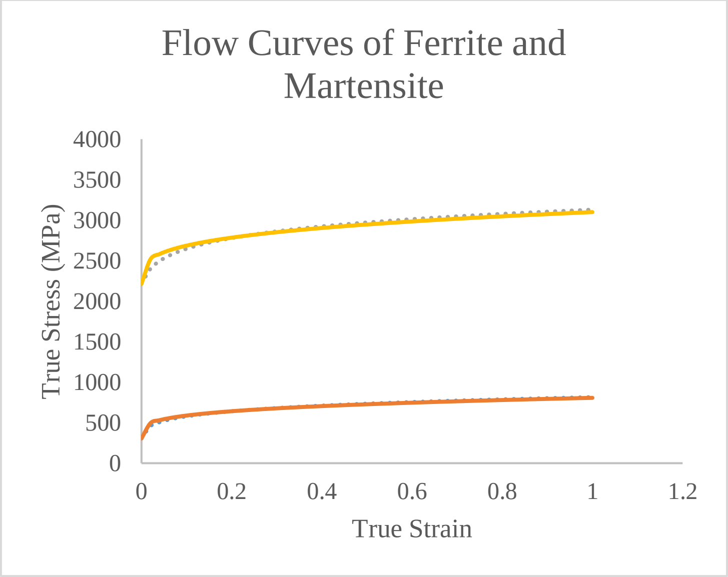

Figure 4.21. Ferrite and Martensite Flow Curves of SSAB-DP600 specimen

4.1.2.2.3 Ferrite and Martensite Flow Curves of BOR-DP800 specimen

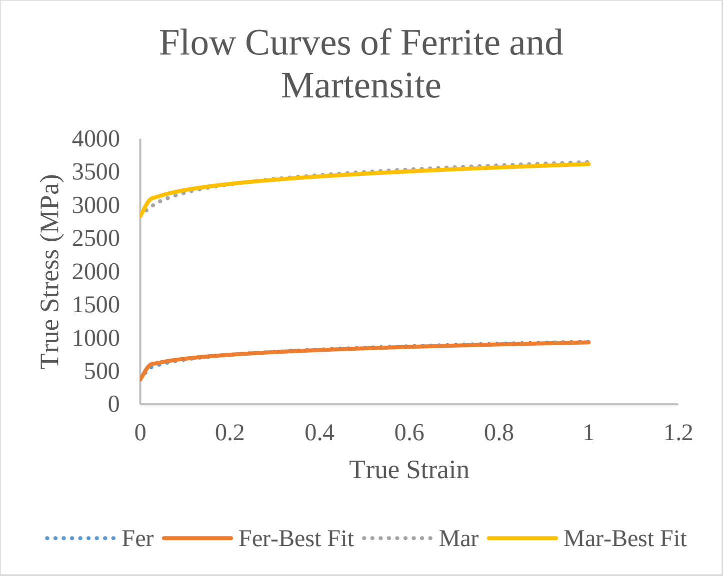

Figure 4.22. Ferrite and Martensite Flow Curves of BOR-DP800 specimen

4.1.2.2.4 Ferrite and Martensite Flow Curves of SSAB-DP800 specimen

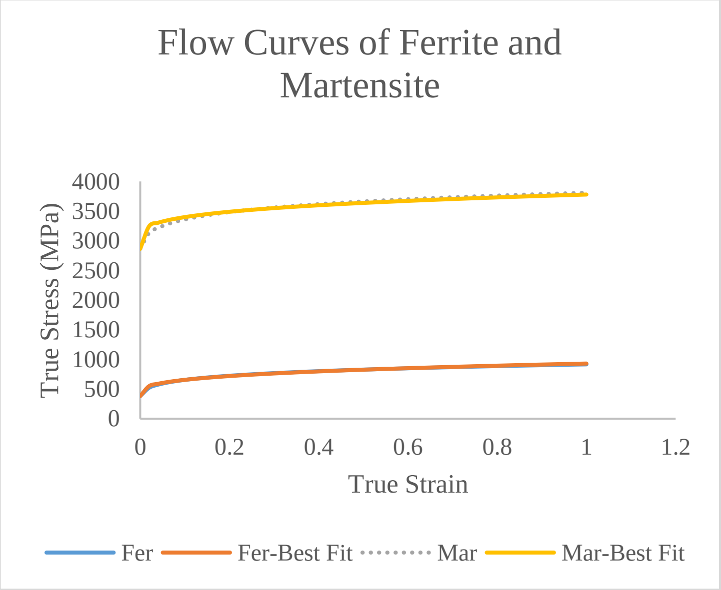

Figure 4.23. Ferrite and Martensite Flow Curves of SSAB-DP800 specimen

4.2 Mechanical Modeling Procedure

Mechanical modeling flowchart is shown in below Figure 4.24.

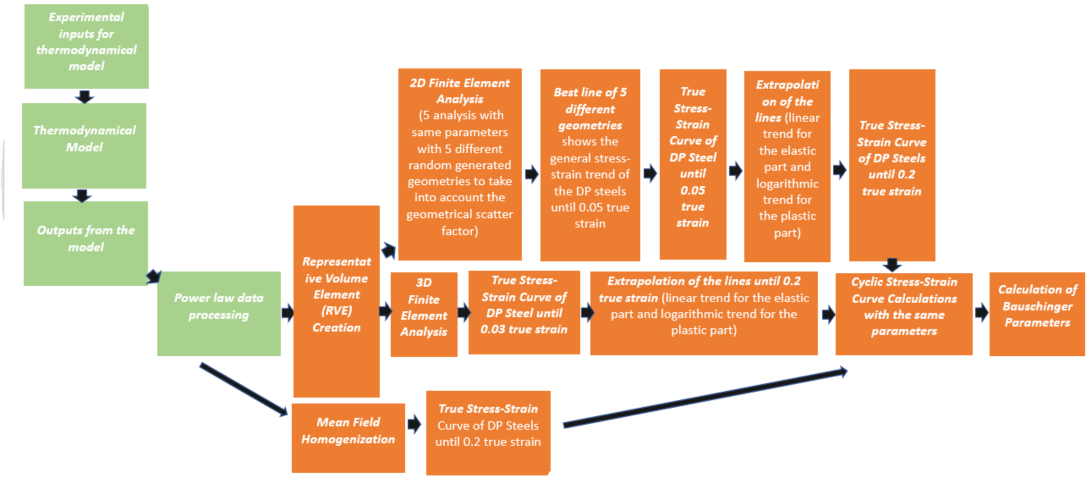

Figure 4.24. Mechanical Modeling Procedure Flowchart-1

Mechanical modeling inputs are found from the thermodynamical models as shown in Table 4.53. It is mentioned that two homogenization methods would be used to calculate the general yield curves of steels.

For the MFH approach, elliptical-shaped martensite islands are randomly positioned on a 2D plane. Utilizing the incremental linearization method, the first order Mori-Tanaka homogenization scheme is applied. With randomly oriented ellipsoid martensite islands, 2D plane strain analysis and 3D analysis are carried out independently for the FEA approach. Ferrite and martensite phases are defined for all models with elastoplastic behavior. Crystal plasticity calculations are not included in the uniaxial tensile behavior calculations since the texture effect in especially hot rolled DP steels is negligible. Also, polycrystalline modeling is not included in the calculations because a different result would not be obtained from the modeling method used in thesis. If a more advanced modeling is desired with polycrystalline modeling, interface energies between ferrite and martensite phases should be calculated and added to the model. This process is outside the scope of this thesis. The aim of this thesis is to create a modeling framework with as simple approaches as possible by reducing the experiments to be done and the created framework is open to development.

Before performing mechanical uniaxial tensile modeling on real DP steel samples, sensitivity analysis is performed to measure the effects of input parameters on output parameters, to optimize the model and to eliminate unnecessary parameters.

Input and output parameters are shown below:

Inputs: Ferrite K, Ferrite yield strength, Martensite%, Martensite yield strength, Aspect ratio for both MFH and FEA method.

Outputs: Ultimate Tensile Strength, Yield Stress (0.2%), DP Steel K, DP Steel n

4.2.1 Uniaxial Tensile Test Sensitivity Analysis Table

Uniaxial tensile test sensitivity analysis results can be found in Table 4.51. Effect of input parameters to output parameters are shown in Table 4.52.

Table 4.51 Dimensionless sensitivity factor of input parameters to output parameters on fictitious DP Steel

	DP Steel UTS	**DP Steel $\sigma0$ (0.2%)**	**DP Steel K**	**DP Steel n**
Fer K (MFH)*	**0.535**	**0.045**	**1**	**0**
Fer $\sigma0$ (MFH)*	**0.473**	**0.687**	**0**	**0**
%Mar (MFH)*	**0.286**	**0.116**	**0.58**	**0**
Mar $\sigma0$ (MFH)*	**0**	**0**	**0**	**0**
Mar K (MFH)*	**0**	**0**	**0**	**0**
Aspect Ratio (MFH)*	**0**	**0.150**	**0.29**	**-0.033**

Fer K (FEA)*	**0.599**	**0.504**	**1.04**	****NV**
Fer σ0 (FEA)*	**0.689**	**0.467**	****NV**	****NV**
%Mar (FEA)*	**0.137**	**0.258**	****NV**	****NV**
Mar σ0 (FEA)*	**0**	**0**	**0**	**0**
Mar K (FEA)*	**0**	**0**	**0**	**0**
Aspect Ratio (FEA)*	**-0.168**	**0.084**	****NV**	****NV**

*Two homogenization methods (MFH, FEA) are used separately to calculate results.

Table 4.52 Effect of Input Parameters Scale

	Sensitivity Factor
No Effect, No valid curve	0
Low Effect	<0.25
Medium Effect	0.25<SF<0.50
High Effect	>0.50

- Dramatic effect of ferrite strength on both DP Steel’s yield stress and UTS can be found on Table 4.51. As expected, increase in harder and stronger phase martensite give rise to strength of DP steel. In this case high dislocation density sub-structure provides strengthening due to dislocation-dislocation interactions in lath type martensite[73].

- Outputs of sensitivity analysis showed that martensite yield strength and strain hardening coefficients can be fixed to simplify the model for all specimens since there is no effect on the mechanical material behavior. Independence of DP steels of martensite strength is observed in sensitivity analysis. It is shown that up to 50-60% martensite there is no effect of martensite yield strength on mechanical properties of DP Steels. Because at small strains, martensite islands only deform elastically.

- Additionally, it is seen from the calculated ferrite and martensite flow curves strain hardening exponent (n) are same for the same phases independent from the chemical composition, because of the default strain hardening exponent values for individual phases in JMatPro software. Due to this situation, it is seen that the general strain hardening exponent of the steel did not change either.Consequently, it is decided that for all DP steel specimens following values are fixed with average values as follows to simplify and optimize the model as shown in Table 4.53:

Martensite yield stress = 2800 MPa   Martensite K = 900

Martensite n = 0.29   Ferrite n = 0.26

4.2.2 Uniaxial Tensile Test Model of DP Steel Specimens

The required inputs for mechanical modeling can be summarized as follows:

- Yield Stress of Ferrite is found from JMatPro ferrite true stress-strain curve
- Yield Stress of Martensite is found from JMatPro martensite true stress-strain curve (fixed according to sensitivity analysis)
- Strain hardening Coefficient of martensite (n) is found from power law data processing with least square error minimization of JMatPro true stress-strain curve (fixed according to sensitivity analysis)
- Strain hardening Coefficient of ferrite (n) is found from power law data processing with least square error minimization of JMatPro true stress-strain curve (fixed according to sensitivity analysis)

- Strain hardening exponent (K) is found from power law data processing with least square error minimization of JMatPro true stress-strain curve
- Martensite fraction is found by metallographic examination (image processing with Climax)
- Elastic modulus, Poisson's ratio, density is taken from literature, general low alloy steel values are used since physical properties does not change dramatically ($E_{martensite}$ = 209000, $E_{ferrite}$=206000, v = 0.29, d = 7.9 g/cm3).

Table 4.53 Final Input Values to be Fed to Mechanical Models

	SSAB DP590	**SSAB DP800**	**BOR DP600**	**BOR DP800**
Fer σ0 (MPa)	308	382	332	375
Fer K (MPa)	505	550	535	555
***Fer n**	0.25	0.25	0.25	0.25
***Mar σ0 (MPa)**	2800	2800	2800	2800
***Mar K (MPa)**	900	900	900	900
***Mar n**	0.3	0.3	0.3	0.3
Aspect Ratio of Martensite	1.5	1.5	2	1.25
Martensite Fraction (Vol%)	18	35	21	37

**These parameters are fixed to the average values of DP steel in order to simplify the mechanical models, as they do not significantly affect the outputs according to the sensitivity analysis.*

4.2.2.1 Flow Curves of DP Steel Specimens

Uniaxial stress-strain curves are calculated individually for 0° and 90° for all samples used in the thesis, BOR-DP600, SSAB-DP600, BOR-DP800, and SSAB-DP800, using the input values provided above in Table 4.53. Homogenization methods FEA-2D, FEA-3D and MFH are used separately in modeling. Results are compared with the experimental uniaxial stress-strain curves of the samples. Model results and their comparison with experimental data are given in the figures below with engineering stress-strain, true stress-strain and metal forming stress-strain curves (Figure 4.25 to Figure 4.31). Also, 2D-FEA and 3D-FEA stress and strain distribution field results can be seen in below figures (Figure 4.32 to Figure 4.39). FE-2D 90° uniaxial model field results can be found in the Appendix A.

4.2.2.1.1 SSAB-DP600 Specimen Uniaxial Test Model Curves

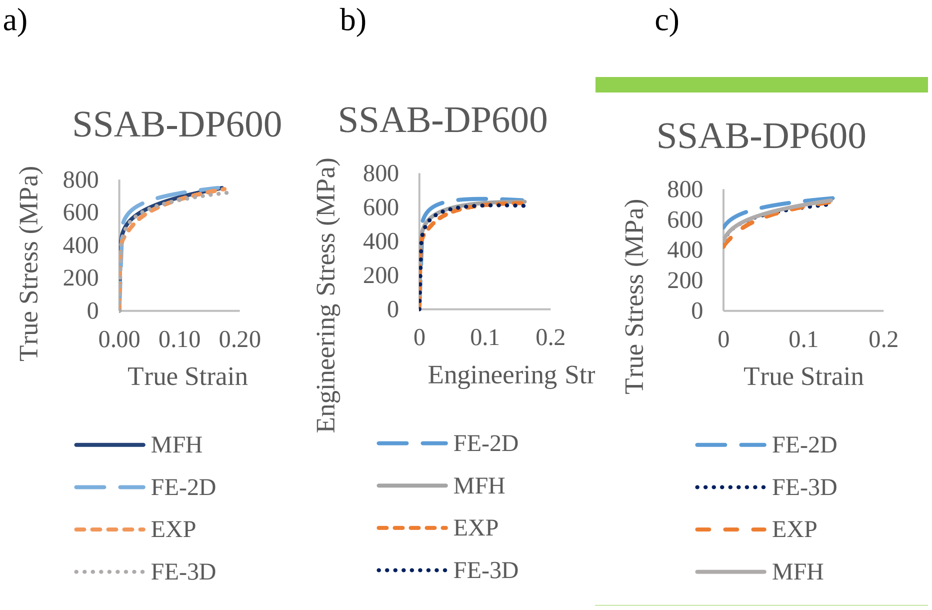

Figure 4.25. SSAB-DP600, 0° Uniaxial test model and experimental comparison results a) True Stress-Strain Curve b) Engineering Stress-Strain curves c) Metal Forming Curves

True stress-strain, engineering stress strain and metal forming curves of SSAB-DP600 steel for 0° uniaxial tensile test model can be found at Figure 4.25 a, b, c respectively.

It can be said that all used homogenization methods in modeling make good estimations by staying within 10% error margin in estimating uniaxial tensile test curves.

While it has been found that the FEA approach is better able to capture the overall trend of the material flow curve and the behavior of strain hardening, it can also be said that the MFH method may compute flow curves with a trend that is similar to the experimental curve. The overprediction that occurs in all homogenization methods may be due to the inability to take into account all the aspects of deformation behavior of DP Steels.

True stress-strain, engineering stress strain and metal forming curves of SSAB-DP600 steel for 90° uniaxial tensile test can be found at Figure 4.26 a, b, c respectively. In addition to the comments above, it can be said that the MFH makes a very good estimation of the experimental curve in the 90° uniaxial model of BOR-DP600 sample, while the FEA-2D model is also within the acceptable error range with a certain amount of over prediction.

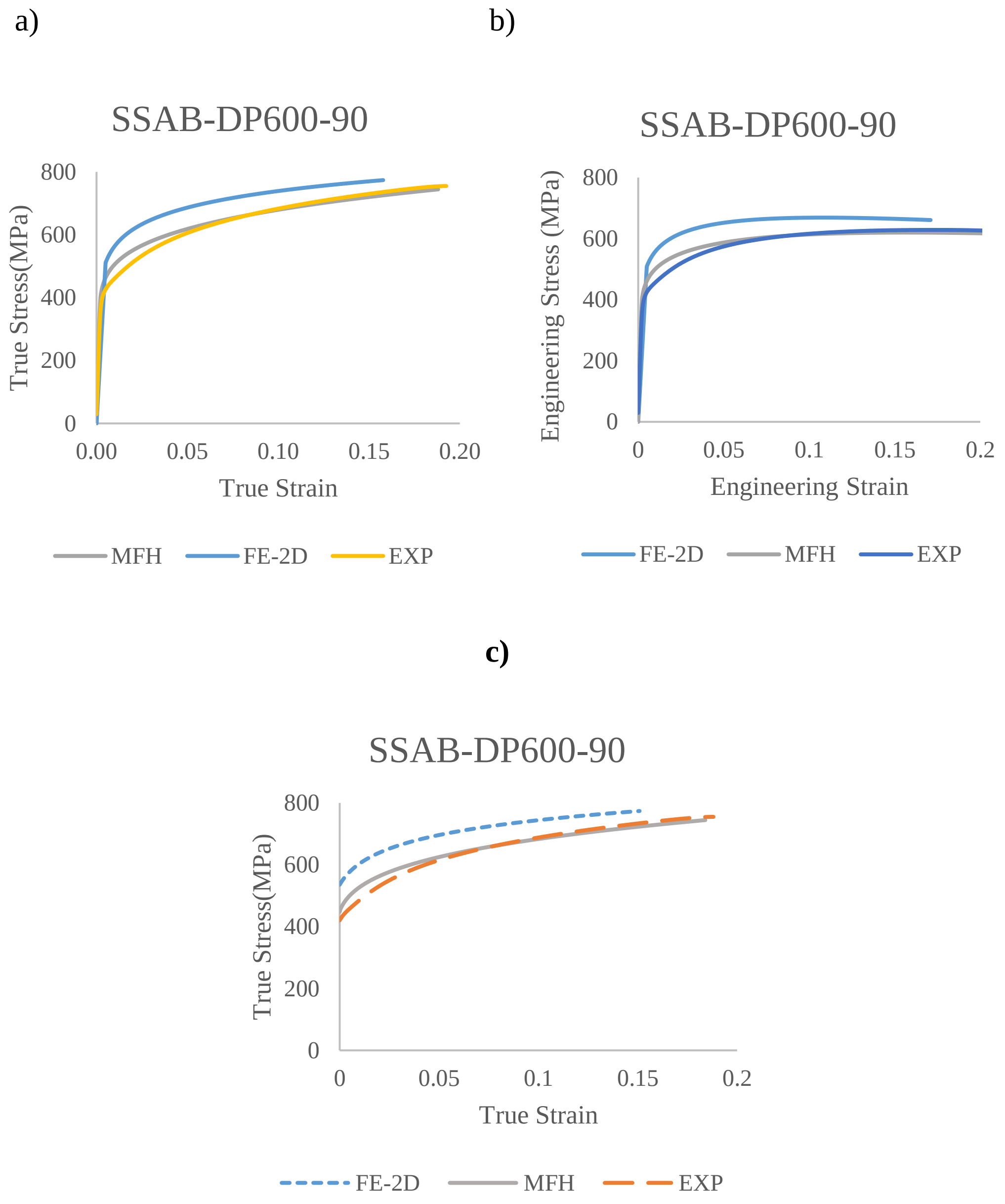

Figure 4.26. SSAB-DP600, 90^{o} Uniaxial test model and experimental comparison results a) True Stress-Strain Curve b) Engineering Stress-Strain curves c) Metal Forming Curves

4.2.2.1.2 SSAB-DP800 Specimen Uniaxial Test Model Curves

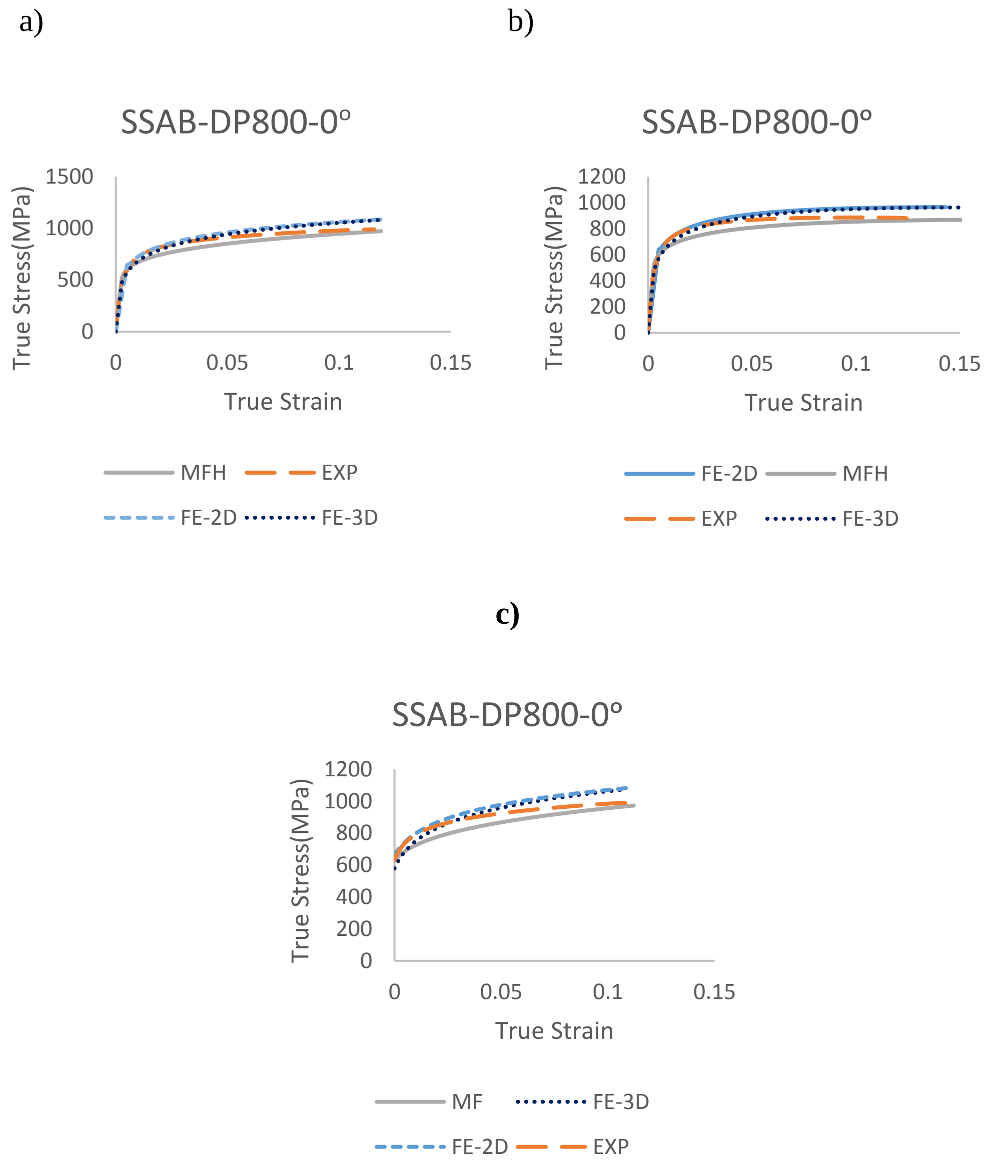

Figure 4.27. SSAB-DP800, 0° Uniaxial test model and experimental comparison results a) True Stress-Strain Curve b) Engineering Stress-Strain curves c) Metal Forming Curves

True stress-strain, engineering stress strain and metal forming curves of SSAB-DP800 steel for 0° uniaxial tensile test can be found at Figure 4.27 a, b, c respectively.

It can be said that all used homogenization methods in modeling make good estimations by staying within ~10% error margin in estimating uniaxial tensile test curves.

While FEA method predicts the low strain parts of the curve and the yield stress of the steel better, the MFH method makes a better estimation in the parts of the curve that reach high strains.

True stress-strain, engineering stress strain and metal forming curves of SSAB-DP800 steel for 90° uniaxial tensile test can be found at Figure 4.28 respectively.

Looking at the 90° uniaxial tensile test model results, it can be said that FEA-2D homogenization catches the experimental curve with a very close trend, while MFH’s prediction is slightly outside the ~10% error margin.

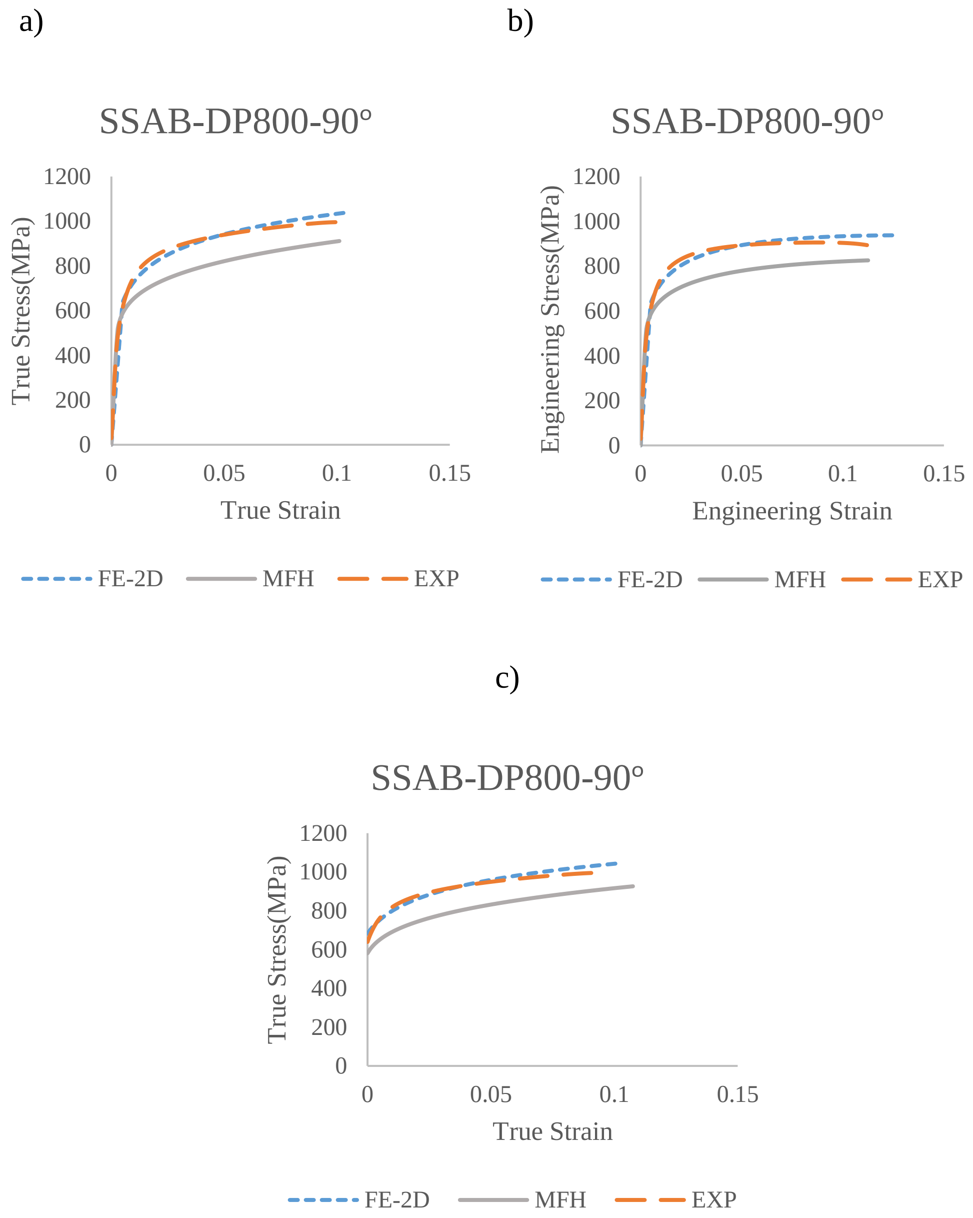

Figure 4.28. SSAB-DP800, 90° Uniaxial test model and experimental comparison results a) True Stress-Strain Curve b) Engineering Stress-Strain curves c) Metal Forming Curves

4.2.2.1.3 BOR-DP600 Specimen Uniaxial Test Model Curves

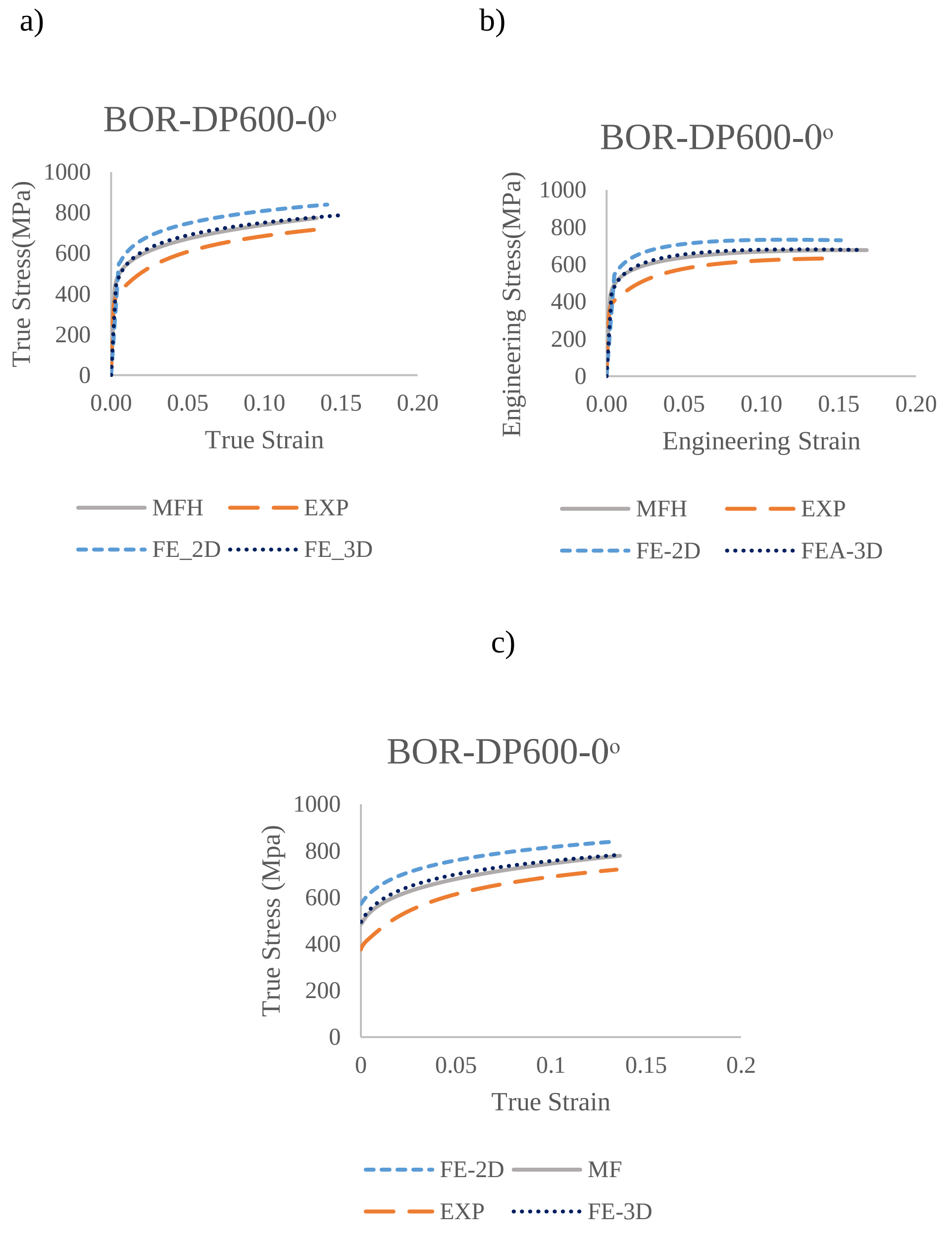

Figure 4.29. BOR-DP600, 0° Uniaxial test model and experimental comparison results a) True Stress-Strain Curve b) Engineering Stress-Strain curves c) Metal Forming Curves

True stress-strain, engineering stress strain and metal forming curves of BOR-DP600 steel for 0° uniaxial tensile test can be found at Figure 4.29 a, b, c respectively.

When looking at the results of the BOR-DP600 sample, there is an over prediction in all methods. In particular, the results from the homogenization with the FEA-2D method are far from the acceptable error band. This can be explained by the fact that the model predicts higher strength values than expected due to the smaller grain size of the cold rolled BOR-DP600 sample (4.07 µm) compared to DP600 grade steels.

True stress-strain, engineering stress strain and metal forming curves of BOR-DP600 steel for 90° uniaxial tensile test can be found at Figure 4.30 respectively.

Although over prediction was obtained with all homogenization methods with similar results in this model like 0° uniaxial tensile test model, the results came closer to the acceptable ~10% error limit.

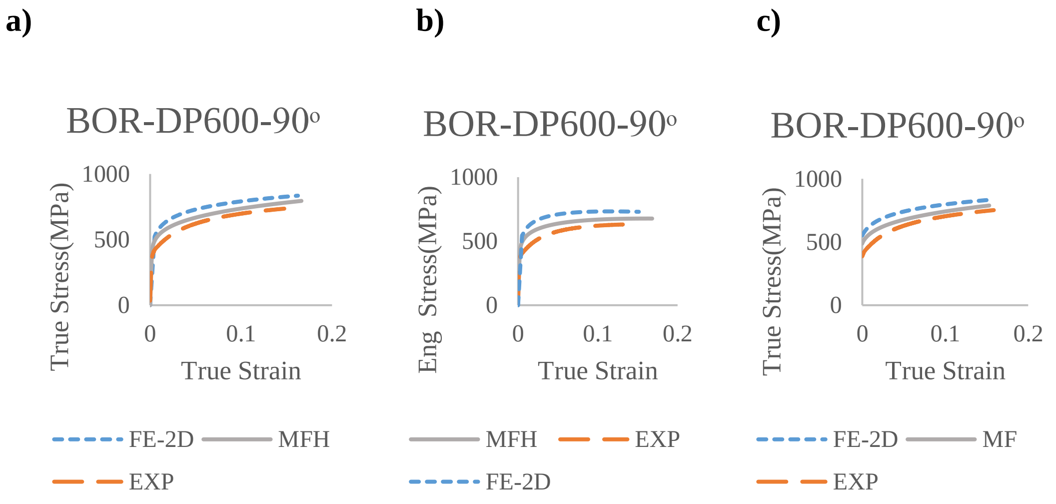

Figure 4.30. SSAB-DP600, 90° Uniaxial test model and experimental comparison results a) True Stress-Strain Curve b) Engineering Stress-Strain curves c) Metal Forming Curves

4.2.2.1.4 BOR-DP800 Specimen Uniaxial Test Model Curves

Table 4.54 Calculated yield stress (0.2%) and UTS values of BOR-DP800 specimen and comparison with experimental data for 0° uniaxial tensile test

	MFH	**FE-2D**	**FE-3D**	**EXP**
Yield Stress (0.2%)	596	694	581.92	516.5
UTS	863	826.5	959.96	827.78

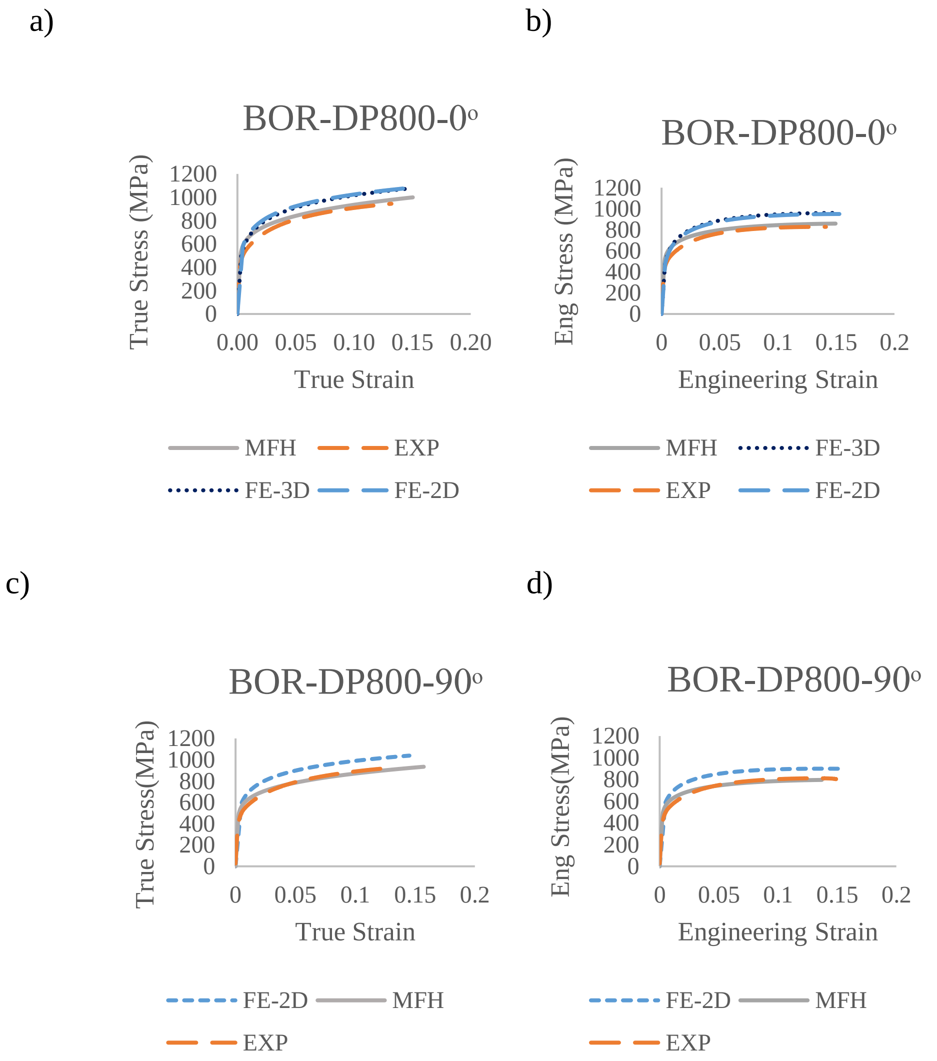

Figure 4.31. BOR-DP800, Uniaxial test model and experimental comparison results a) 0° True Stress-Strain Curve b) 0° Engineering Stress-Strain curves c) 90° True Stress-Strain Curve d) 90° Engineering Stress-Strain curves

True stress-strain and engineering stress strain curves of BOR-DP800 steel for 0° uniaxial tensile test can be found at Figure 4.31a and Figure 4.31b respectively.

When predicting uniaxial tensile test curves, used homogenization methods produce good estimates that are within a 10% error margin, while the findings of FEA-2D and FEA-3D analyses are close to the upper bound. As in the case of BOR-DP600 steel, the smaller grain size in the cold rolled samples may have contributed to the over-prediction by increasing strength estimates.

Although the MFH results are closer to the experimental result, it can be said that the FEA-2D and FEA-3D methods work better in capturing the general flow trend. True stress-strain and engineering stress strain curves of BOR-DP800 steel for 90° uniaxial tensile test can be found at Figure 4.31c and Figure 4.31d respectively. Similar results as stated above can be seen in these Figures.

4.2.2.2 Field Results of DP Steel Specimens

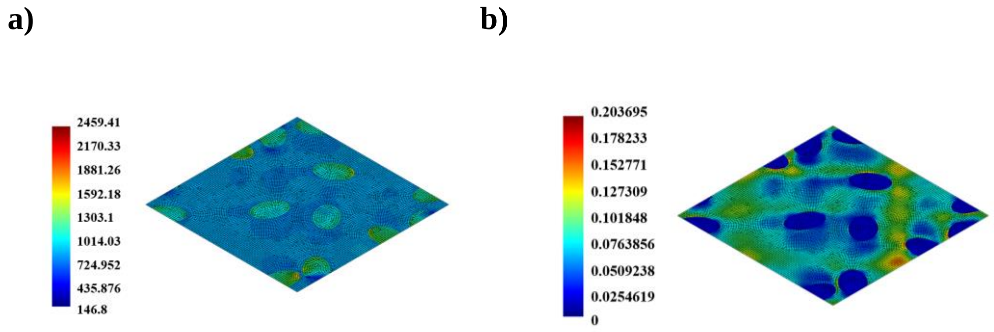

Figure 4.32. SSAB-DP600 0° Uniaxial Model 2D Field Results a) Equivalent Von-Mises Stress Distribution (MPa)b) Equivalent Plastic Strain

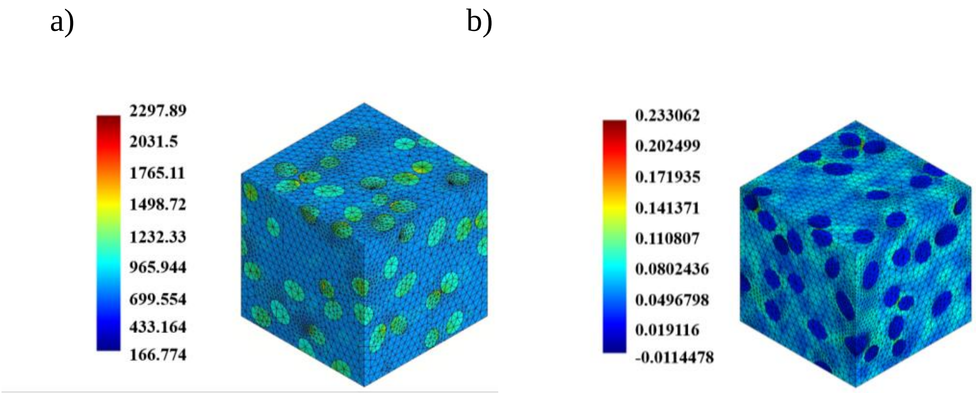

Figure 4.33. SSAB-DP600 0° Uniaxial Model 3D Field Results a) Equivalent Von-Mises Stress Distribution (MPa) b) Equivalent Plastic Strain

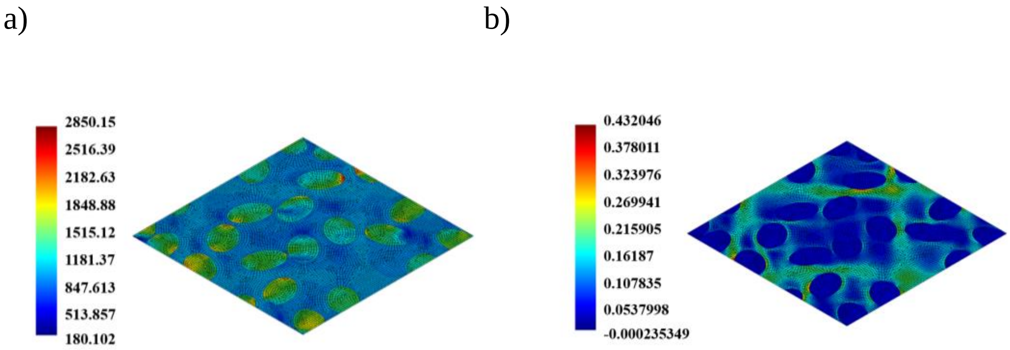

Figure 4.34. SSAB-DP800 0° Uniaxial Model 2D Field Results a) Equivalent Von-Mises Stress Distribution (MPa) b) Equivalent Plastic Strain

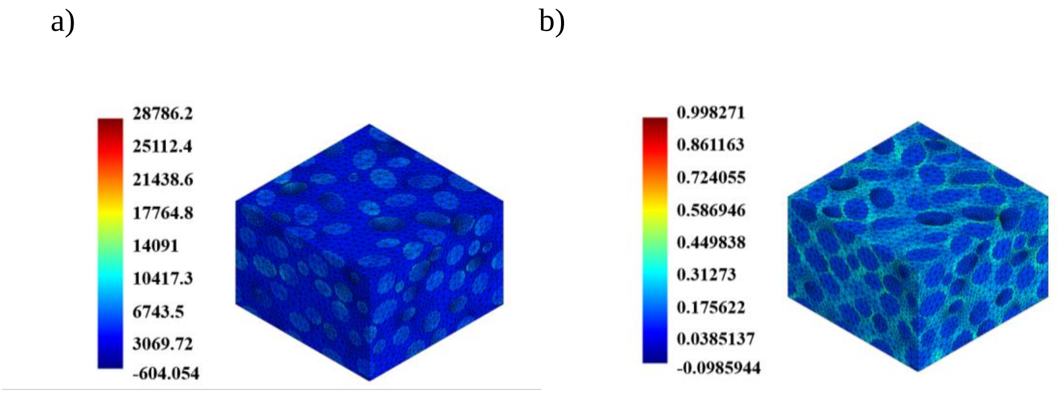

Figure 4.35. SSAB-DP800 0° Uniaxial Model 3D Field Results a) Equivalent Von-Mises Stress Distribution (MPa) b) Equivalent Plastic Strain

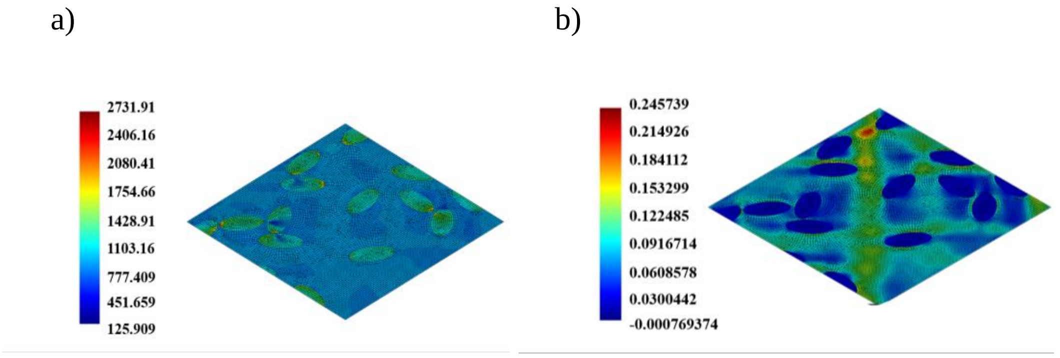

Figure 4.36. BOR-DP600 0° Uniaxial Model 2D Field Results a) Equivalent Von-Mises Stress Distribution (MPa) b) Equivalent Plastic Strain

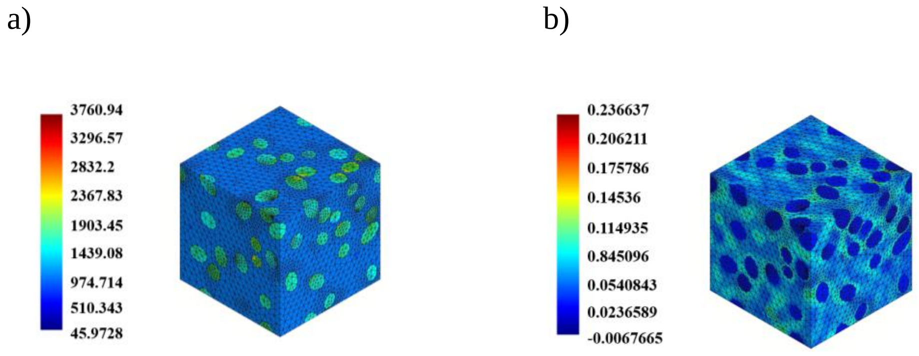

Figure 4.37. BOR-DP600 0° Uniaxial Model 3D Field Results a) Equivalent Von-Mises Stress Distribution (MPa) b) Equivalent Plastic Strain

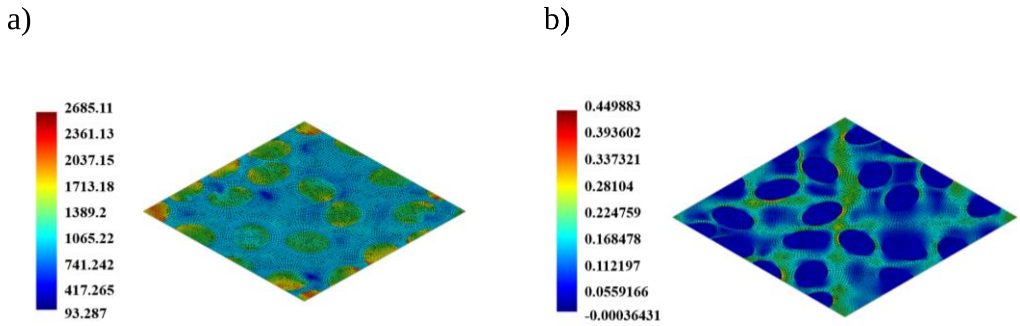

Figure 4.38. BOR-D800 0° Uniaxial Model 2D Field Results a) Equivalent Von-Mises Stress Distribution (MPa) b) Equivalent Plastic Strain

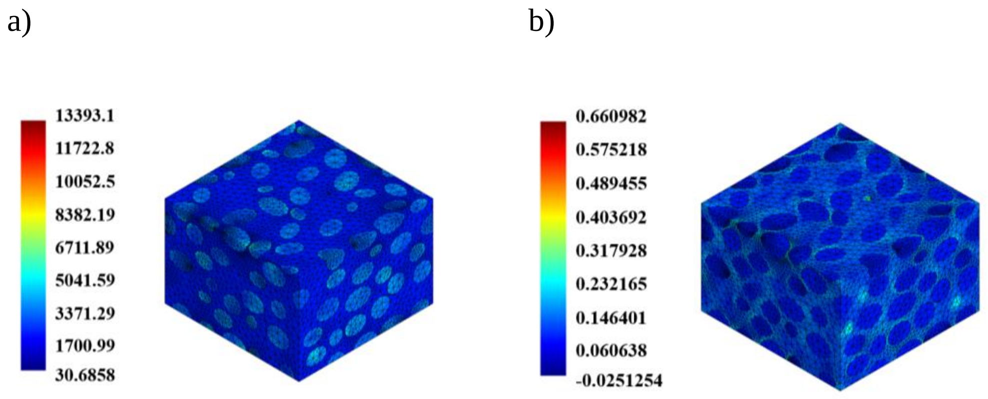

Figure 4.39. BOR-DP800 0° Uniaxial Model 3D Field Results a) Equivalent Von-Mises Stress Distribution (MPa) b) Equivalent Plastic Strain

Equivalent Von-Mises Stress and equivalent plastic strain field results of FEA-2D and FEA-3D analyzes are given in the figures (Figure 4.32 to Figure 4.39) above for all DP Steel specimens SSAB-DP600, SSAB-DP800, BOR-DP600 and BOR-DP800.

According to these results:

- The deformation and degree of elongation in DP steels are controlled by the softer and more ductile ferrite phase, which regulates the material's ductility by achieving higher plastic strain values than the martensite phase.
- It can be understood from the high Von-Mises stress values at martensite islands, which are harder and have higher strength, are the load-bearing phase of DP steels. Also, from the component 11 stress distribution after deformation while there is compressive stresses on the martensite islands, tensile stresses on the ferrite matrix can be seen.
- Regions where the amount of Equivalent Von Mises Stress reaches its maximum are on the martensite islands in the regions close to the ferrite martensite interface, while the maximum plastic strain regions are seen at the ferrite-martensite interface, especially in the regions where the martensite islands are concentrated. This outcome explains the deformation mechanism

of DP steels, mechanical property differences between ferrite and martensite and the inhomogeneous deformation behavior triggers the crack initiation. Ferrite, which is a softer phase, under any load begins to deform much faster than martensite and creates a shear force at the phase interface. When the ferrite phase is highly deformed, the high strain gives rise to deformation of the martensite phase.

- A composite structure with high strength and ductility is created when the martensite phase, which has a high load carrying capability, and the ferrite phase, which can achieve high ductility values.

4.2.3 Calculation of Cyclic Stress-Strain Curves

Remaining part of the mechanical flow chart is shown in below Figure 4.40.

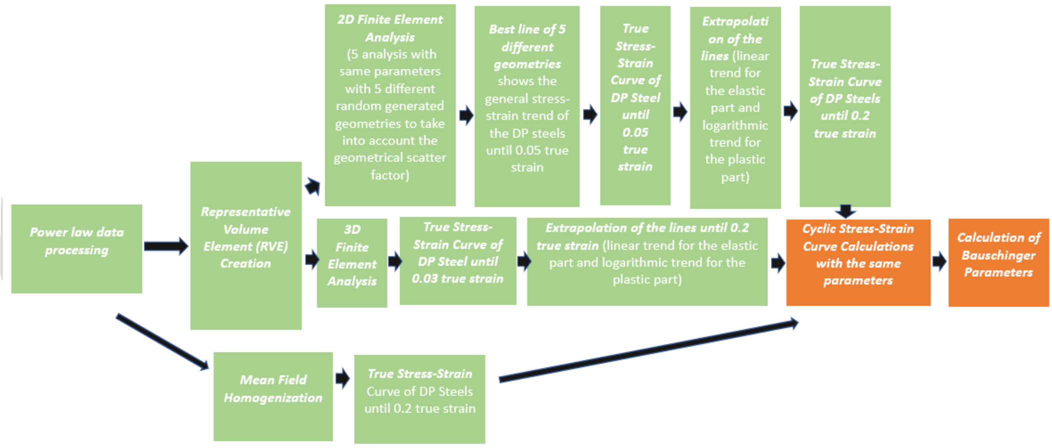

Figure 4.40. Mechanical Modeling Procedure Flowchart-2

In the final phase of the thesis, the Bauschinger parameters are calculated by making the cyclic tension-compression test models. MFH and FEA homogenization methods are used separately as in the uniaxial test modeling.

Although it is a phenomenon known for many years in DP steels and has a great impact on metal forming, the spring back effect in material models has not been included in the model calculations before. With the completion of this phase of the thesis, the spring back behavior of the DP steels is revealed by following a methodology based on the ICME principles, in which the inputs obtained starting from the thermodynamic-based modeling are fed into the mechanical models. While the Bauschinger effect is included in the models, the back stress mechanism, which is the most effective mechanism in the spring back behavior of multi-phase materials, has been added to the calculations. Since the spring back caused by mechanisms such as dislocation pile-up at the grain boundaries or Orowan looping mechanism has a much more negligible effect on DP steels they are not included in model calculations.

It is mentioned in the literature review part that there is not yet a standard way to quantify the Bauschinger effect, but there are various methods used for this purpose. In this thesis, general Bauschinger parameters to quantify the Bauschinger effect Bauschinger Stress Parameter (βσ), Bauschinger Strain Parameter (βε), Bauschinger Energy Parameter (βE), Ratio of Directional hardening to isotropic hardening (B*) and P_{isot} isotropic hardening fraction number are used with the following equations:

Bauschinger Stress Parameter (βσ):

$$\beta\sigma = \frac{\sigma(+) - \sigma(-)}{2\sigma(+)} \quad \textbf{\textit{(Eqn.14)}}$$

Bauschinger Strain Parameter (βε):

$$\beta\varepsilon = \frac{\varepsilon b}{\varepsilon 0} \quad \textbf{\textit{(Eq.15)}}$$

Bauschinger Energy Parameter (βE):

$$\beta E = \frac{Eb}{E0} \quad \textbf{\textit{(Eqn.16)}}$$

Ratio of Directional hardening to isotropic hardening:

$$\beta^{*} = \frac{(\sigma(+) - \sigma(-))}{2(\sigma(+) - \sigma 0)} \quad \textbf{\textit{(Enq.17)}}$$

Isot Fraction of isotropic hardening:

$$P_{isot} = \frac{1}{1+\beta *} \quad \textbf{\textit{(Eqn.18)}}$$

After cyclic tension-compression model outputs are obtained for one complete cycle for each simulation, Cumulative absolute plastic strain vs true stress curves are calculated by subtracting the elastic strain from total strain of the material as shown in Figure 4.41a, Figure 4.41b.

$$\varepsilon_p = \varepsilon_{total} - (\sigma/E) \quad \textbf{\textit{(Eqn.19)}}$$

a) b)

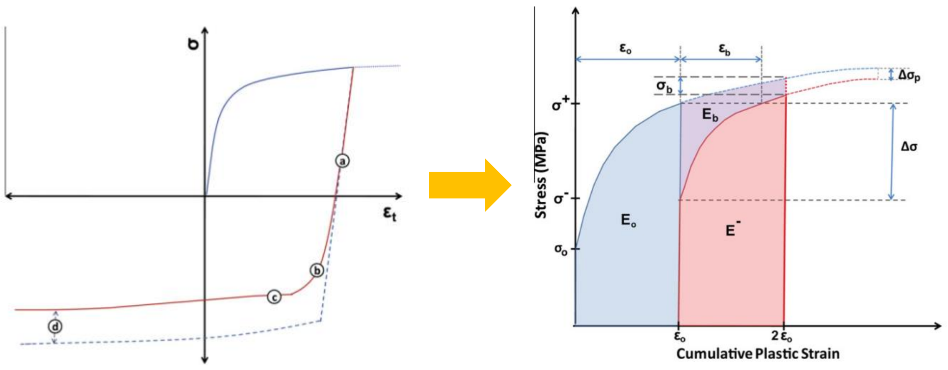

Figure 4.41. a) One half cycle of tension-compression model b) Cumulative plastic strain vs Stress (MPa) curve

4.2.3.1 Cyclic Stress-Strain Parametric Analysis

In this part of the thesis effect of %Carbon, %Martensite and IAT on cyclic stress strain curves and Bauschinger effect is examined by parametric analysis and sensitivity analysis on a fictitious DP steel.

A sensitivity analysis is performed on cyclic-stress strain curves to see the potential effects on the Bauschinger effect, since these 3 parameters are interrelated and effective on steel strength as shown in the previous sensitivity analysis for uniaxial tensile loading.

It is known that:

- Both % Martensite and %C are effective in increasing the strength of DP Steels.
- Martensite after quenching for the same IAT increases when %C in steel increases. Relatedly, increasing steel strength may contribute to an increase in the Bauschinger Effect.
- Due to the nature of the IA zone, as IAT is raised for steel with the same chemical composition, austenite content increases while carbon in austenite decreases, which has opposite effects on the steel's strength. This trade-off must be considered to make steel with the best possible parameters.

To perform sensitivity analysis on these 3 parameters related to each other, firstly input parameters to be used are determined. Then, Bauschinger parameters are obtained by processing the data in the obtained curves. To see the effect of pre-strain, 0.02, 0.04, 0.05, 0.07 and 0.08 pre-strain are used for each parameter to be tested.

Parametric Analysis Inputs:

Input-1.1: %C (0.05, 0.1, 0.15) (FEA), Input-1.2: %C (0.05, 0.1, 0.15) (MFH)

Input-2.1: %M (15%, 30%, 45%) (FEA), Input-2.2: %M (15%, 30%, 45%) (MFH)

Input-3.1: IAT (715^{o}C, 750^{o}C, 775^{o}C, 790^{o}C, 800^{o}C) (FEA), Input-3.2: IAT (715^{o}C, 750^{o}C, 775^{o}C, 790^{o}C, 800^{o}C) (MFH)

Outputs: $\beta\sigma$, $\beta\varepsilon$, BE, B*, P isot (for pre-strains of 0.02, 0.04, 0.05, 0.07, 0.08)

After the model results are acquired, two different comparison graphs are created. The first graphs show how various input factors affect cyclic stress-strain curves at a single pre-strain value. Second graphs represent the effect of pre-strain while keeping input parameters fixed. MFH and FEA methods are applied separately to the models for comparison.

4.2.3.1.1 Effect of %Carbon Cyclic Stress-Strain Curves

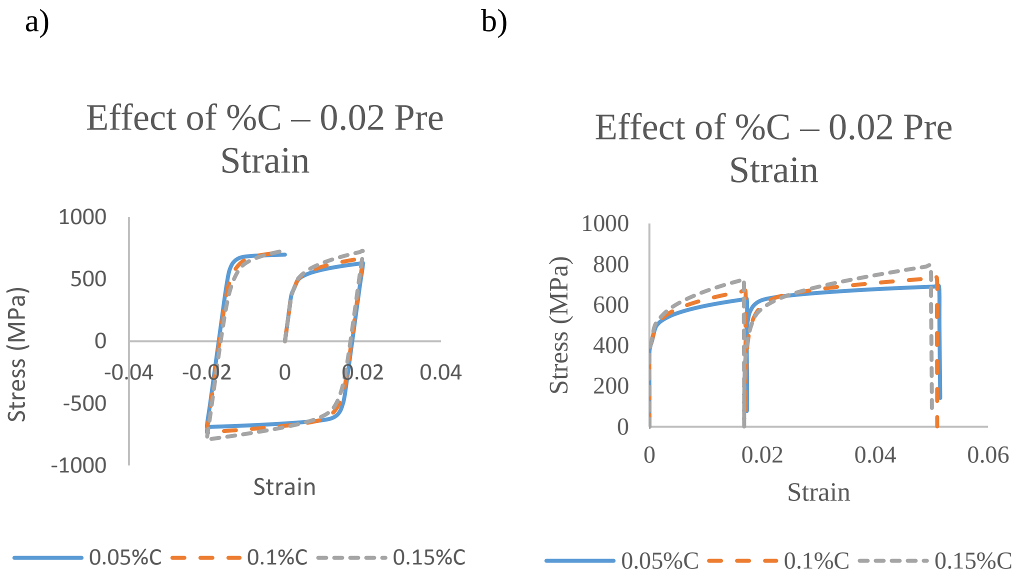

Figure 4.42. FEA Results for Same Pre-Strain and Different Amount of %Carbon a) Cyclic Stress-Strain Curve b) Cumulative plastic strain vs Absolute Stress Curve

Figure 4.42a and Figure 4.42b represents the FEA model results of cyclic stress strain behavior of a fictitious DP steel with varying %Carbon from 0.15% to 0.30% and 0.45%. From these two figures:

- As the %C rises, the curves become more asymmetric, especially when approaches the 0.15%. This demonstrates that as the %C rises, the Bauschinger effect intensifies. Likewise, the degree of transient softening seen in the steel increases as the amount of carbon in the material does.

Figure 4.43a and Figure 4.43b represents the MFH model results of cyclic stress strain behavior of a fictitious DP steel with varying %C. Here, similar remarks about the FEA method might be made.

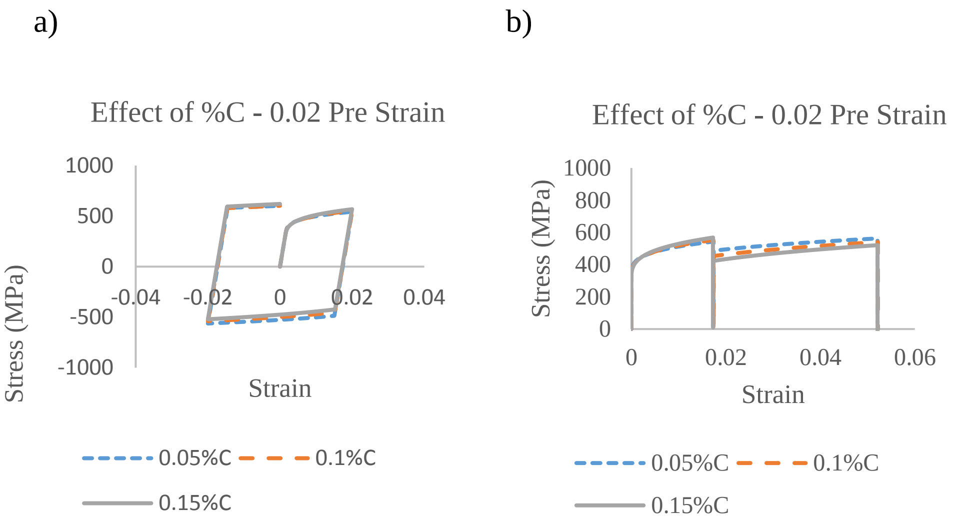

Figure 4.43. MFH Results for Same Pre-Strain and Different Amount of %Carbon, a) Cyclic Stress-Strain Curve b) Cumulative plastic strain vs Absolute Stress Curve

4.2.3.1.2 Effect of %Martensite Cyclic Stress-Strain Curves

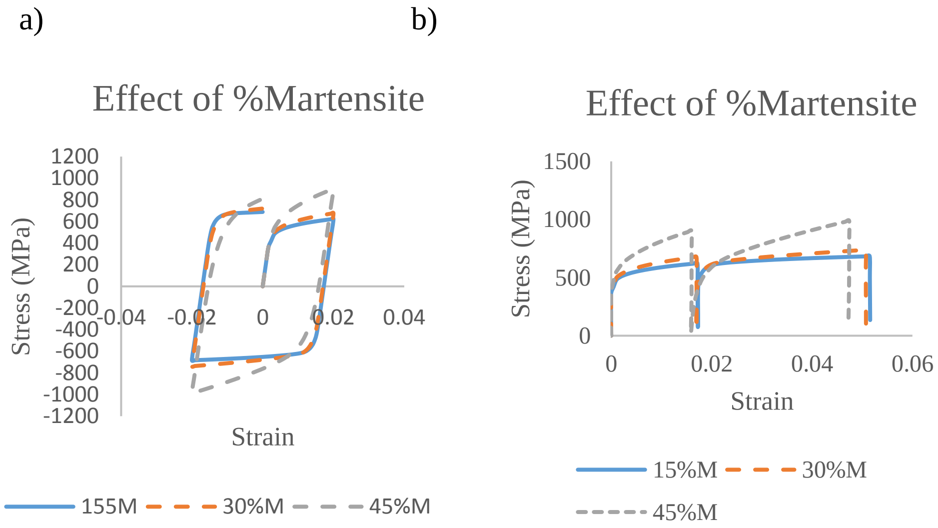

Figure 4.44. FEA Results, Effect of %Martensite for Same Pre-Strain and Different Amount of Martensite, a) Cyclic Stress-Strain Curve b) Cumulative plastic strain vs Absolute Stress Curve

Figure 4.44a and Figure 4.44b represents the FEA model results of cyclic stress strain behavior of a fictitious DP steel with varying %Martensite from 15% to 30% and 45%. From these two figures:

- It is obvious that when the volume fraction of martensite increases, the Bauschinger effect increases, and the asymmetry of the curves increases.
- Dramatic increase in asymmetry, especially when the amount of martensite reaches 45%, is related to the increase in the amount of martensite in volume, and the increase in stress and strain distributions, inhomogeneity between the ferrite and martensite phases, which are mechanically very different from each other.
- Likewise, as the %M in the steel increases, the amount of transient softening observed in the material increases.

Figure 4.45a and Figure 4.45b represents the MFH model results of cyclic stress strain behavior of a fictitious DP steel with varying %Martensite. It can be said that similar inferences with the inferences made from the FEA model can be made with the results from the MFH model.

As a result, it is seen that similar results are obtained for the 3 input parameters %Carbon, %Martensite and IAT. It has been mentioned in the previous sections that the increase of all three parameters increases the strength of the material. The sensitivity analysis coefficients are found with the parametric analysis data and the sensitivity analysis table is prepared to determine which parameter is more effective.

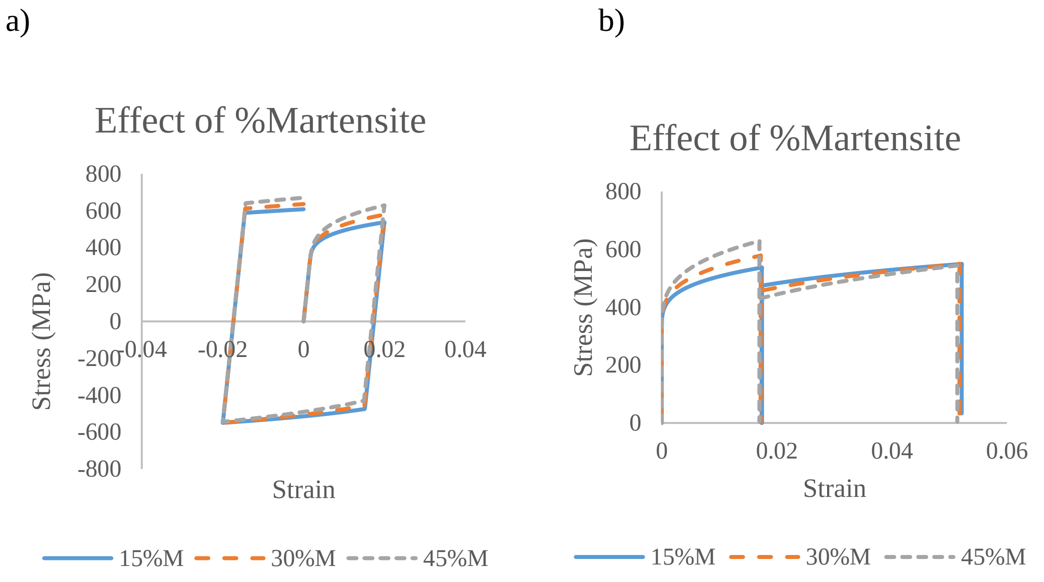

Figure 4.45. MFH Results for Same Pre-Strain and Different Amount of %Martensite a) Cyclic Stress-Strain Curve b) Cumulative plastic strain vs Absolute Stress Curve

4.2.3.1.3 Effect of IAT to Cyclic Stress-Strain Curves

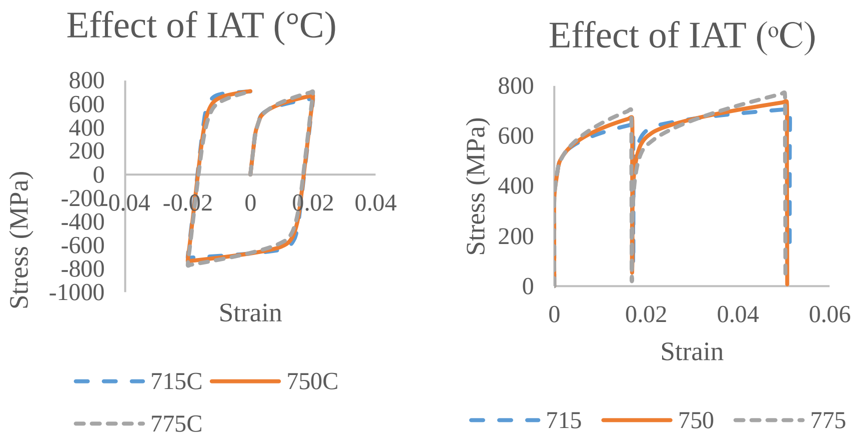

Figure 4.46. FEA Results, Effect of IAT for Same Pre-Strain a) Cyclic Stress-Strain Curve b) Cumulative plastic strain vs Absolute Stress Curve

Figure 4.46a and Figure 4.46b represents the FEA model results of cyclic stress strain behavior of a fictitious DP steel with varying IAT with 715 °C, 750 °C and 775 °C. From these two figures:

- It can be observed that the asymmetry of the curves increases as the amount of IAT increases which shows the increase in Bauschinger Effect.
- Also, increase in transient softening can be seen as the IAT increases.

Figure 4.47a and Figure 4.47b represents the MFH model results of cyclic stress strain behavior of a fictitious DP steel with varying IAT. Similar statements of the FEA method could be leveled at this point.

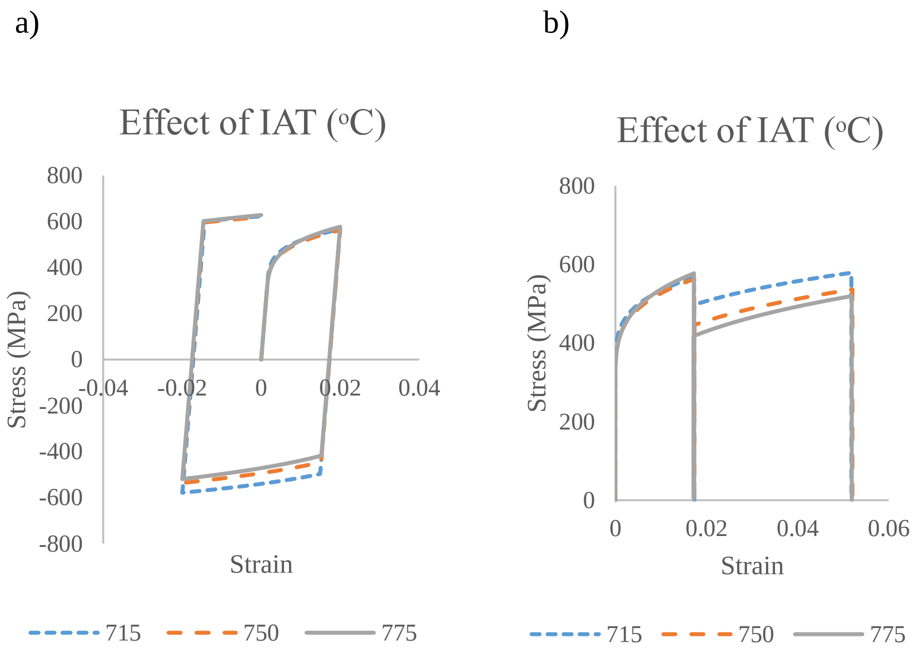

Figure 4.47. MFH Results, Effect of IAT for Same Pre-Strain a) Cyclic Stress-Strain Curve b) Cumulative plastic strain vs Absolute Stress Curve

<u>Bauschinger Parameters of Inputs:</u>

After calculating the cumulative absolute plastic strain vs true stress curves as shown above, Bauschinger parameters were calculated separately by processing the data outputs.

Figure 4.48, Figure 4.49, Figure 4.50, Figure 4.51, Figure 4.52 and Figure 4.53 represents the Bauschinger parameters for %C, %Martensite and IAT inputs.

4.2.3.1.4 Effect of %Carbon to Bauschinger Parameters for Different Pre-Strains

Bauschinger parameters calculated separately with two different homogenization methods MFH and FEA to see the effect of %Carbon on Bauschinger effect are given in the Figures below (Figure 4.48(a-d) and Figure 4.49(a-d)).

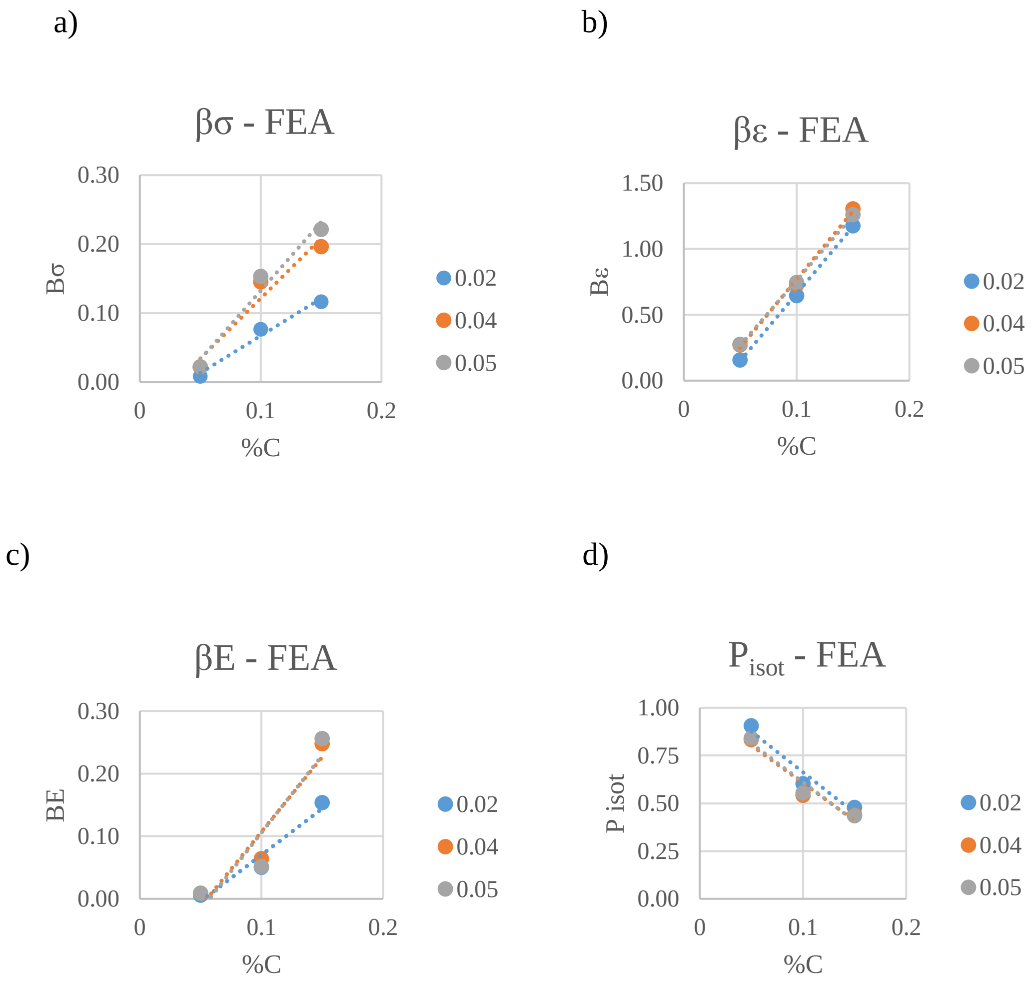

Figure 4.48. FEA Results, Effect of %Carbon to Bauschinger Parameters for Different Pre-Strains (FEA) a) βσ, b) βε, c) βE, d) P_{isot}

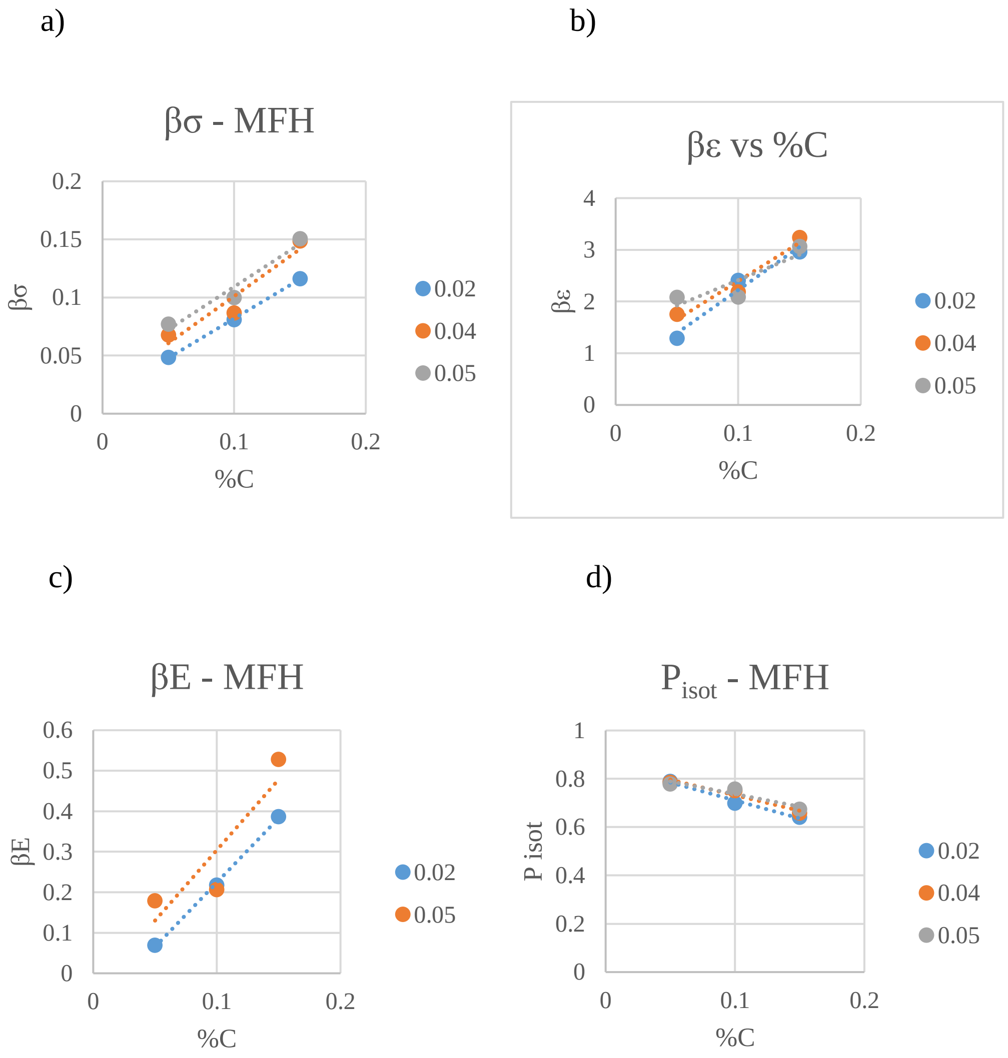

Figure 4.49. MFH Results, Effect of %Carbon to Bauschinger Parameters for Different Pre-Strains a) βσ, b) βε, c) βE, d) P_{isot}

- *βE parameter is not valid for 0.04 pre-strain*

4.2.3.1.5 Effect of %Martensite to Bauschinger Parameters for Different Pre-Strains

Bauschinger parameters calculated separately with two different homogenization methods MFH and FEA to see the effect of %Martensite on Bauschinger effect is given in the Figures below (Figure 4.50(a-d) and Figure 4.51(a-d)).

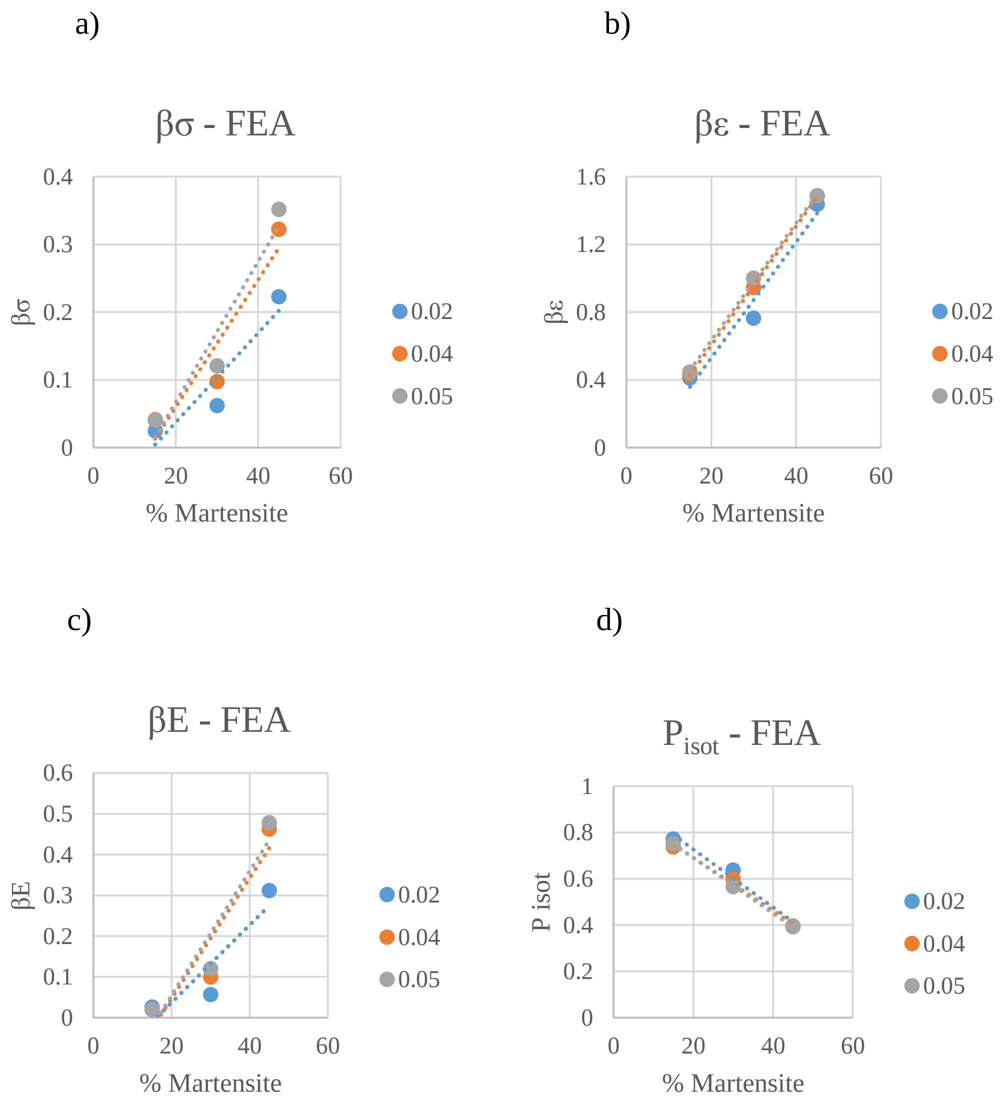

Figure 4.50. FEA Results Effect of %Martensite to Bauschinger Parameters for Different Pre-Strains a) βσ, b) βε, c) βE, d) P_{isot}

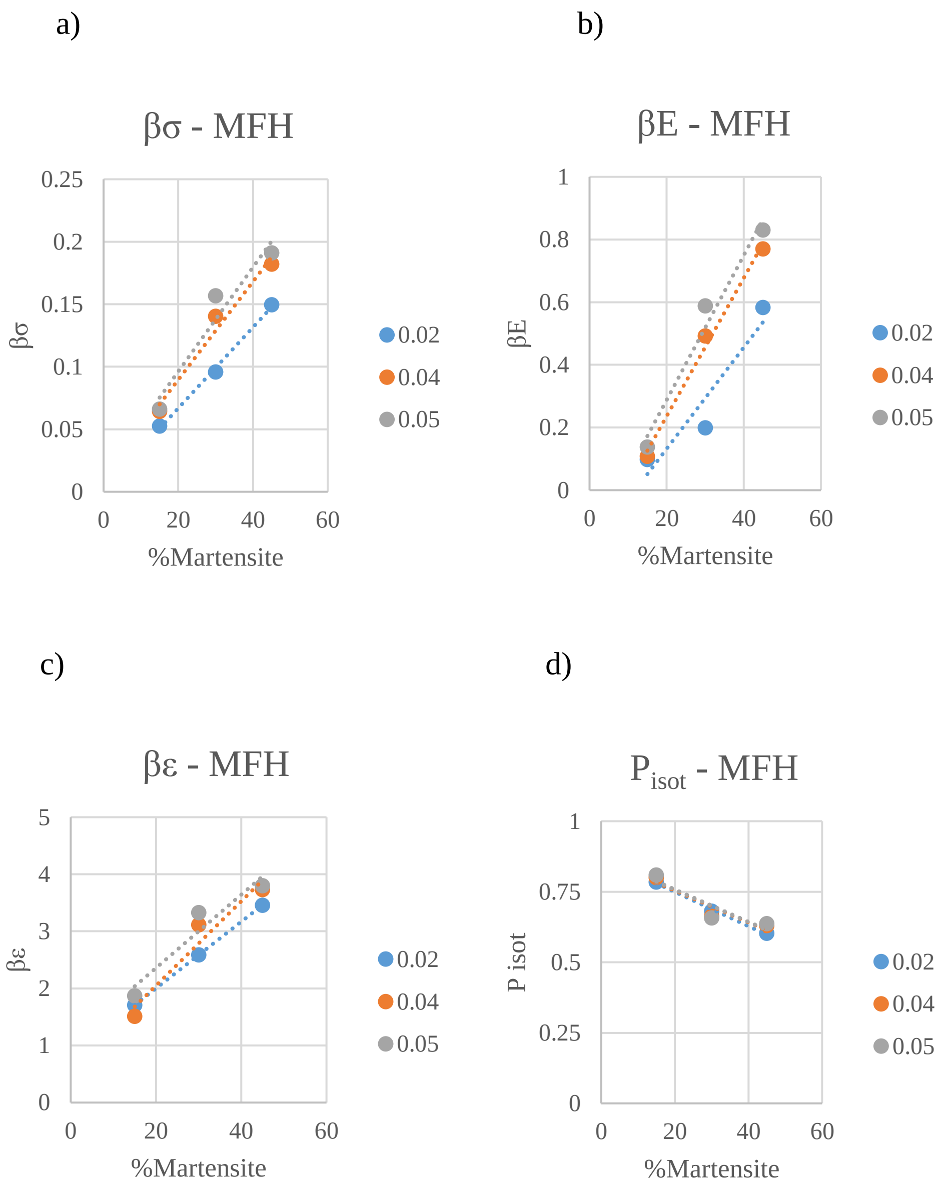

Figure 4.51. MFH Results, Effect of %Martensite to Bauschinger Parameters for Different Pre-Strains a) βσ, b) βε, c) βE, d) P_{isot}

4.2.3.1.6 Effect of IAT to Bauschinger Parameters for Different Pre-Strains

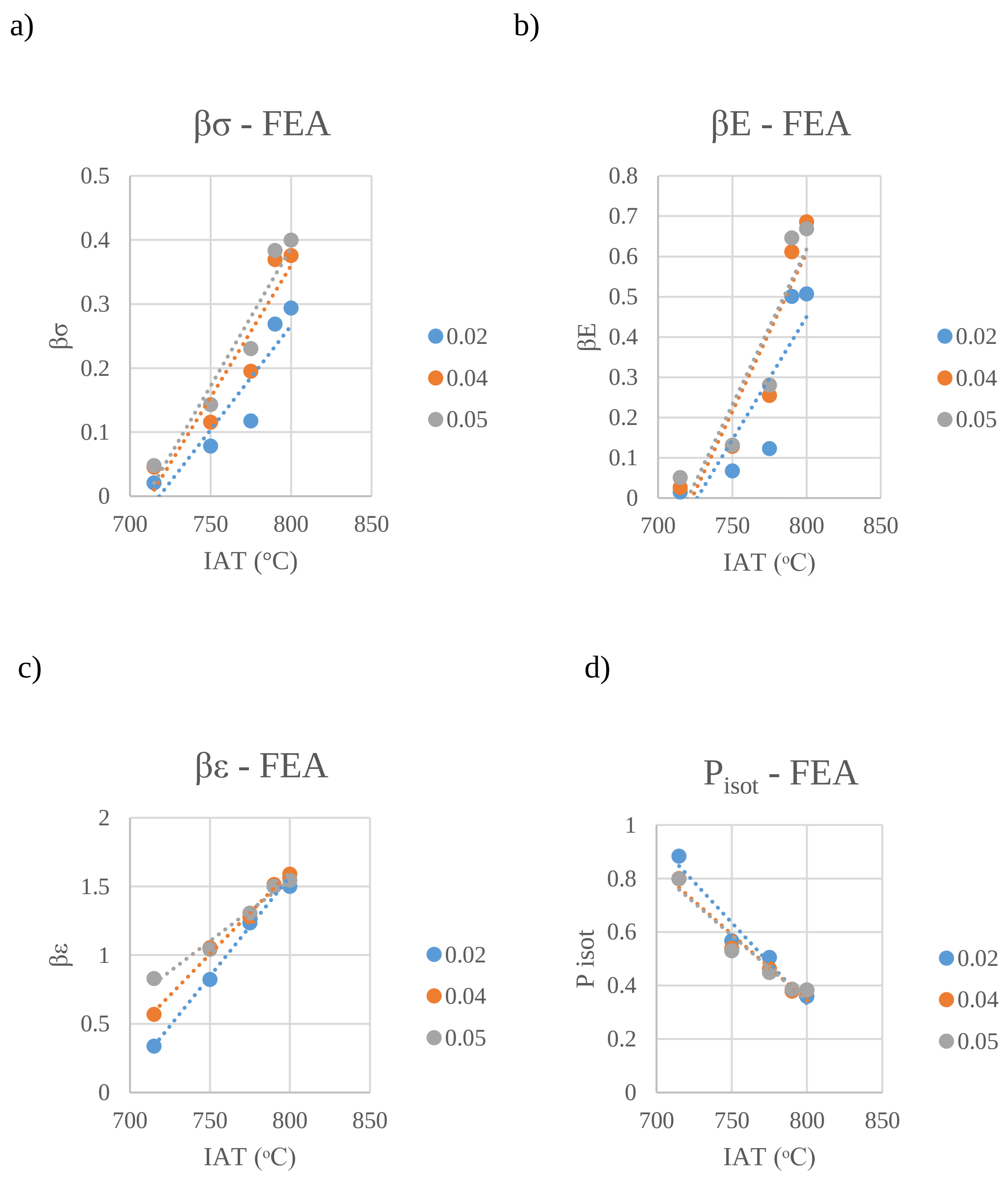

Figure 4.52. FEA Results Effect of IAT to Bauschinger Parameters for Different Pre-Strains a) βσ, b) βε, c) βE, d) P_{isot}

Bauschinger parameters calculated separately with two different homogenization methods MFH and FEA to see the effect of IAT on Bauschinger effect are given in the Figures below (Figure 4.52(a-d) and Figure 4.53(a-d)).

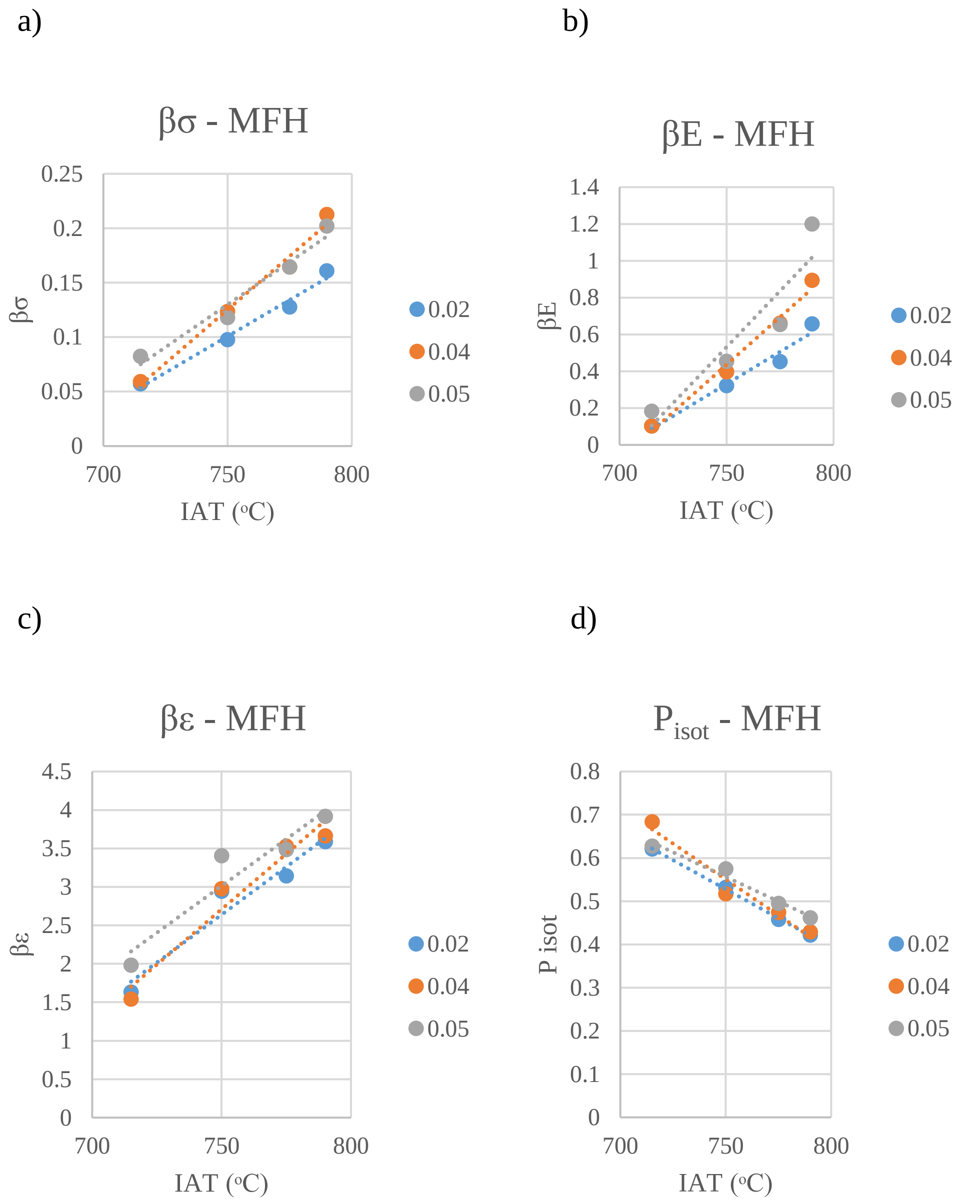

Figure 4.53. MFH Results Effect of IAT to Bauschinger Parameters for Different Pre-Strains a) βσ, b) βε, c) βE, d) P_{isot}

In summary:

- Although it does not always follow a completely linear line, it can be seen in both MFH and FEA solutions that Bauschinger parameters βσ, βε, βE increase as the pre-strain increases.
- As IAT, %Carbon or %Martensite increases Bauschinger Effect parameters βσ, βε and BE increases relatedly. Increasing asymmetry of cyclic stress strain curves shows the same indication.
- DP steels exhibit strain partitioning across the two phases during the straining process. For a given applied strain level, ferrite deforms significantly more than martensite. So, deformation in the ferrite phase will increase for a given applied strain level as the %Martensite or %Carbon rises.
- The fraction of non-recoverable hardening (P_{isot}) decreases as the %Carbon, %Martensite or IAT increases. In other words, reverse yield strength can be predicted more properly by the isotropic hardening model when the %Carbon, %Martensite or IAT is low but kinematic hardening becomes more prominent as the %Carbon, %Martensite or IAT increases.
- Bσ parameter results indicates that as %C, %Martensite or IAT increases, reduction in the flow stress increases after reversal of strain path.
- Bε parameter shows that as the %C, %Martensite or IAT increases, transient softening of the steel increases considerably.
- BE parameter shows that Bauschinger Energy increases from very low values ~0.05 to considerably high values 0.5-0.8 according to varying parameter as the %C, %Martensite or IAT increases.

MFH – FEA Comparison

- FEA method captures stress-strain transitions much better than MFH. Because MFH does not solve the RVE problem in detail therefore does not compute the detailed micro stress and strain fields in each phase and FEA method can bring better solutions to elastoplastic models.

- FEA model approximation shows more prominent effect in terms of βσ and P_{isot} parameters which are related with the premature yielding and non-recoverable hardening.
- MFH model approximation shows more prominent effect on BE and Bε parameters which are related to Bauschinger non-recoverable energy and transient softening.
- Strain reversal trends are captured better in the FEA approach, which provides a more comprehensive solution than the MFH approach.
- It is known that increase in both %Carbon and %Martensite increases the strength of the DP steel. Also, increasing IAT temperature dramatically affect the strength of the DP steel. In IA zone as the IAT increases obtained %Austenite increases but %Carbon in austenite decreases. So, it can be said that all these three parameters are inter-related to each other and there is a strength trade-off among them. So, to find the effect of these three parameters and their comparison on Bauschinger effect, Sensitivity Analysis is done by using parametric analysis data.

4.2.3.2 Cyclic Stress-Strain Sensitivity Analysis

The sensitivity analysis results for the %C, %Mar and IAT can be found in the Table-4.55 below.

Table 4.55 Dimensionless sensitivity factor of input parameters to output parameters on fictitious DP Steel for Cyclic Stress-Strain Analysis

Homogenization Method	**Input Parameter**	**Pre-Strain**	**βσ**	**βε**	**BE**	**B***	**P isot**
FEA	**%C**	**0.02**	1.4	1.6	2.9	1.5	-0.7
		0.04	1.2	1.4	3.7	1.3	-0.7
		0.05	1.3	1.3	4.8	1.4	-0.7
	%M	**0.02**	3.2	1.3	5.0	2.2	-0.6
		0.04	2.9	1.1	4.4	1.8	-0.6
		0.05	2.6	1.0	3.8	1.6	-0.6
	IAT	**0.02**	19.8	9.1	NV	15.2	-9.4
		0.04	16.3	7.3	24.0	11.7	-8.4
		0.05	14.5	5.2	21.3	10.3	-8.5
MFH	**%C**	**0.02**	0.8	0.7	-1.5	0.7	-0.2
		0.04	0.9	0.7	NV	0.7	-0.2
		0.05	0.7	NV	1.7	0.6	-0.1
	%M	**0.02**	1.0	0.7	2.4	0.8	-0.3
		0.04	0.8	0.7	7.5	5.5	-0.3
		0.05	0.8	0.6	1.2	0.6	-0.3
	IAT	**0.02**	8.5	6.2	13.5	6.7	-4.6
		0.04	9.4	6.1	11.9	7.8	-5.4
		0.05	8.0	5.4	14.5	5.9	-3.6

**NV represents the non-valid analysis result*

Values found in the sensitivity analysis table are given below Figure 4.54, Figure 4.55 and Figure 4.56 in column charts to indicate the results of FEA and MFH homogenization separately for each analyzed pre-strain value.

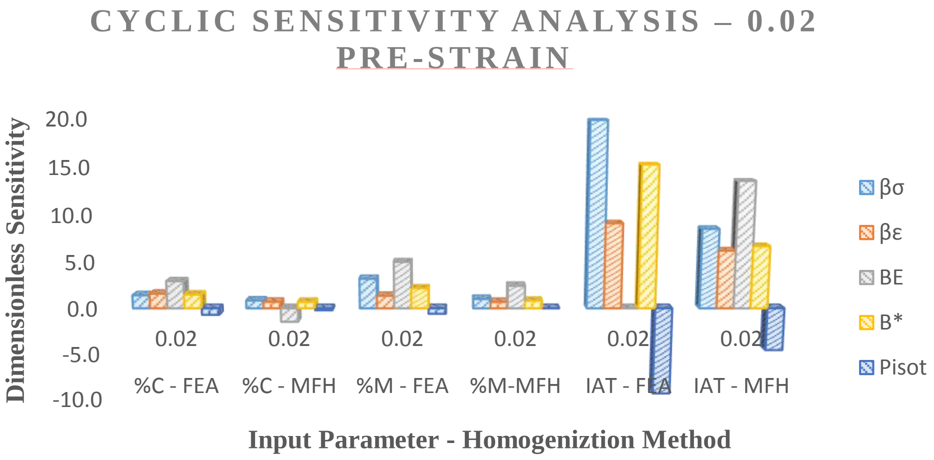

Figure 4.54. Dimensionless sensitivity comparison of FEA and MFH methods on Bauschinger Parameters, 0.02 pre-strain

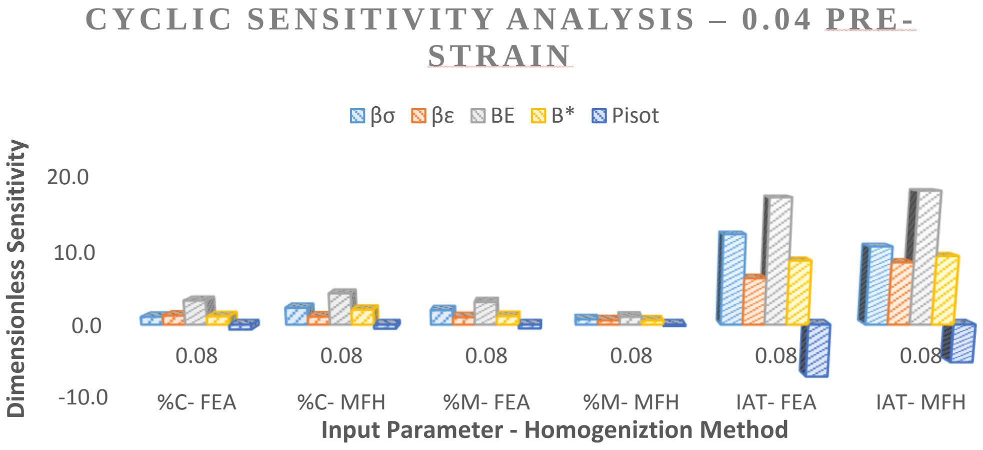

Figure 4.55. Dimensionless sensitivity comparison of FEA and MFH methods on Bauschinger Parameters, 0.03 pre-strain

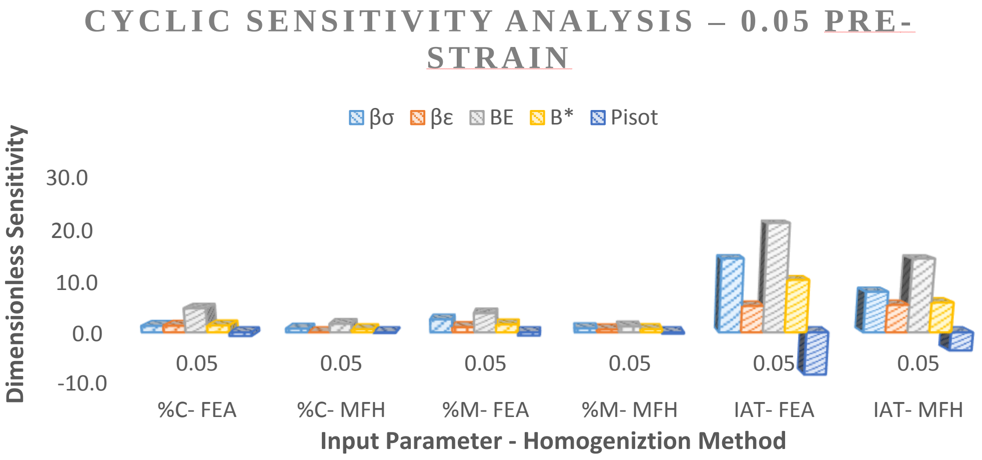

Figure 4.56. Dimensionless sensitivity comparison of FEA and MFH methods on Bauschinger Parameters, 0.05 pre-strain

According to the FEA approximation results, the same pre-strain amount effect of %Carbon, %Martensite and IAT on Bauschinger parameters is sharper than MFH approximation results.

In summary:

- The most effective parameter is the IAT with a very large margin. IAT should be selected carefully during process design. It is observed that IAT is the most sensitive parameter by a large margin in the thermodynamic sensitivity analysis, and the modeling strategy is determined accordingly at the beginning.
- As the pre-strain increases, the effects of carbon content, martensite content and IAT on Bauschinger parameters decrease.
- At low pre-strain (0.02), FEA solutions in the parameter that is related to premature yielding, the amount of martensite is more effective than the amount of carbon, while the amount of carbon is more effective in the parameter that is related to softening. However, as the pre-strain increases,

there is little difference between the effects of these two on Bauschinger parameters. In MFH calculations close values with FEA are obtained from the sensitivity analysis. As a result, it can be said that there is no considerable difference between the effect of %Carbon and %Martensite on Bauschinger parameters. After parametric and sensitivity analyzes are done and their outcomes are collected, same models are used to find Bauschinger effect on BORCELIK and SSAB DP Steel specimens.

4.2.3.3 Cyclic Tension-Compression Curves and Bauschinger Parameters of DP Steel Specimens

After parametric analysis and sensitivity analysis of cyclic curves, the same models are used to extract Bauschinger parameters and to understand the cyclic compression-tension loading behavior of the BOR-DP600, BOR-DP800, SSAB-DP600 and SSAB-DP800 samples. Results are shown in below Figures (Figure 4.57 to Figure 4.60).

4.2.3.3.1 BOR-DP600-Cyclic Curves

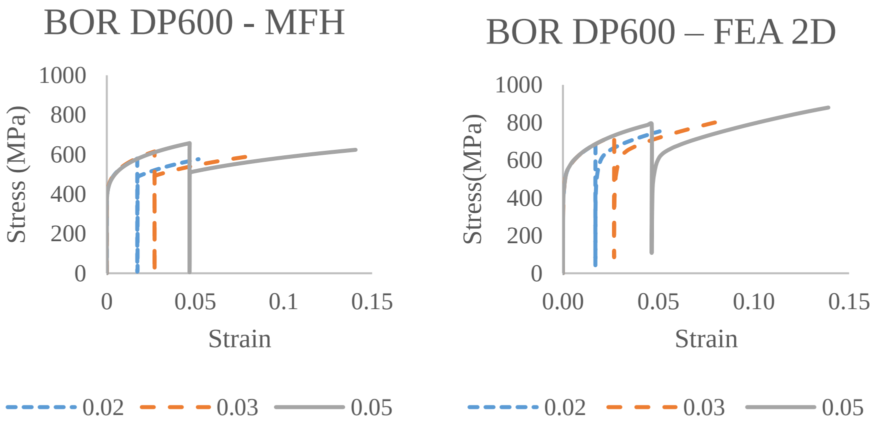

Figure 4.57. Cumulative Plastic Strain vs Absolute Stress Curve of BOR-DP600 a) MFH Results b) 2D-FEA Results

4.2.3.3.2 SSAB-DP600-Cyclic Curves

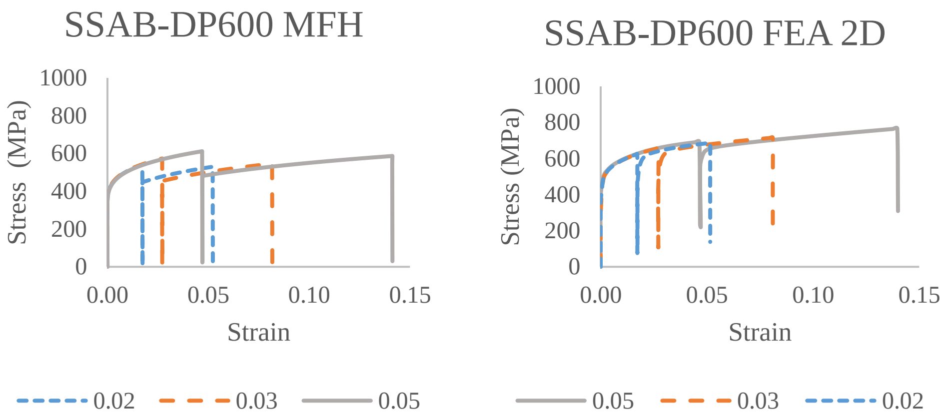

Figure 4.58. Cumulative Plastic Strain vs Absolute Stress Curve of SSAB-DP600 a) MFH Results b) 2D-FEA Results

4.2.3.3.3 BOR-DP800-Cyclic Curves

a) b)

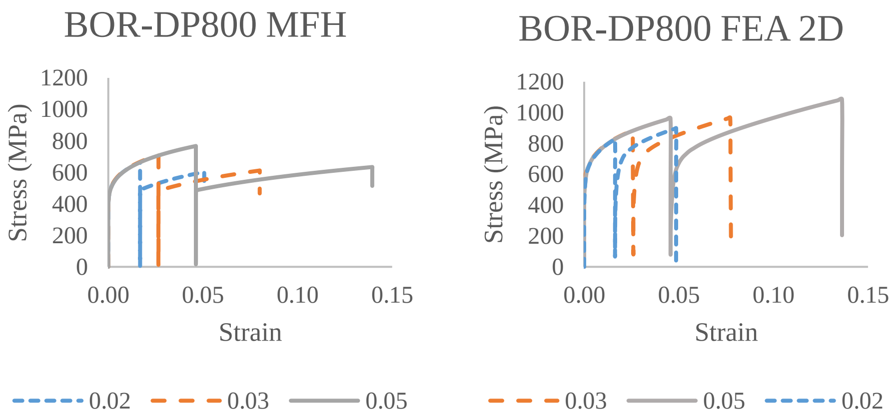

Figure 4.59. Cumulative Plastic Strain vs Absolute Stress Curve of BOR-DP800 a) MFH Results b) 2D-FEA Results

4.2.3.3.4 SSAB-DP800

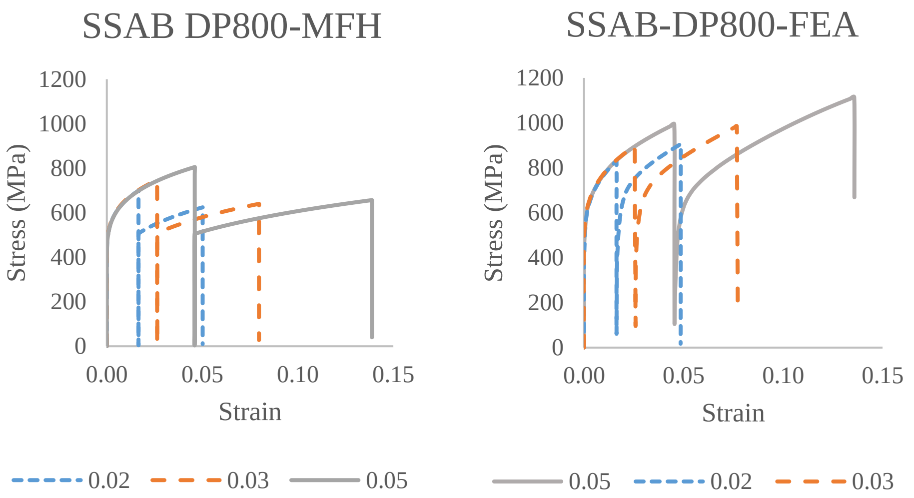

Figure 4.60. Cumulative Plastic Strain vs Absolute Stress Curve of SSAB-DP800 a) MFH Results b) 2D-FEA Results

4.2.3.3.5 Bauschinger Parameters of SSAB-DP600 vs SSAB-DP800 steels

Bauschinger parameter comparison for SSAB-DP600 and SSAB-DP800 with two different homogenization method FEA and MFH can be seen in below Figure 4.61.

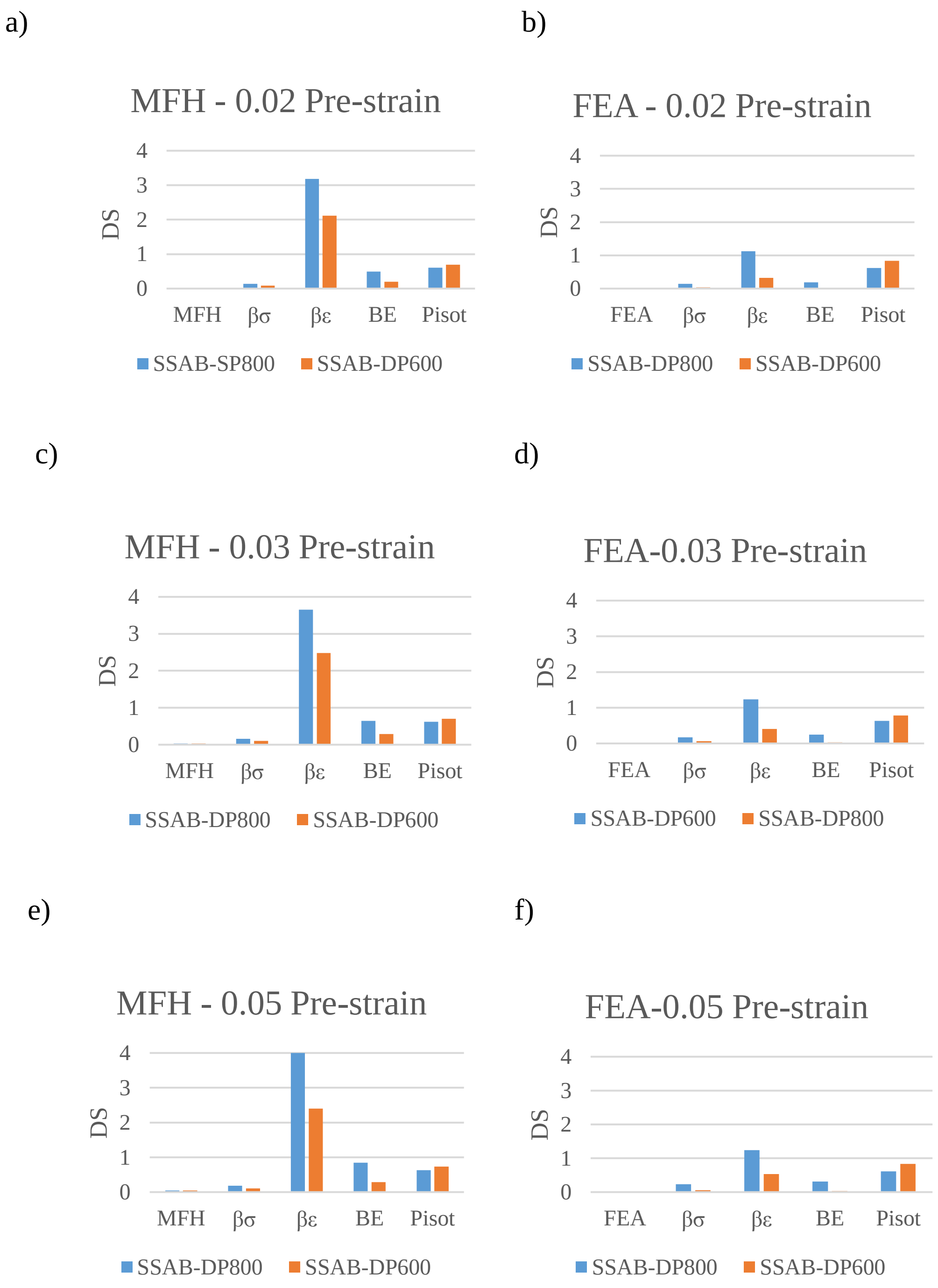

Figure 4.61. Bauschinger parameters of SSAB-DP600 and SSAB-DP800 steels a) MFH Results when Pre-strain is 0.02 b) FEA-2D Results when Pre-strain is 0.02 c) MFH Results when Pre-strain is 0.03 d) FEA-2D Results when Pre-strain is 0.03 e) MFH Results when Pre-strain is 0.05 f) FEA-2D Results when Pre-strain is 0.05

4.2.3.3.6 Bauschinger Parameters of BOR-DP600 vs BOR-DP800 steels

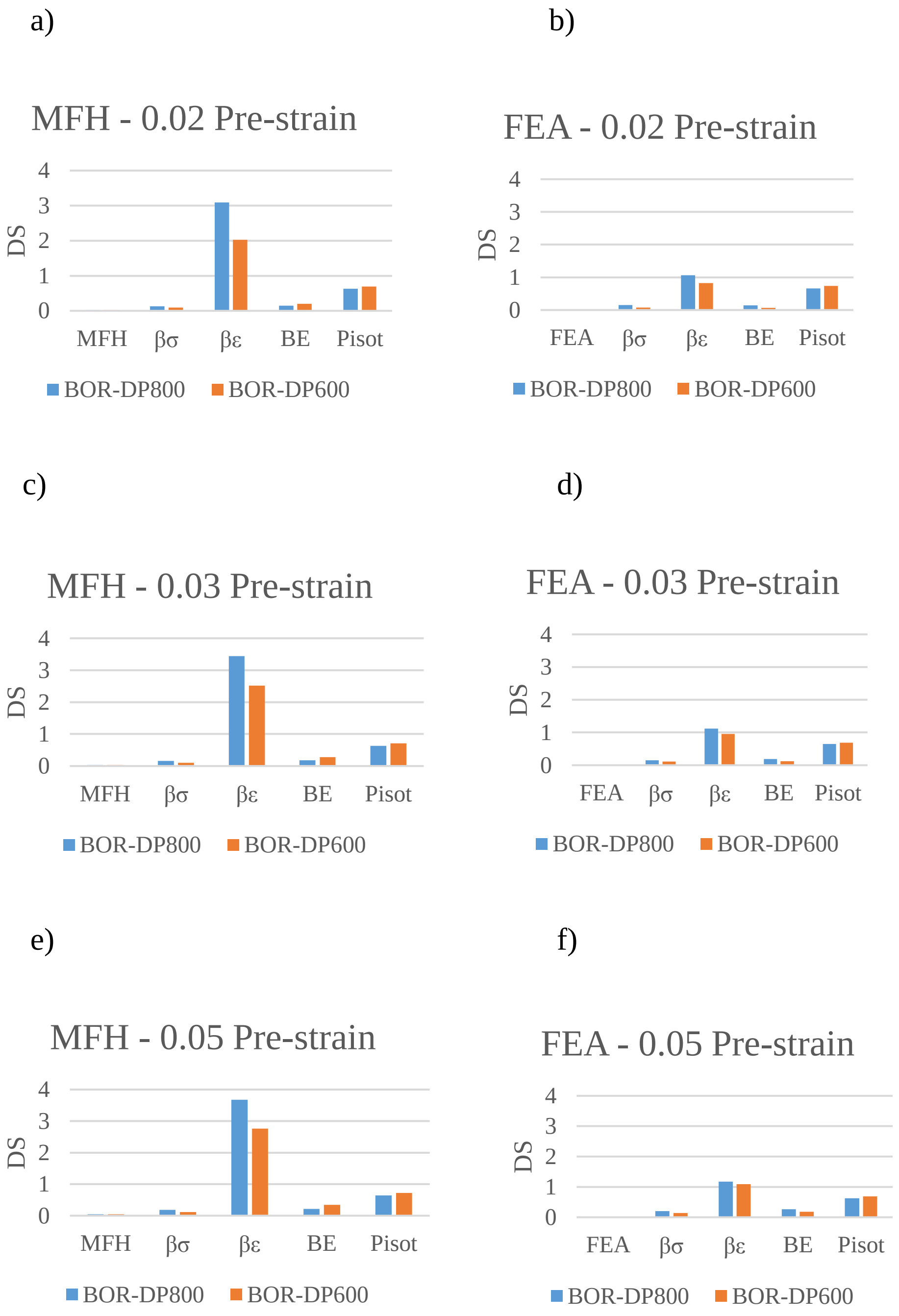

Figure 4.62. Bauschinger parameters of BOR-DP600 and BOR-DP800 steels a) MFH Results when Pre-strain is 0.02 b) FEA-2D Results when Pre-strain is 0.02 c) MFH Results when Pre-strain is 0.03 d) FEA-2D Results when Pre-strain is 0.03 e) MFH Results when Pre-strain is 0.05 f) FEA-2D Results when Pre-strain is 0.05

Bauschinger parameter comparison for BOR-DP600 and BOR-DP800 with two different homogenization method FEA and MFH can be seen in below Figure 4.62.

In summary:

- Back stresses are known to form, especially in multiphase materials, because of the mechanical discrepancies between the embedded particles, the surrounding matrix material, and the mechanical incompatibilities of various phases. Due to the ease of dislocation movement, local back stresses assist to trigger a yield stress reduction in the metal[50]. If the strain direction is then reversed, the same source may then cause dislocations with the opposite sign. Dislocations with opposite sign attract and consume one another, reducing the material's strength. In contrast to what it would have been if the strain had remained in the forward direction, the yield stress of the material is therefore measured to be lower in the opposite direction. This behavior is also observed in the model results for all DP steel samples.
- With increasing martensite volume fraction, the hardening rate increases in the plastic zone and stress amplitude increases.
- It is also mentioned in the previous parts of the thesis that a modeling that does not consider the Bauschinger effect, which is frequently observed especially in multi-phase materials due to the very high long range internal stresses between two mechanically very different constituents formed by misfit strain as compared with the internal stresses in single phase materials, will fail in accurate prediction. In the model results, it is determined that the Bauschinger back stress is strongly effective in all 4 different DP steels with different manufacturing backgrounds and grades. Likewise, it is observed that the effect in DP800 steels increased with the increase of the harder martensite phase volume fraction and the amount of pre-strain, and the effect was higher than that of DP600 steels.
- The fraction of non-recoverable hardening (P_{isot}) decreases as the %Carbon, %Martensite. In other words, reverse yield strength can be predicted more

properly by the isotropic hardening model when the %Carbon or %Martensite is low like DP600 steels, but kinematic hardening becomes more prominent as the %Carbon, %Martensite or IAT increases like in DP800 steels.

CHAPTER 5

CONCLUSION

In this thesis, a novel method known as ICME was used to simulate the process chain modelling of dual-phase (DP) steels (DP600 and DP800) with various chemical compositions and production histories. Multi-scale modeling, a two-way bridge between material production and manufacturing processes, is used to gather the material data needed for this.

Following is a summary of some of the significant findings from the models and experimental comparisons developed for the thesis:

- Data from thermodynamic modeling results are transferred to mechanical models and a framework is created in accordance with ICME principles.
- The models are used to compute and then verify the IA time and temperature needed to obtain the experimental phase fractions for all specimens. An experimental set-up showed that the thermodynamic model works properly and that the experimental and thermodynamic model results are consistent.
- According to thermodynamic sensitivity analysis, IAT is the most critical parameter, and it should be fixed in production processes since it causes high scatter in outputs. %C is highly effective on martensite strength and MS temperature, %Mn and %Si are effective on final ferrite hardness and strength and increase in %Si and %Al promotes formation of new ferrite with smaller grains by decreasing MS and promotes better tensile strength total elongation balance.
- Uniaxial tensile test model sensitivity analysis showed that the yield stress, strain hardening exponent (n) and strain hardening coefficient (K) values of the martensite phase had no effect on the overall yield behavior. This is due to the fact that the martensite phase does not deform at low strain values. As

a result of the results, the mentioned values of martensite were fixed in all DP steel samples in order to simplify the model.

- Both homogenization methods (FEA, MFH) used to extract the general yield behavior measured the yield curves in 3 samples (BOR-DP800, SSAB-DP600, SSAB-DP800) with an error of ~10% and less. The margin of error in the BOR-DP600 sample is more than ~10%. This is because the sample has a smaller grain size compared to the same grade steels, and the models over-predict.
- Both FEA and MFH methods make better predictions in hot rolled SSAB-DP800 and SSAB-DP600 samples compared to cold rolled BOR-DP600 and BOR-DP800 samples. Since the texture effect in hot rolled samples is much more negligible than cold rolled samples, it can be predicted that a model without crystal plasticity will give better results in hot rolled samples. Crystal plasticity calculations can be included in the model to improve the model. In the same way, it can be said that the model needs various improvements to be valid in nano grain size DP steels due to the over prediction that occurs as the grain size decreases.
- When looking at the uniaxial tensile test modeling results, it can be said that the FEA method, which can perform a more detailed analysis and calculates the stress-strain distributions between the phases, is more successful in capturing the general trend of the yield curves, while the MFH results make estimations close to the experimental curve.
- FEA field results showed that the load-bearing phase is martensite and the phase responsible for deformation is ferrite in the composite-like microstructure of DP steels.
- With the results of the sensitivity analysis of the cyclic stress strain model, it is observed that the Bauschinger effect increased as the amount of martensite, which is the harder phase, increased in DP steels. Likewise, as the dissolved carbon ratio in austenite increases Bauschinger effect increases.

- Of the two homogenization methods used (FEA, MFH), FEA is more successful in capturing the trend of cyclic stress strain curves.
- In the models used in this thesis, by using as simple concepts as possible (random inclusion distribution, random orientation, fixed aspect ratio of martensite islands) and reducing the experimental processes, it was examined how well the experimental data could be captured in the process-chain modeling. The results are promising. With detailed microstructural analysis, the model can be developed by defining the sizes, orientations and distributions of martensite islands in modelling phase for DP steels.

REFERENCES

1. Lesar, R. *Introduction to Computational Material Science*. (Cambridge University Press, 2013).
2. Olson, G. Designing a New MaterialWorld. **288**, (2000).
3. Allison, J., Backman, D. & Christodoulou, L. Engineering : A New Paradigm for the Global Materials Profession. 25–27.
4. Faleskog, J., Gao, X. & Shih, C. F. Micromechanics calibration. 355–373 (1998).
5. Darabi, A. C. *et al.* PT US CR. *Mech. Mater.* (2017) doi:10.1016/j.mechmat.2017.04.009.
6. Brisard, S. *et al.* Mori – Tanaka estimates of the effective elastic properties of stress-gradient composites To cite this version : HAL Id : hal-01740741. (2019).
7. Weiss, M., Kupke, A., Manach, P. Y., Galdos, L. & Hodgson, P. D. Author ' s Accepted Manuscript. *Mater. Sci. Eng. A* (2015) doi:10.1016/j.msea.2015.07.037.
8. Gündüz, S. & Tosun, A. Influence of straining and ageing on the room temperature mechanical properties of dual phase steel. **29**, 1914–1918 (2008).
9. Sarwar, M. Materials & Design Influence of epitaxial ferrite on tensile properties of dual phase steel. **28**, 335–340 (2007).
10. Sekkate, Z., Aboutajeddine, A. & Seddouki, A. Elastoplastic mean-field homogenization : recent advances review. *Mech. Adv. Mater. Struct.* **0**, 1–26 (2020).
11. Hill, R. J. & Hill, R. J. Continuum micro-mechanics of elastoplastic

polycrystals To cite this version : HAL Id : hal-03620021. **13**, 89–101 (2022).

12. Sun, S. & Pugh, M. Properties of thermomechanically processed dual-phase steels containing fibrous martensite. **335**, 298–308 (2002).

13. World Auto Steel 2016.

14. Li, Z. & Davis, C. Ironmaking and Steelmaking. 7–10 (2019).

15. Korzewka, A. D., Lawson, R. D., Matlock, D. K. & Krauss, G. A CONSIDERATION OF MODELS DESCRIBING THE STRENGTH AND DUCTILITY OF DUAL-PHASE STEELS. *Scr. Metall.* 1023–1028 (1980).

16. Garcia, C. I. Formation of Austenite in 1 . 5 Pct Mn Steels. **12**, (1981).

17. Azizi-alizamini, H., Militzer, M. & Poole, W. J. Austenite Formation in Plain Low-Carbon Steels. (2010) doi:10.1007/s11661-010-0551-5.

18. Speich, G. R. & Corporation, S. Formation of Austenite During Intercritical Annealing of Dual-Phase Steels. **12**, (1981).

19. Steels, H. B. & Morales-rivas, L. Viewpoints on Technological Aspects of Advanced High-Strength Bainitic Steels. (2022).

20. Darabi, A. C., Chamani, H. R., Kadkhodapour, J. & Anaraki, A. P. Micromechanical analysis of two heat-treated dual phase steels: DP800 and DP980. *Mech. Mater.* (2016) doi:10.1016/j.mechmat.2017.04.009.

21. Raabe, B. D., Klose, P., Engl, B., Imlau, K. & Friedel, F. Concepts for Integrating Plastic Anisotropy into Metal Forming Simulations. 169–180 (2002).

22. Tasan, C. C. *et al.* An Overview of Dual-Phase Steels : Advances in Processing and Micromechanically Guided Design. 1–41 (2015) doi:10.1146/annurev-matsci-070214-021103.

23. 22-hölscher.pdf.

24. Radkahanta, R. & Singh, S. B. *Automotive Steels Design, Metallurgy, Processing and Applications*. (2017).

25. Hidenori, B. Effect of Cold of Hot Rolled Band Dual Microstructure Phase Steel * on Strength and Ductility. 360–365 (1987).

26. Garcia, C. I., Cho, K., Redkin, K., Deardo, A. J. & Tan, S. Influence of Critical Carbide Dissolution Temperature during Intercritical Annealing on Hardenability of Austenite and Mechanical Properties of DP-980 Steels. **51**, 969–974 (2011).

27. High, A. & Steel, S. metals The E ff ect of Rapid Heating and Fast Cooling on the Transformation Behavior and Mechanical Properties. 1–12 (2019).

28. Davies, R. G. & Company, F. M. Influence of Martensite Composition and Content on the Properties of Dual Phase Steels. **9**, 671–679 (1978).

29. BANGARU, N.-R. V. & SACHDEV, A. K. Influence of Cooling Rate on the Microstructure and Retained Austenite in an Intercritically Annealed Vanadium Containing HSLA Steel. *Metall. Trans.* 1899–1906 (1982).

30. MARK D. GEIB & KRAUSS, D. K. M. G. The Effect of Intercritical Annealing Temperature on the Structure of Niobium Microalloyed Dual Phase Steel. *Metall. Trans.* 1683–1689 (1980).

31. Fonstein, N., Kapustin, M., Pottore, N., Gupta, I. & Yakubovsky, O. Factors that Determine the Level of the Yield Strength and the Return of the Yield-Point Elongation in Low-Alloy Ferrite – Martensite Steels. **104**, 328–336 (2007).

32. Shen, X. P. & Priestner, R. Effect of Boron on the Microstructure and Tensile Properties of Dual-Phase Steel. (1989).

33. Concepción, V. L., Lorusso, H. N. & Svoboda, H. G. Effect of carbon content on microstructure and mechanical properties of dual phase steels. *Procedia Mater. Sci.* (2013).

34. Ali, M. *et al.* Influence of chromium content on the microstructure and mechanical properties of thermomechanically hot-rolled low-carbon bainitic steels containing niobium. *Appl. Sci.* **10**, (2020).

35. Rashid, M. . No Title. *A Unique High Strength Sheet Steel with Super.* (1977).

36. Fereiduni, E. & Banadkouki, S. S. G. Reliability / unreliability of mixture rule in a low alloy ferrite – martensite dual phase steel. *J. Alloys Compd.* **577**, 351–359 (2013).

37. Dulucheanu, C., Severin, T. L., Cerlinca, D. A. & Irimescu, L. Structures and Mechanical Properties of Some Dual-Phase Steels with Low Manganese Content. (2022).

38. Luo, Y. Isotropized Voigt-Reuss model for prediction of elastic properties of particulate composites. *Mech. Adv. Mater. Struct.* **0**, 1–13 (2021).

39. Tomita, Y. & Okabayashi, K. Tensile Stress-Strain Analysis of Cold Worked Metals and Steels and Dual-Phase Steels. 865–872 (1985).

40. Granbom, Y. *Structure and mechanical properties of dual phase steels – An experimental and theoretical analysis*.

41. Ennis, B. A review of the effects of chemical and phase segregation on the mechanical behaviour of multi-phase steels.

42. Maalekian, M. Technische Universität Graz Christian Doppler Laboratory for Early Stages of Precipitation The Effects of Alloying Elements on Steels (I). (2007).

43. De, V. L., Lorusso, H. N. & Svoboda, H. G. Effect of carbon content on microstructure and mechanical properties of dual phase steels. *Procedia Mater. Sci.* **8**, 1047–1056 (2015).

44. Nouri, A. & Saghafian, H. Effects of Silicon Content and Intercritical

Annealing on Manganese Partitioning in Dual Phase Steels. *J. Iron Steel Res. Int.* **17**, 44–50 (2010).

45. Zhou, L., Zhang, D. & Liu, Y. Influence of silicon on the microstructures , mechanical properties and stretch-flangeability of dual phase steels. (2014) doi:10.1007/s12613-014-0968-8.

46. Fr, D. David Frómeta Gutiérrez Doctoral thesis.

47. ASM International. *ASM Handbook, Heat Treating*. vol. 4 (1991).

48. Coldren, A. P., Eldis, G. T. & Arbor, A. to Optimize the Composition of an As-Rolled. 41–48.

49. Nanda, T., Singh, V. & Singh, V. Third generation of advanced high-strength steels : Processing routes and properties. **0**, 1–30 (2016).

50. Zhonghua, L. I. & Haicheng, G. U. Bauschinger Effect and Residual Phase Stresses in Two Ductile-Phase Steels: Part I. The Influence of Phase Stresses on the Bauschinger Effect. **21**, 717–724 (1990).

51. Zhonghua, L. I. & Haicheng, G. U. Bauschinger Effect and Residual Phase Stresses in Two Ductile-Phase Steels : Part I1 . The Effect of Microstructure and Mechanical Properties of the Constituent Phases on Bauschinger Effect and Residual Phase Stresses (): r / Op. **21**, 725–732 (1990).

52. Sowerby, R., Uko, D. K. & Tomita, Y. R ; **41**, 43–58 (1979).

53. Sowerby, R. & Uko, D. K. A Review of Certain Aspects of the Bauschinger Effect in Metals. 43–58 (1979).

54. Aran, A., Demirkol, M. & Karabulut, A. Bauschinger effect in precipitation strengthened aluminium alloy 2024. 35–39 (1987).

55. Şimşir, C. *et al.* The Bauschinger effect in the supercooled austenite of SAE 52100 steel. *Acta Mater.* 4478–4491 (2010).

56. Lemoine, X. & Aouafi, A. B auschinger effect correspondence of

experimental tests. 241–244 (2008) doi:10.1007/s12289-008-0357-9.

57. Mollica, F., Rajagopal, K. R. & SrinivasaA.R. The Inelastic Behavior of Material Subject to Loading Reversal. *Int. J. Plast.* 1119–1146 (2001) doi:10.1016/S0749-6419(00)00082-6.

58. Choteau, M., Quaegebeur, P. & Degallaix, S. Modelling of Bauschinger effect by various constitutive relations derived from thermodynamical formulation. **37**, 1143–1152 (2005).

59. Xiang, Y. & Vlassak, J. J. Bauschinger effect in thin metal films. **53**, 177–182 (2005).

60. Solanki, K. N., Horstemeyer, M. F., Steele, W. G., Hammi, Y. & Jordon, J. B. International Journal of Solids and Structures Calibration , validation , and verification including uncertainty of a physically motivated internal state variable plasticity and damage model. *Int. J. Solids Struct.* **47**, 186–203 (2010).

61. Thermocalc Software. CALPHAD Methodology.

62. 8. National Research Council, C. Integrated Computational Materials Engineering: A Transformational Discipline for Improved Competitiveness and National Security. (2008).

63. Eds, J. H. W. & Truyol, J. P. C. A. *Thermodynamic Modeling and Materials Data Engineering*.

64. Huh, J., Huh, H. & Soo, C. Effect of strain rate on plastic anisotropy of advanced high strength steel sheets. *Int. J. Plast.* **44**, 23–46 (2013).

65. Trofimov, A., Drach, B. & Sevostianov, I. Effective elastic properties of composites with particles of polyhedral shapes. *Int. J. Solids Struct.* (2017) doi:10.1016/j.ijsolstr.2017.04.037.

66. Hashin, Z. & Shtrikman, S. A variational approach to the elastic behavior of

multiphase minerals. Journal of the Mechanics and Physics of Solids. 127–140 (1963) doi:DOI:10.1016/0022-5096(63)90060-7.

67. Bendsùe, M. P. & Sigmund, O. Material interpolation schemes in topology optimization. **69**, (1999).

68. Hill, R. J. Continuum micro-mechanics of elastoplastic polycrystals. *J. Mech. Phys. Solids* **13**, 89–101 (1965).

69. Kröner, E. ZUR PLASTISCHEN VERFORMUNG DES VIELKRISTALLS*. *Acta Met.* 89–101 (1965).

70. Iwakuma, T. Finite Elastic-Plastic Deformation of Polycrystalline Metals. 87–119 (1984) doi:10.1098/rspa.1984.0071.

71. Çavuşoğlu, O., Toros, S. & Gürün, H. Microstructure based modelling of stress – strain relationship on dual phase steels. **9233**, 0–7 (2017).

72. Liu, Z.-K. & Wang, Y. *Computational Thermodynamics of Materials*. (2016).

73. Aydogan, E. *et al.* Materials Science & Engineering A Effect of shock loading on the microstructure , mechanical properties and grain boundary characteristics of HT-9 ferritic / martensitic steels. *Mater. Sci. Eng. A* **651**, 75–82 (2016).

APPENDICES

A. FEA Field Results of 90° Uniaxial Tensile Test Model

A.1) SSAB-DP600-90 Field Results (Equivalent Von-Mises distribution, Equivalent Plastic Strain distribution)

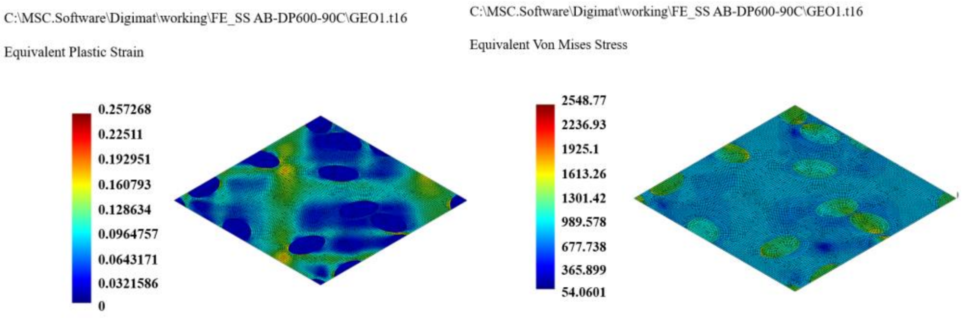

A.2) SSAB-DP800-90 Field Results (Equivalent Von-Mises distribution, Equivalent Plastic Strain distribution)

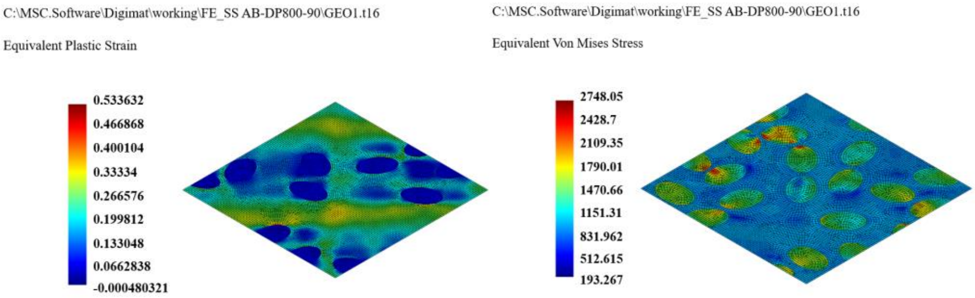

A.3) BOR-DP600-90 Field Results (Equivalent Von-Mises distribution, Equivalent Plastic Strain distribution)

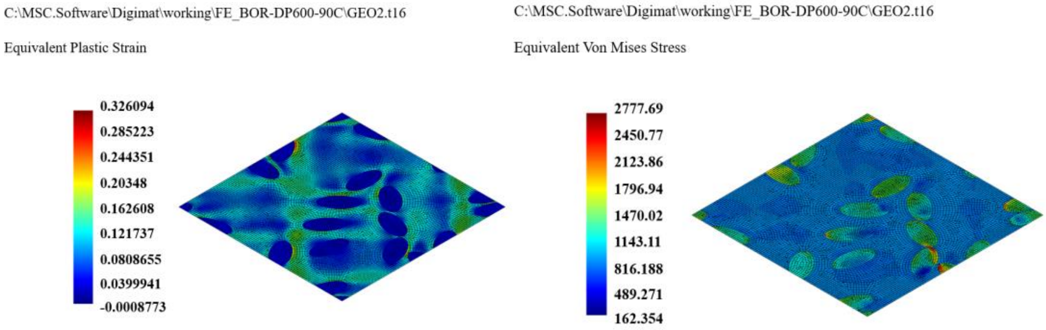

A.4) BOR-DP800-90 Field Results (Equivalent Von-Mises distribution, Equivalent Plastic Strain distribution)

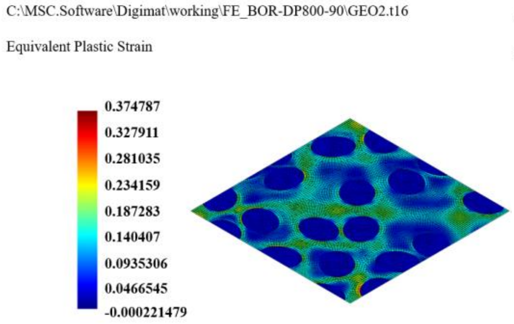

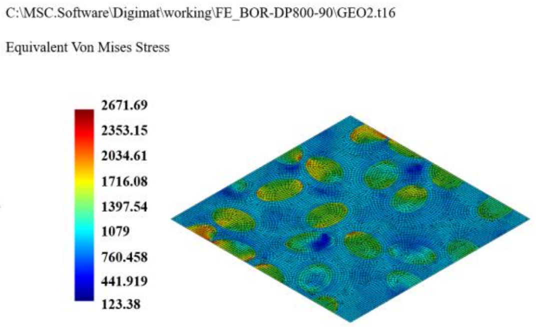

B. Bauschinger Effect Calculation Parameters for Sensitivity Analysis Inputs %Carbon, %Martensite, IAT (°C) and for DP Steel Specimens with two different homogenization method FEA and MFH

B.1) FEA Cyclic Stress-Strain Model Bauschinger Effect Calculation Parameters on a Fictitious Steel – 0.05%C

0.05 %C	**FEA**		
Pre-Strain	**0.02**	**0.04**	**0.05**
σ+	628.59	678.14	691.14
σ-	618	648	660
σ0	526	526	526
βσ	0.01	0.02	0.02
ε0	0.02	0.04	0.05
εB	0.003	0.01	0.013
Bε	0.16	0.27	0.28
EB	0.06	0.21	0.27
E0	9.93	22.87	29.71
BE	0.01	0.01	0.01
B*	0.10	0.20	0.19
Pisot	0.91	0.83	0.84
E (MPa)	229000	229000	229000

B.2) FEA Cyclic Stress-Strain Model Bauschinger Effect Calculation Parameters on a Fictitious Steel – 0.1%C

0.1 %C	FEA		
Pre_Strain	0.02	0.04	0.05
σ+	668.31	729.68	749.43
σ-	585	572	583
σ0	542	542	542
βσ	0.08	0.15	0.15
ε0	0.02	0.04	0.05

Table B.2 (Cont'd)

εB	0.01	0.03	0.04
βε	0.65	0.73	0.75
EB	0.51	1.56	2.18
E0	10.17	24.24	42.04
BE	0.05	0.06	0.05
B*	0.66	0.84	0.80
Pisot	0.60	0.54	0.56
E(Gpa)	224	224	224

B.3) FEA Cyclic Stress-Strain Model Bauschinger Effect Calculation Parameters on a Fictitious Steel – 0.15%C

0.15 %C	**FEA**		
Pre-Strain	**0.02**	**0.04**	**0.05**
σ+	723.66	823.52	861.5
σ-	555	500	480
σ0	568	568	568
βσ	0.12	0.20	0.22
ε0	0.017	0.04	0.05
εB	0.02	0.05	0.06
βε	1.18	1.31	1.26
EB	1.66	6.33	8.69
E0	10.76	25.56	33.93
BE	0.15	0.25	0.26
B*	1.08	1.27	1.30
Pisot	0.48	0.44	0.43
E (Gpa)	220	220	220

B.4) MFH Cyclic Stress-Strain Model Bauschinger Effect Calculation Parameters on a Fictitious Steel – 0.05%C

0.05 %C	**MFH**		
Pre_Strain	**0.02**	**0.04**	**0.05**
σ+	543.08	591.31	609.34
σ-	490.5	511.2	515.4
σ0	444	444	444
βσ	0.05	0.07	0.08
ε0	0.02	0.04	0.05
εB	0.02	0.07	0.098
βε	1.29	1.76	2.09
EB	0.58	2.60	4.60
E0	8.40	9.58	25.70
BE	0.07	0.27	0.18
B*	0.27	0.27	0.28
Pisot	0.79	0.79	0.78
E (Gpa)	210	210	210

B.5) MFH Cyclic Stress-Strain Model Bauschinger Effect Calculation Parameters on a Fictitious Steel – 0.1%C

0.1 %C	**MFH**		
Pre-Strain	**0.02**	**0.04**	**0.05**
σ+	552.5	607.42	628.04
σ-	463	502	513
σ0	448	448	448
βσ	0.08	0.09	0.09
ε0	0.02	0.04	0.05
εB	0.04	0.08	0.10
βε	2.41	2.19	2.04
EB	1.83	4.27	5.52

Table B.5(Cont’d)

E0	8.45	20.02	26.21
BE	0.22	0.21	0.21
B*	0.43	0.33	0.32
Pisot	0.70	0.75	0.76
E (Gpa)	210	210	210

B.6) MFH Cyclic Stress-Strain Model Bauschinger Effect Calculation Parameters on a Fictitious Steel – 0.15%C

0.15 %C	MFH		
Pre-Strain	**0.02**	**0.04**	**0.05**
σ+	567.95	630.56	654.1
σ-	436	443	457
σ0	450	450	450
βσ	0.12	0.15	0.15
ε0	0.02	0.04	0.05
εB	0.05	0.12	0.14
βε	2.96	3.24	3.07
EB	3.32	11.24	14.21
E0	8.59	20.57	26.94
BE	0.39	0.55	0.53
B*	0.56	0.52	0.48
Pisot	0.64	0.66	0.67
E(Gpa)	210	210	210

B.7) FEA Cyclic Stress-Strain Model Bauschinger Effect Calculation Parameters on a Fictitious Steel – 15%Martensite

15%Mar	**FEA**		
Pre-Strain	**0.02**	**0.04**	**0.05**
σ+	623	673	688
σ-	592	618	632

Table B.7 (Cont'd)

σ0	518	518	518
βσ	0.025	0.04	0.04
ε0	0.02	0.04	0.05
εB	0.007	0.02	0.02
βε	0.41	0.43	0.45
EB	0.26	0.47	0.66
E0	9.66	22.69	30.88
BE	0.03	0.02	0.02
B*	0.30	0.36	0.33
Pisot	0.77	0.74	0.75
E(Gpa)	224	224	224

B.8) FEA Cyclic Stress-Strain Model Bauschinger Effect Calculation Parameters on a Fictitious Steel – 30%Martensite

30%Mar	**FEA**		
Pre-Strain	**0.02**	**0.04**	**0.05**
σ+	676	746	771
σ-	592	600	585
σ0	528	528	528
βσ	0.06	0.10	0.12
ε0	0.02	0.04	0.05
εB	0.01	0.04	0.05
βε	0.77	0.95	1.00
EB	0.59	2.46	3.87
E0	10.26	24.54	32.09
BE	0.06	0.10	0.12
B*	0.57	0.67	0.77
Pisot	0.64	0.60	0.57
E (GPa)	224	224	224

B.9) FEA Cyclic Stress-Strain Model Bauschinger Effect Calculation Parameters on a Fictitious Steel – 45%Martensite

45%M	**FEA**		
Pre-Strain	**0.02**	**0.04**	**0.05**
σ+	902	1100	1174
σ-	500	390	348
σ0	638	638	638
βσ	0.22	0.32	0.35
ε0	0.02	0.04	0.05
εB	0.02	0.05	0.07
βε	1.44	1.49	1.49
EB	4.30	14.43	20.46
E0	13.76	31.16	42.76
BE	0.31	0.46	0.48
B*	1.52	1.54	1.54
Pisot	0.40	0.39	0.39
E (Gpa)	225	225	225

B.10) MFH Cyclic Stress-Strain Model Bauschinger Effect Calculation Parameters on a Fictitious Steel – 15%Martensite

15%M	MFH		
Pre-Strain	**0.02**	**0.04**	**0.05**
σ+	537.3	585.24	602.47
σ-	481	510	523
σ0	435	435	435
βσ	0.05	0.06	0.07
ε0	0.02	0.04	0.05
εB	0.03	0.06	0.09
βε	1.71	1.51	1.87
EB	0.82	2.11	3.50
E0	8.29	19.49	25.41
BE	0.10	0.11	0.14
B*	0.28	0.25	0.24

Table B.10 (Cont'd)

Piso	0.78	0.80	0.81
E(Gpa)	210	210	210

B.11) MFH Cyclic Stress-Strain Model Bauschinger Effect Calculation Parameters on a Fictitious Steel – 30%Martensite

30%M	**MFH**		
Pre-Strain	**0.02**	**0.04**	**0.05**
σ+	676.01	745.5	771.16
σ-	592	600	585
σ0	528	528	528
βσ	0.06	0.10	0.12
ε0	0.02	0.04	0.05
εB	0.01	0.04	0.05
βε	0.77	0.95	1.00
EB	0.59	2.46	3.87
E0	10.26	24.54	32.09
BE	0.06	0.10	0.12
B*	0.57	0.67	0.77
Pisot	0.64	0.60	0.57
E (GPa)	224	224	224

B.12) MFH Cyclic Stress-Strain Model Bauschinger Effect Calculation Parameters on a Fictitious Steel – 45%Martensite

45%M	**MFH**		
Pre-Strain	**0.02**	**0.04**	**0.05**
σ+	901.68	1100.1	1173.7
σ-	500	390	348
σ0	638	638	638
βσ	0.22	0.32	0.35

Table B.12 (Cont'd)

ε0	0.02	0.04	0.05
εB	0.02	0.05	0.07
βε	1.44	1.49	1.49
EB	4.30	14.43	20.46
E0	13.76	31.16	42.76
BE	0.31	0.46	0.48
B*	1.52	1.54	1.54
Pisot	0.40	0.39	0.39
E (Gpa)	225	225	225

B.13) FEA Cyclic Stress-Strain Model Bauschinger Effect Calculation Parameters on a Fictitious Steel – 715 °C

715 °C	**FEA**		
Pre-Strain	**0.02**	**0.04**	**0.05**
σ+	646.48	700.21	715.98
σ-	620	637	648
σ0	447.3	447.3	447.3
βσ	0.02	0.05	0.05
ε0	0.02	0.04	0.05
εB	0.01	0.02	0.04
βε	0.34	0.57	0.83
EB	0.15	0.61	1.54
E0	9.96	23.52	30.62
BE	0.01	0.03	0.05
B*	0.13	0.25	0.25
Pisot	0.88	0.80	0.80
Elastic Modulus	2.29E+05	229000	229000

B.14) FEA Cyclic Stress-Strain Model Bauschinger Effect Calculation Parameters on a Fictitious Steel – 750 °C

750 °C	**FEA**		
Pre_Strain	**0.02**	**0.04**	**0.05**
σ+	672.77	747.46	774.51
σ-	568	575	553
σ0	548	548	548
βσ	0.08	0.12	0.14
ε0	0.02	0.04	0.05
εB	0.01	0.04	0.05
βε	0.82	1.05	1.04
EB	0.68	3.13	4.23
E0	10.18	24.49	32.16
BE	0.07	0.13	0.13
B*	0.77	0.86	0.89
Pisot	0.57	0.54	0.53
Elastic Modulus	2.21E+05	221000	221000

B.15) FEA Cyclic Stress-Strain Model Bauschinger Effect Calculation Parameters on a Fictitious Steel – 775 °C

775 °C	**FEA**		
Pre-Strain	**0.02**	**0.04**	**0.05**
σ+	704.28	805.73	845.65
σ-	539	492	465
σ0	536	536	536
βσ	0.12	0.19	0.23
ε0	0.02	0.04	0.05
εB	0.02	0.05	0.06
βε	1.24	1.28	1.30
EB	1.28	6.34	9.32
E0	10.45	24.89	33.24
BE	0.12	0.25	0.28
B*	0.98	1.16	1.23
Pisot	0.50	0.46	0.45
Elastic Modulus (MPa)	217000	217000	217000

B.16) MFH Cyclic Stress-Strain Model Bauschinger Effect Calculation Parameters on a Fictitious Steel – 715 °C

715 °C	**MFH**		
Pre_Strain	**0.02**	**0.04**	**0.05**
σ+	566.7	619.44	638.3
σ-	502	546	533
σ0	461	461	461
βσ	0.06	0.06	0.08
ε0	0.02	0.04	0.05
εB	0.03	0.06	0.09
βε	1.63	1.54	1.98
EB	0.90	2.09	4.90
E0	8.74	20.59	26.88
BE	0.10	0.10	0.18
B*	0.61	0.46	0.59
Pisot	0.62	0.68	0.63
E (Gpa)	210	210	210

B.17) MFH Cyclic Stress-Strain Model Bauschinger Effect Calculation Parameters on a Fictitious Steel – 750 °C

750 °C	**MFH**		
Pre-Strain	**0.02**	**0.04**	**0.05**
σ+	562.88	595.09	642.54
σ-	453	448	491
σ0	438	438	438
βσ	0.1	0.12	0.12
ε0	0.02	0.04	0.05
εB	0.05	0.11	0.16
βε	2.94	2.97	3.40
EB	2.75	8.09	12.12
E0	8.57	20.40	26.72
BE	0.32	0.40	0.45
B*	0.88	0.94	0.74

Table B.17 (Cont'd)

Pisot	0.53	0.52	0.57
E (Gpa)	210	210	210

B.18) MFH Cyclic Stress-Strain Model Bauschinger Effect Calculation Parameters on a Fictitious Steel – 775 °C

775 °C	**MFH**		
Pre-Strain	**0.02**	**0.03**	**0.05**
σ+	577	643	668
σ-	430	432	448
σ0	453	453	453
βσ	0.13	0.16	0.16
ε0	0.02	0.04	0.05
εB	0.05	0.13	0.16
βε	3.14	3.53	3.48
EB	3.93	13.8	17.98
E0	8.69	20.9	27.49
BE	0.45	0.66	0.65
B*	1.18	1.11	1.02
Pisot	0.46	0.47	0.49
E (Gpa)	210	210	210

B.19) MFH Cyclic Stress-Strain Model Bauschinger Effect Calculation Parameters for BOR-DP600 Steel

MFH			
	0.02	**0.03**	**0.05**
σ+	579.38	615.2	657.26
σ-	475	493.6	510.8
σ0	465	465	465
βσ	0.09	0.1	0.11
ε0	0.02	0.03	0.05
εB	0.04	0.068	0.13

Table B.19 (Cont’d)

βε	2.02	2.52	2.77
EB	1.82	4.13	9.52
E0	9.01	14.93	27.38
BE	0.20	0.28	0.35
B*	0.46	0.40	0.38
Pisot	0.69	0.71	0.72
Elastic Modulus	210000	208266	210000

B.20) FEA Cyclic Stress-Strain Model Bauschinger Effect Calculation Parameters for BOR-DP600 Steel

FEA			
Pre Strain	**0.02**	**0.03**	**0.05**
σ+	685.11	730.98	792.85
σ-	582	565	568
σ0	542	542	542
βσ	0.08	0.11	0.14
ε0	0.02	0.027	0.05
εB	0.01	0.026	0.05
βε	0.82	0.96	1.09
EB	0.71	2.16	5.73
E0	10.41	17.33	32.45
BE	0.07	0.12	0.18
B*	0.36	0.44	0.45
Pisot	0.74	0.69	0.69
Elastic Modulus	227919	228450	227500

B.21) MFH Cyclic Stress-Strain Model Bauschinger Effect Calculation Parameters for SSAB-DP600 Steel

MFH			
Pre Strain	**0.02**	**0.03**	**0.05**
σ+	540.28	573.3	611.67
σ-	448	454	482
σ0	436	436	436
βσ	0.09	0.10	0.11
ε0	0.02	0.03	0.05
εB	0.04	0.07	0.11
βε	2.12	2.48	2.40
EB	1.66	3.99	7.33
E0	8.28	13.90	25.60
BE	0.20	0.29	0.29
B*	0.44	0.43	0.37
Pisot	0.69	0.70	0.73
Elastic Modulus	201694.8	202636.4	202279.1

B.22) FEA Cyclic Stress-Strain Model Bauschinger Effect Calculation Parameters for SSAB-DP600 Steel

FEA			
Pre Strain	**0.02**	**0.03**	**0.05**
σ+	625	657	693
σ-	582	576	620
σ0	515	515	515
βσ	0.03	0.06	0.06
ε0	0.02	0.03	0.05
εB	0.01	0.01	0.03
βε	0.32	0.41	0.53
EB	0.12	0.45	0.91
E0	9.80	16.03	28.99
BE	0.012	0.027	0.032
B*	0.20	0.29	0.21

Table B.22 (Cont'd)

Pisot	0.84	0.78	0.83
Elastic Modulus	223731	228600	194980

B.23) MFH Cyclic Stress-Strain Model Bauschinger Effect Calculation Parameters for BOR-DP800 Steel

MFH			
Pre Strain	**0.02**	**0.03**	**0.05**
σ+	664.44	710.51	767.61
σ-	489	484	487
σ0	518	518	518
βσ	0.13	0.16	0.18
ε0	0.02	0.03	0.05
εB	0.05	0.09	0.17
βε	3.10	3.44	3.68
EB	1.47	3.06	6.59
E0	9.91	16.72	31.067
BE	0.149	0.183	0.212
B*	0.6	0.59	0.56
Pisot	0.63	0.63	0.64
Elastic Modulus	207473	207473	207473

B.24) FEA Cyclic Stress-Strain Model Bauschinger Effect Calculation Parameters for BOR-DP800 Steel

FEA			
Pre Strain	**0.02**	**0.03**	**0.05**
σ+	827	883	963
σ-	637	618	587
σ0	642	642	642
βσ	0.15	0.15	0.2
ε0	0.016	0.026	0.046
εB	0.017	0.029	0.054

Table B.24(Cont’d)

βε	1.06	1.12	1.17
EB	1.615	3.843	10.152
E0	11.925	20.038	38.413
BE	0.14	0.19	0.26
B*	0.51	0.55	0.59
Pisot	0.66	0.65	0.63
Elastic Modulus	199717	218935	224988

B.25) MFH Cyclic Stress-Strain Model Bauschinger Effect Calculation Parameters for SSAB-DP800 Steel

MFH			
Pre Strain	**0.02**	**0.03**	**0.05**
σ+	699.4	746.7	805.5
σ-	510	509	506
σ0	552	552	552
βσ	0.135	0.159	0.186
ε0	0.017	0.026	0.046
εB	0.054	0.095	0.184
βε	3.18	3.65	4.00
EB	5.114	11.291	27.554
E0	10.425	17.511	32.726
BE	0.491	0.645	0.842
B*	0.64	0.61	0.59
Pisot	0.61	0.62	0.63
Elastic Modulus	207394	207394	207394

B.26) FEA Cyclic Stress-Strain Model Bauschinger Effect Calculation Parameters for BOR-DP800 Steel

FEA			
Pre Strain	**0.02**	**0.03**	**0.05**
σ+	830	896	994
σ-	592	586	538
σ0	632	632	632
βσ	0.14	0.17	0.23
ε0	0.016	0.026	0.046
εB	0.018	0.032	0.057
βε	1.13	1.23	1.24
EB	2.142	4.96	12.99
E0	11.55	20.38	41.67
BE	0.185	0.243	0.31
B*	0.60	0.59	0.63
Pisot	0.62	0.63	0.61
Elastic Modulus	22501	195088	213060